1998

Flow characteristics in the inlet region of a power plant stack by Francisco Dovali-Solis.

Francisco Dovali-Solis
Lehigh University

Dovali-Solis, Francisco

Flow Characteristics in the Inlet Region of a Power Plant Stack

January 10, 1999

Flow Characteristics in the Inlet Region of a Power Plant Stack

by

Francisco Dovali-Solis

A Thesis

Presented to the Graduate Committee

of Lehigh University

in Candidacy for the Degree of

Master of Science

in

Mechanical Engineering

Lehigh University

November 12, 1998

This thesis is accepted and approved in partial fulfillment of the requirements for the Master of Science.

NOV. 23, 1998

Date

Dr. Edward K. Levy, Professor
Thesis Advisor

Dr. Charles R. Smith, Professor
Chairperson of Department

Table of Contents

List of Tables.

List of Figures.

Nomenclature

x	x-direction
y	y-direction
$\dot{m}$	Mass flow
ρ	Density
A	Total Cross-Sectional Area
N	Number of Measurement Points
ΔA	Total Area divided by N
V_T	Total Velocity
V_Z	Axial Velocity
V_r	Radial Velocity
V_θ	Tangential Velocity
RA	Resultant Angle
α	Yaw
β	Pitch
L	Stack Length
D	Stack Diameter
μ	Viscosity
P	Perimeter
C	Pitot Probe Pressure Coefficient
P_T	Total pressure
P_{DYN}	Dynamic Pressure
P_S	Static Pressure
T_{AIR}	Air temperature
P_{ATM}	Atmospheric Pressure
ϕ_{AIR}	Relative Humidity
ΔP	Stack Pressure Drop
U	Uncertainty
Δ	Random Error

B	Bias Error
S	Precision Index
t	t-Student Variable
w_{xi}	Relative Precision
VPC	Velocity Pressure Coefficient
SA	Station A, 1.1 diameters from Inlet
SB	Station B, 2.44 diameters from Inlet
SC	Station C, 3.88 diameters from Inlet
X	X-vortex cell
Y	Y-vortex cell
S	Swirl Number
R	Circular cross-section Radius
k	Turbulent Kinetic Energy
ε	Turbulence Dissipation Rate
	S-probe error from Figure 6.3
ε	Flow Rate Error

To produce a mighty book, you must choose a mighty theme. No great and enduring volume can ever be written on the flea, though many there be who have tried it.

Herman Melville
(1819-1891)
Moby Dick

Abstract

Flow characteristics occurring in a power plant stack with a radial inlet geometry were investigated using a $1/10^{th}$ scale laboratory model, with dimensions of 0.4572 m (18 in) in diameter and 12.1 m (476.4 in) in length. Experimental results of axial velocity, secondary flow, and swirl are presented for planes located at 1.01, 2.44, and 3.88 diameters from the downstream corner of the inlet breaching. The average axial velocity in the stack was approximately 37 m/s (121.4 ft/s). Three-dimensional velocity measurements were collected in the inlet region using a type DA three-dimensional velocity head probe.

The measurements show that the radial inlet geometry induces a counter-rotating vortex pair that evolves into a single vortical secondary flow structure a short distance after the inlet. The location and manner in which the vortex pair merges into a single vortex affects the flow rate measurement accuracy in the inlet region of the stack.

It was also found that for measurement locations close to the inlet, the axial velocity field and the strength of the secondary flows affect average resultant angles and flow rate measurements. At a location 1.1 diameters from the inlet, changing the orientation of a two-traverse measurement set can either underestimate or overestimate the flow rate measurement by as much as 4.3%.

Three dimensional velocity probe data and numerical results were used in conjunction with S-probe error data reported in the literature to estimate S-probe bias error in flow rate. The radial inlet produces a high radial velocity region. Since S-probes are particularly sensitive to radial velocity, flow rate measurement error as large as 9.56% were observed.

The flow field was modeled numerically using a two-equation turbulence model (RNG k-ε). A comparison between the experimental and numerical secondary flow patterns showed that the RNG *k*-ε turbulence model, although able to predict the qualitative behavior of the flow field after the inlet, cannot predict how the flow evolves due to the presence of strong concentrated vortices.

Introduction

Background

Industrial societies are characterized by their large consumption of energy, the production of which is accomplished mostly by burning fossil fuels, i.e. coal, oil and natural gas. The combustion of fossil fuels produces energy in the form of heat and a number of by-products in both solid and gaseous states. For industrial applications, heat is utilized as is, or is converted into electricity. Combustion by-products are either collected for disposal, e.g. solid by-products such as fly-ash, or released into the atmosphere by means of stacks, e.g. gaseous by-products such as CO_2, CO, SO_X and NO_X. The emission of these gases is in the form of a homogeneous mixture commonly referred to as "flue gas."

In the United States, environmental issues have warranted the need for improved emission monitoring, resulting in mandated methods and procedures. Congress empowered the Environmental Protection Agency (EPA) by enacting the 1990 Clean Air Act (CAA) program for acid-rain control. This legislation, stated in the Code of the Federal Registry (CFR), CAA title IV "Acid Rain Deposition Control Requirements" sets limits on the amount of specific air pollutants the nation can emit. The program objectives are to monitor, control and ultimately reduce SO_2 and NO_X emissions that contribute to acid rain.

With the Clean Air Act as the driving force and the EPA as the implementer, stationary sources such as fossil fuel electric generating stations have been forced to adhere to the new regulations. As a result of CAA title IV virtually all electric utility power plants have been required to install Continuous Emission Monitoring (CEM) systems for SO_2, NO_X, CO_2 and stack volumetric flow rate. CEM data are also used (using fuel F-factors, CO_2 concentration, O_2 concentration, and volumetric flow rate) to obtain boiler heat inputs and, subsequently, unit heat rates [Energy Research Center, June 1998]. McRanie & Dene [1996] report that since the installation of CEM systems, many plants have found that the heat input rate as determined by CEMs is higher (by 5-25%) than determined by conventional methods. Since all methods should give equivalent results this discrepancy is disconcerting and thermodynamically improbable. The report goes on to conclude that the major cause of the problem is volumetric flow rate measurement error in CEM systems (Figure 1.1). This would agree with comments by Elliot [1995], and Levy et al [1997], in which flow rate error can be as high as 20%.

The power generation industry is subject to regulations that impose strict emission limits and steep penalties for exceeding them. Title IV of the Clean Air Act considers large fossil-fired powerplants as major sources of SO_2 and NO_X emissions, and has established the concept of "emission allowance." Under this concept, each utility is assigned the right to emit a specific amount of SO_2 per year as it generates electricity. One SO_2 allowance is equivalent to one ton of SO_2. Measuring volumetric flow is a fundamental component of SO_2 allowance

tracking and, if high, results in excess SO_2 allowances being used. Allowances can be bought and sold on the open market (~ $100 per Ton, Figure 1.2). Therefore, the use of excess allowances can have a significant impact on a plant's operating cost.

As previously mentioned, some utilities have had adverse experiences while implementing EPA regulations dealing with the computation of mass flow. Continuous Flow Monitoring Systems must meet certain accuracy standards set by "CAA 40CFR Pt. 75." The EPA's mandated means for determining this "relative accuracy" is contained in CAA "40CFR Pt. 60 Appendix. A, Method 1 and 2." The aforementioned describe the procedures by which experimental velocity data in a stack are to be collected and processed. This method, referred to as the " Equal Area Method" additionally specifies the measuring instrument to be used, i.e. a "Stausscheibe" or reverse type Pitot tube (S-probe). The basis for the Equal Area Method is the division of the stack cross section into equal annular sector areas. It is assumed that the measured velocity at the area centroid is representative of the average velocity in that area. For a given number of measurement points, ***N***, the computed mass flow $\dot{m}$ is given by

$$\dot{m} = \rho \, \Delta A \sum_{i=1}^{N} V_i \qquad (1.1)$$

where ΔA is the total area *A* divided by *N*, ρ is the density of the stack gas, and V_i is the measured axial velocity.

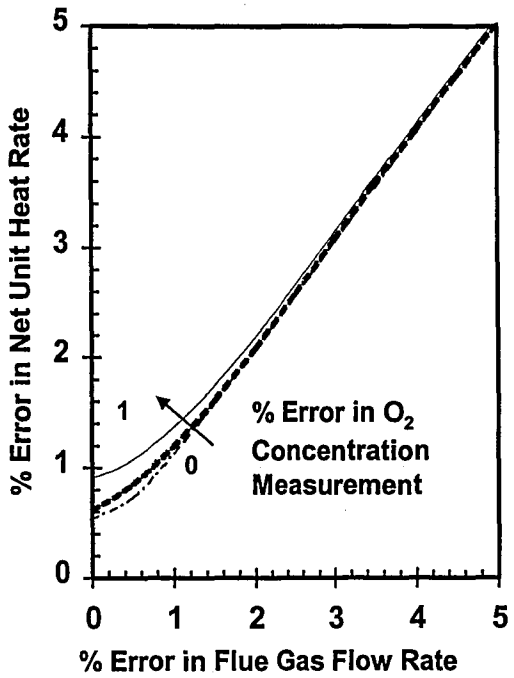

Figure 1.1 Measurement Accuracy of the O2 Based F-Factor Method

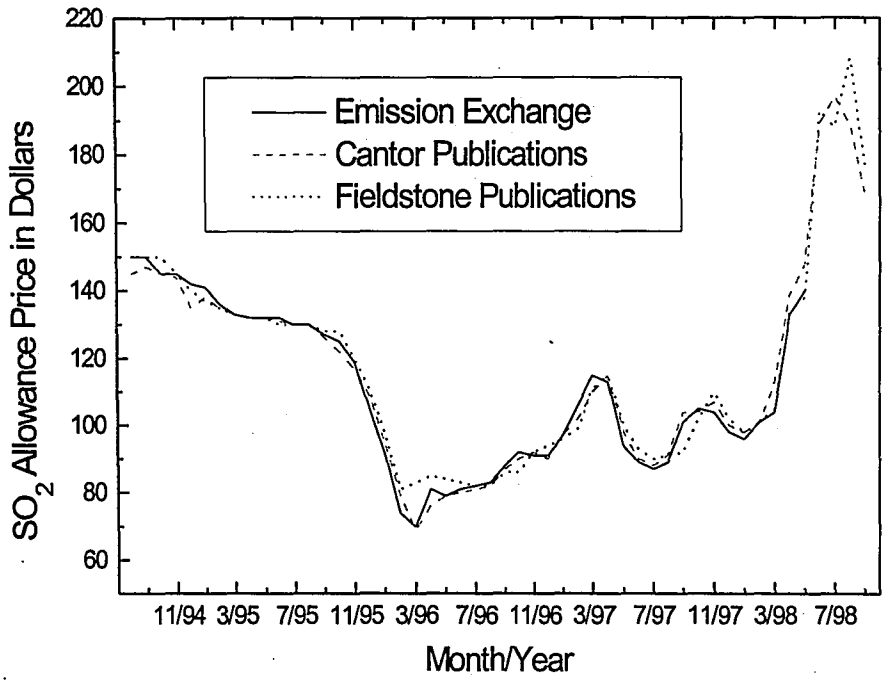

Figure 1.2 Monthly Average Price of Sulfur Dioxide Allowances Under the Acid Rain Program, Reference Prices Reported by the Brokerage Firms and the Fieldston Publications, Market Survey are Rounded to the Nearest Whole Dollar, Reference [7]

The Equal Area method introduces a positive bias error into the calculated flow rate by ignoring the no-slip condition at the wall [Elliot 1995, McRanie & Dene 1996, Levy & Eldredge June 1997]. A second source of error results from use of the S-probe in the presence of "mild" cyclonic flow ($\overline{RA} < 20°$) [McRanie & Dene 1996, Levy et al January 1997].

EPA regulations limit the average resultant angle ($\overline{RA}$) present in the stack to less than 20°. The average resultant angle at a point is the angle between the velocity vector V_T and a line parallel to the stack axis passing through the point. The average resultant angle is the arithmetic mean of the resultant angles at the equal area locations. Although the average resultant angle is indicative of the secondary flow strength, it cannot describe by itself such complicated fluid mechanics behavior. Different secondary flow patterns have the same average resultant angle, depending on their swirl intensity. The secondary flow pattern is dictated for the most part by the inlet geometry. Common stack inlet geometries are presented in Figure 1.3. Radial inlet configurations are probably the most common, and are the emphasis of this study. Although radial inlets give a relatively low average resultant angle, they also give rise to relatively complicated secondary flow patterns. Offsetting the inlet to one side tends to induce a uniform rotating motion in the flow (augmenting the $\overline{RA}$). The degree of offset determines the center and strength of rotation, with the extreme case being a tangential inlet geometry.

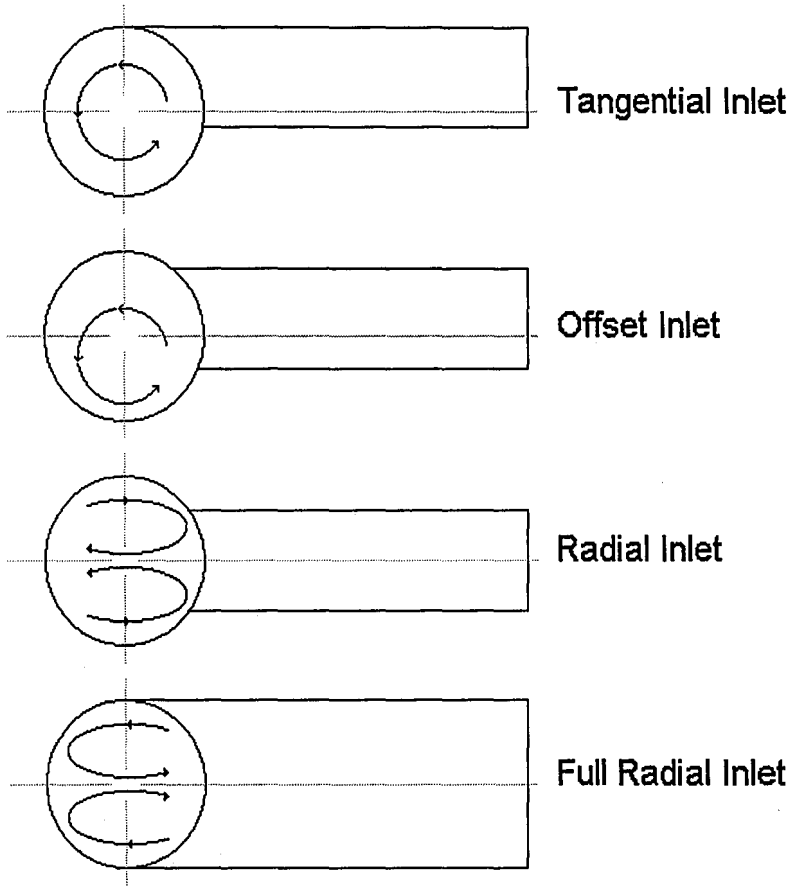

Figure 1.3 Stack Inlet Geometries and Qualitative Secondary Flow Patterns

Problem Statement

Power plant stacks are basically conduits for discharging combustion gases into the upper atmosphere. As the inlet stream is forced into the stack, the flow abruptly changes direction. As a result the velocity distribution becomes highly non-uniform, generating secondary flows in cross-stream planes downstream of the inlet. The strength of the secondary flows at the measurement location can significantly affect flow rate measurement accuracy.

The objective of the present study was to perform a laboratory and computational investigation of the characteristics of the flow occurring in a scale model of a stack with a radial inlet geometry. The model dimensions are 0.4572 m (18 in) in diameter and 12.1 m (476.4 in) in length. Average axial velocity is approximately 37 m/s (121.4 ft/s). Three-dimensional velocity measurements were collected in the inlet region using a type DA three-dimensional velocity head probe.

The flow field was modeled numerically using a two-equation turbulence model (RNG k-ε). The velocity field $\mathbf{V(V_r,V_\theta,V_Z)}$ characteristics were evaluated and compared with experimental data to determine the validity of computational fluid dynamics studies on flow rate error analysis. Once similarities and discrepancies between simulation and experimental data were established, appropriate conclusions were reached on how to best interpret the results.

Chapter 2

Experimental Test Facility

Laboratory Apparatus

The objective of the present study was to perform a laboratory and computational investigation of the characteristics and dynamics of the flow field occurring in a scale model of a stack with a radial inlet geometry. This research was conducted on a model stack previously developed in studies by Dalbec [1993] and Levy et al [1997]. In order to study the flow field in more detail, the model was slightly modified to accommodate an increased number of measurement ports, and a steadier inlet velocity profile.

The study concentrated on the region beyond the inlet where the velocity field is still evolving towards fully developed flow and presents strong secondary flows. The model stack is laid down horizontally, parallel to the floor. Since the flow is isothermal, there is no stack effect caused by buoyancy forces, and the flow pattern is defined by the geometry and the inlet velocity profile.

At the inlet of the model stack, a fan forces ambient air through a rectangular duct which joins the circular duct at a right angle to form the model's radial inlet (Figure 2.1). The circular duct diameter is 0.4572 m (18 in), while the rectangular inlet duct dimensions are 0.57309 m × 0.28416 m (22 9/16"×11 3/16"). The inlet duct has an aspect ratio of 2:1, resulting in a equivalent cross sectional area to that of the circular duct (Table 2.1).

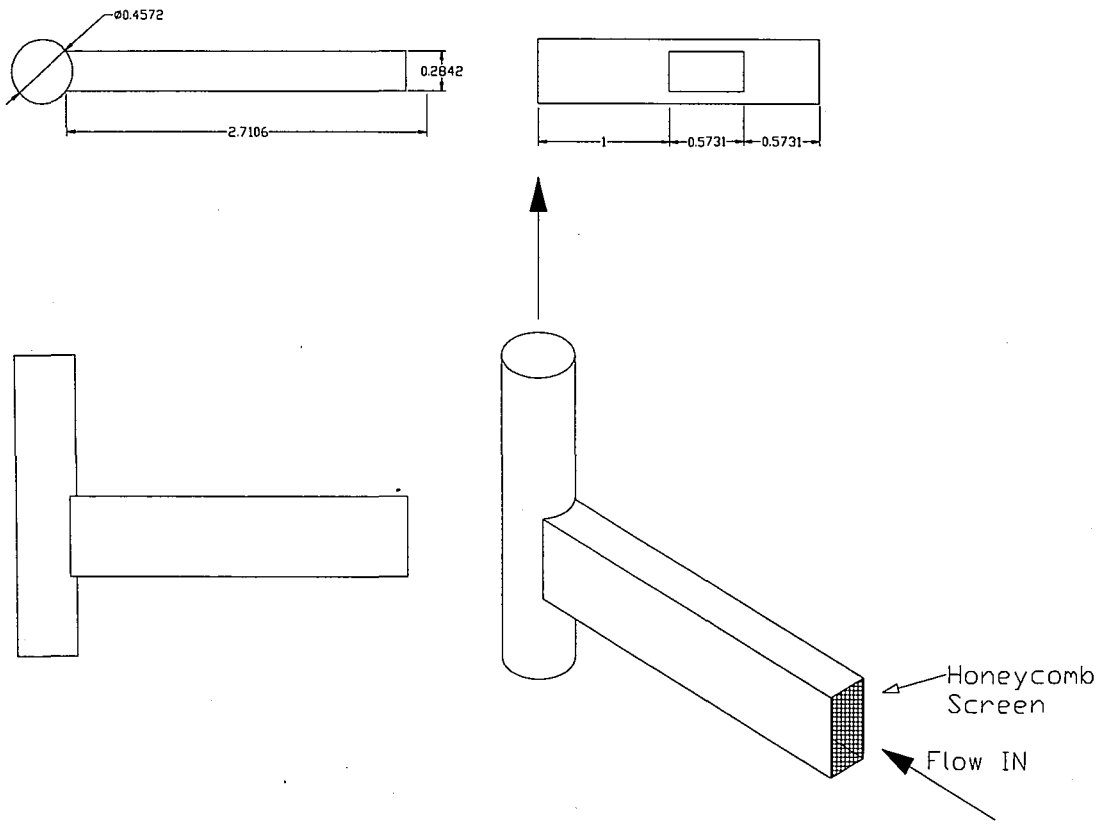

Figure 2.1 Radial Inlet Geometry, dimensions in meters

Table 2.1 Ductwork Dimensions

Duct Section	Dimensions [m]	D_H=(4 A/P) [m]	L [m]	A [m^2]
Rectangular	0.5730875×0.2841625 (22 9/16"×11 3/16")	0.37993	3.8	0.16285
Circular	0.4572 (18")	0.4572	12	0.16417

To improve flow quality in the test section, the model was modified by inserting a honeycomb screen at the fan exhaust. This stabilized the flow and removed swirl from the inlet stream. With this restriction, the average axial velocity in the circular section V_Z varies from 35 to 40 m/s (114.82-131.23 ft/s), depending on atmospheric conditions. The complete model stack is 12.07 m (475.37 in) in length and is shown in Figure 2.2.

The model stack is constructed from galvanized sheet-metal sections (thickness 1/32") with nominal lengths of 0.9144 m (36 in). In order to secure the probe at the measurement location, a special section was manufactured from 1/4" thick sheet metal. This "collar section" has 8 locations (measurement ports) spaced every 45°, to which the probe's traversing mechanism can be attached (Figure 2.3). If different orientations are needed the collar is rotated to the desired angular position. The measurement plane is varied by changing the axial location of the collar along the length of the stack.

The fan connected to the rectangular inlet duct is a centripetal fan, model number HDBI-240, manufactured by Cincinnati Fan and Ventilator Company, Inc. It produces a pressure head of 0.381 m (15 in) H_2O and a volumetric flow rate of 4.883 m^3/s (~10347 CFM) when operated at 29.828 kW (40 hp) and 2500 RPM.

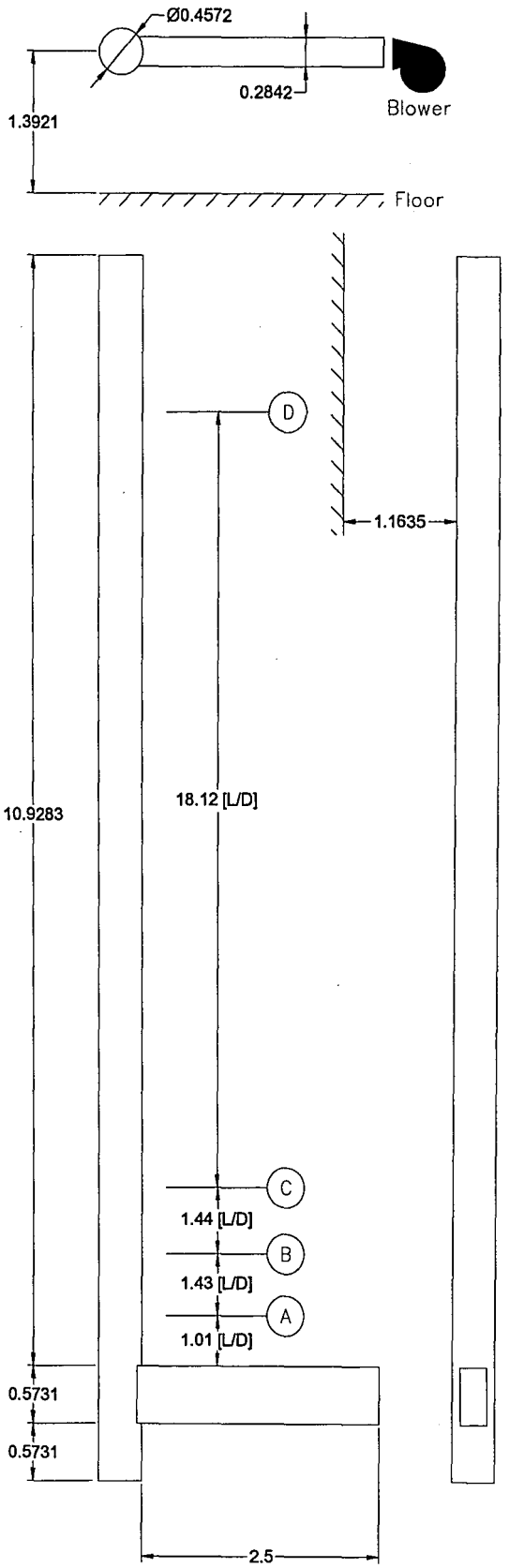

Figure 2.2 Model Stack, dimensions in meters

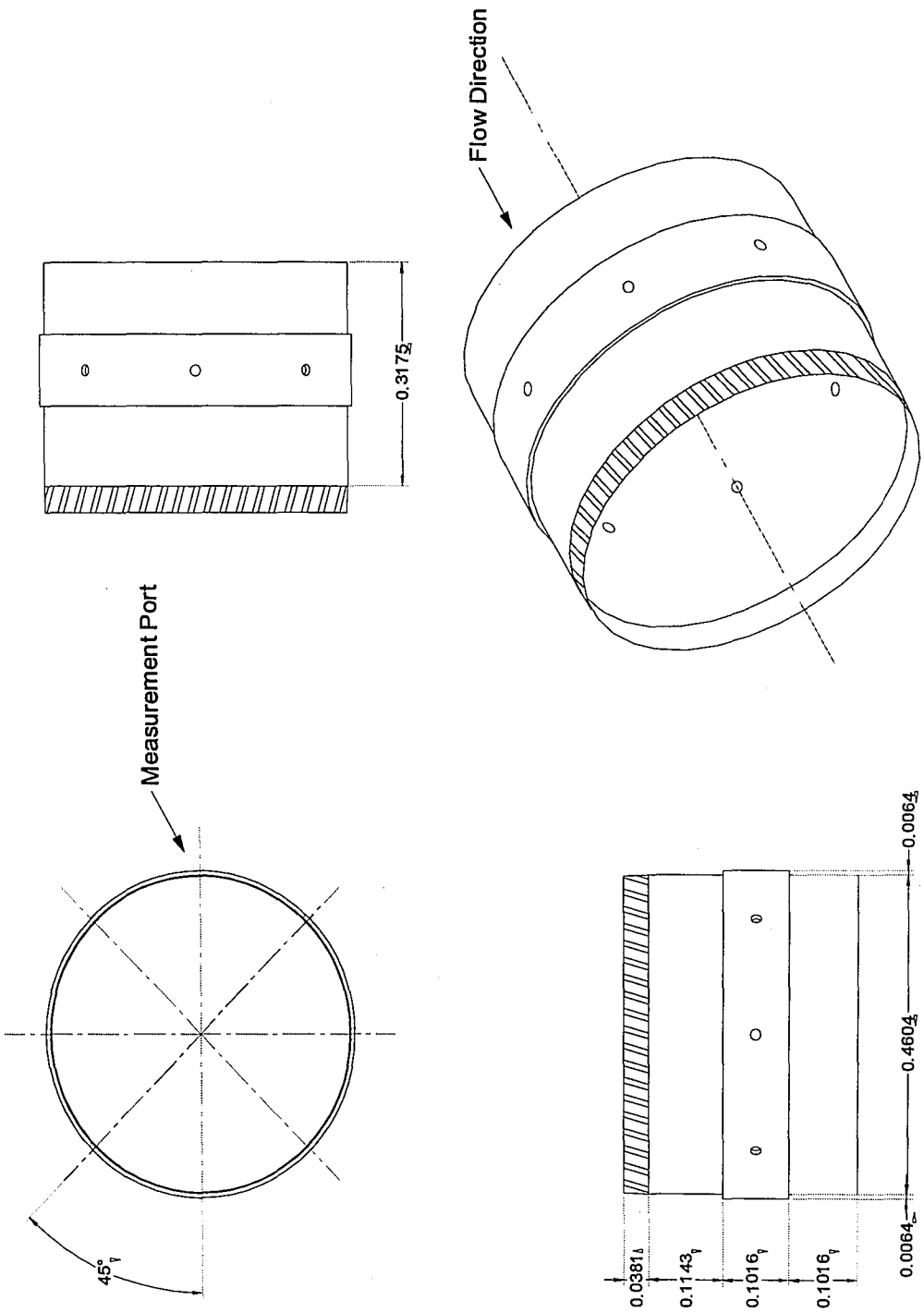

Figure 2.3 Collar Section, dimensions in meters

Design Rationale

To ensure the results and conclusions of this work are relevant to a full-scale application, flow conditions have to be similar. To achieve similarity, relevant dimensionless parameters need to have the same corresponding values for the model and the prototype [White, 1990].

The first requirement to consider is geometric similarity. The model and prototype are geometrically similar if and only if all body dimensions in all three coordinates have the same linear scale ratio, and all angles and flow directions are preserved. The second requirement is dynamic similarity in which the model and the prototype have the same length-scale ratio, and force-scale ratio.

For an incompressible flow with no free surface, it is sufficient to have the same Reynolds numbers. However, for the model and prototype flows being in the fully turbulent flow regime ($Re_D>10^4$), identical Reynolds numbers, or exact dynamic similitude is not a requirement [Gretta, Grieco, 1995].

The Reynolds number is calculated as

$$Re_D = \frac{\rho V_Z D_H}{\mu} \qquad (2.1)$$

where V_Z is the mean flow velocity in the main flow direction, ρ and μ are the fluid density and viscosity respectively, and the hydraulic diameter D_H is defined as:

$$D_H = \frac{4A}{P} \tag{2.2}$$

The parameter *A* is the cross-sectional area normal to the duct centerline, and *P* is the perimeter enclosing it.

Supposing the model stack were a 1/10th scale model of a power plant stack, using average values of axial velocity V_Z reported in Reference [1] and dry air at standard conditions (P=101.3 kPa, μ=18.64×10^{-} [Pa s]), we see that the corresponding Reynolds Numbers for both cases are of the same order of magnitude and well into the turbulent flow regime (Table 2.2).

Table 2.2 Model Stack and Full Scale Prototype Flow Regimes

	L [m]	D [m]	T [K]	μ=[Pa s]	ρ [kg/m^3]	V_Z [m/s]	Re_D
Model	12	0.4572	298.15	183.6×10^{-7}	1.17003	35	~1.0×10^6
Full Scale	120	4.572	422	239.7×10^{-7}	0.81658	17.5	~2.7×10^6

Chapter 3

Measurement Techniques and Procedures

Measurement Locations

The present study called for the measurement of the velocity field at different axial locations in a scaled model of a power plant stack. Information on the measurement planes is presented in Table 3.1. Velocity measurements were carried out at these locations using total velocity head probes.

Table 3.1 Measurement Locations

Location*	Distance from Inlet[m]	Distance from inlet [L/D]	Number of Measurement Points
Station A	0.50 [m] (19.7")	1.10 Diameters	160
Station B	1.12 [m] (44")	2.44 Diameters	160
Station C	1.78 [m] (70.1")	3.88 Diameters	160
Station D	9.40 [m] (370")	20.56.Diameters	40

The duct cross sectional measurement planes were divided into a number *n* of equal annular sector areas, with the measurement locations the centroids of the equal areas. Figure 3.1 shows the model stack circular cross-section divided into 80 equal areas. The shaded region is an annular sector area, and the crosshairs mark the area's centroid. This subdivision is the basis for the equal area method presented in "CAA 40 CFR Pt 60. Appendix A, Method 1," and explained in more detail in Chapter 6.

* The Distance is measured from the downstream corner of the inlet breaching (Figure 2.2).

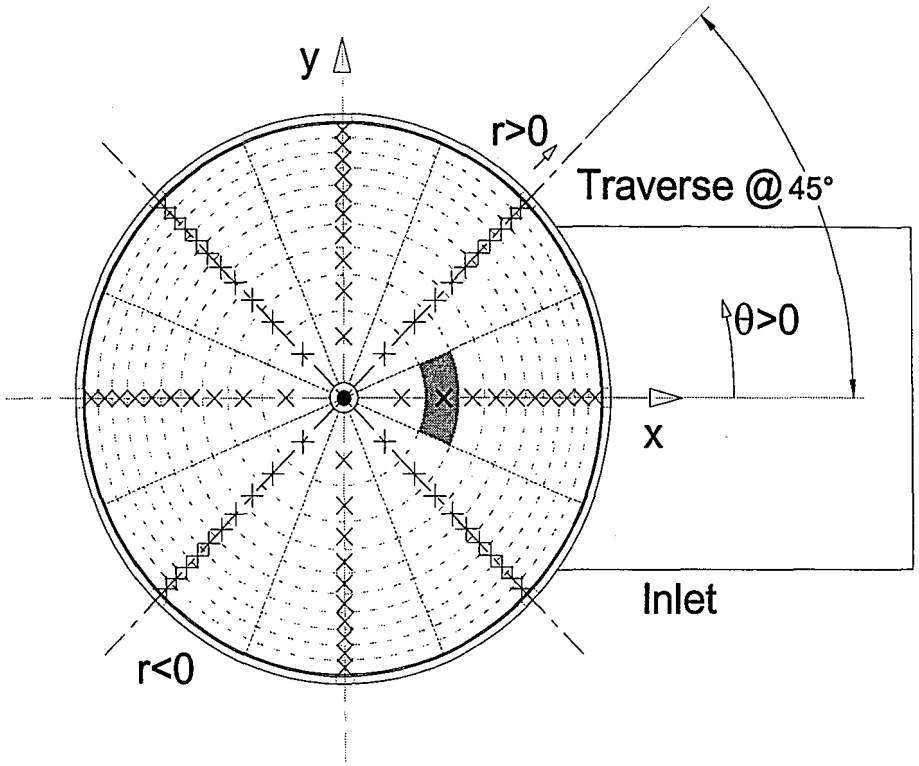

Figure 3.1 Stack Cross-Section Divided into 80 Equal Areas

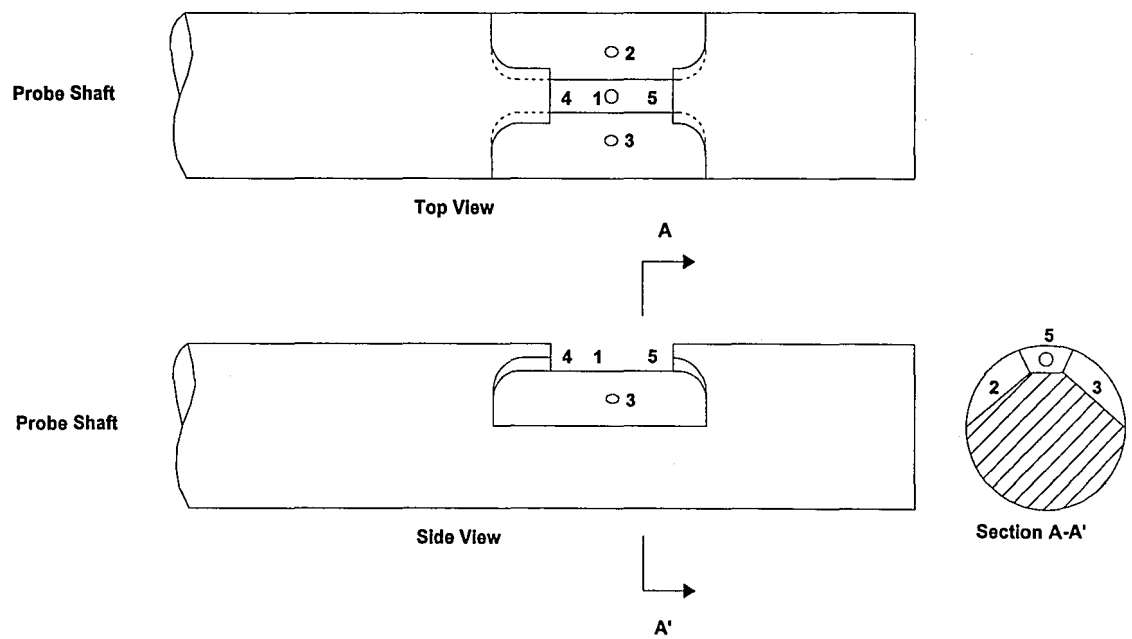

Figure 3.2 Prism Probe Tip

Instrumentation

In the present study, experimental velocity data were generated using a type DA "3D" directional (Prism) probe and a Pitot static tube. Three-dimensional velocity data in cylindrical coordinates, i.e., $V(V_r, V_\theta, V_Z)$, were obtained using the "3D" Prism probe. The Pitot static tube was used at locations with low secondary flow strength, where data on axial velocity V_Z was desired. The procedures used to convert dynamic pressure into velocity are described in detail in the appendix entitled Total Velocity Head Probes.

The five-hole type DA "3D" probe was used for the measurements performed in this laboratory investigation. The probe is model number DA-125-24-F-22-CD, serial number B-2645, manufactured by United Sensor Corporation (Figure 3.2). The probe's shaft is 0.61 m (24 in) in length and 6.35 mm ($^1/_4$ in) in diameter. Its tip is 50.8 mm (2 in) in length and 2.77 mm ($^7/_{64}$ in) in diameter. For the present study the vendor calibration curves were used when calculating velocities from the pressure drop. These curves can be found in the appendix entitled Total Velocity Head Probes and in Reference [32].

The Pitot probe used for the experiments, model number USC 603-672-0909, was manufactured by United Sensor Corporation. The probe's shaft is 0.61 m (24 in) in length and 6.35 mm ($^1/_4$ in) in diameter. Its tip is 38.1 mm (1.5 in) in length and 2.38 mm ($^3/_{32}$ in) in diameter. For this probe ASTM recommends a value of the pressure coefficient *C=0.9975*. However, for the present study the value *C=1.000* was used when calculating velocities from the pressure drop.

A traversing mechanism with a protractor mounted on its traversing fixture was used to align and position the probes. The mechanism allows for the probe's movement in the radial direction and rotation about its axis (yaw). By attaching the traversing mechanism to the collar, the probe tip can be radially located within $\pm 2.54 \times 10^{-4}$ m (± 0.01 in) and the yaw angle can be found within $\pm 0.2°$ inside the duct (Figure 3.3). The "manual traverse unit," model number USC1000-24, manufactured by United Sensor Corporation, can accommodate a probe with a length of up to 0.61 m (24 in) and a diameter of up to 6.35 mm (0.25 in).

Pressure measurements were carried out using a 0.254 m (10 in) H_2O inclined manometer and a double 0.0381 m (1.5 in) H_2O inclined manometer, both manufactured by Merriam Instrument Company. Scale divisions for the equipment are 2.54×10^{-4} m (0.01 in) of H_2O. Specific information for each instrument is presented in Table 3.2.

Table 3.2 Manometer Information

Manufacturer	Model	Serial No	Range	Precision
Merriam Instrument Co.	43GD10	Z56451	0.0381 m	2.54×10^{-4} m (0.01 in)
	40HEX35WM	196940J1	0.254 m	

Measurement Procedure

Once measurement locations were established, velocity measurements were taken at each point. In order to keep track of all the information generated by the experiments, computer spreadsheets were developed to post-process the data. This permitted the comparison of data from different sets by forming accurate representations of the secondary flows in different formats. For every measurement point, the following information was recorded:

- Ambient conditions, i.e., airflow temperature T_{AIR}, barometric pressure P_{ATM}, humidity ϕ_{AIR}.

- Spatial location of the measurement point, i.e., axial location of the measurement plane z, tangential location of the radial traverse θ, and radial position of the point along the traverse r.

- Three-dimensional velocity measurements obtained from the prism probe. Measured as a differential pressure $(P_1\text{-}P_2)$ for the total velocity V_T, a differential pressure $(P_4\text{-}P_5)$ for the pitch angle β, and a yaw angle α from the protractor. When post processing, the velocity data are converted into Cylindrical $V(V_r, V_\theta, V_Z)$ and Cartesian $V(V_X, V_Y, V_Z)$ form.

- When using the Pitot static tube, a one-dimensional velocity component is measured as a differential pressure value P_T for the axial velocity component V_Z.

Velocity measurements were carried out at points located along radial lines referred to as "radial traverses." The measurements in this study were grouped into 20 point traverses that are composed of two opposed 10 point radial traverses. Traverses and x-y plots are referenced by their axial and tangential location, e.g., Station A, traverse @ 45° (Figure 3.1).

Once the probe head is stationed at the desired location, dynamic pressure readings were taken by square root averaging a number of pressure values using a handheld calculator. This reduced the uncertainty produced by small fluctuations in the manometers. Each point-wise experimental pressure data point recorded in this study used 30 instantaneous pressure values to produce a time-mean response.

$$\overline{P} = \frac{\sqrt{\sum_{i=1}^{n} P_i^2}}{n} \tag{3.1}$$

Barometric pressure, relative humidity and air temperature were measured for each set of data in order to determine conditions at the time the experiment took place. Because of the large number of measurement locations, a complete set of measurements required several days of testing. During the course of such a test sequence, small changes in flow rate through the test section occur due to changes in inlet air density. To compensate, the measured velocities were corrected to standard density conditions through the use of the following equation:

$$\frac{V_S}{V_m} = \sqrt{\frac{\Delta P_S \, \rho_m}{\Delta P_m \, \rho_S}} \qquad (3.2)$$

where V is the average axial velocity, Δp the pressure drop from the inlet duct to the stack exit, ρ the air density and the subscript m and s denote measured and standard conditions respectively.

Equation 3.2 assumes the pressure drop from the inlet duct to the exit of the stack varies with V^2, and it thus assumes the duct friction factor and inlet loss coefficients are constant for small changes in velocity, Reference [14].

When measuring in a circular cross section, and as long as the prism probe is traversed radially, the resulting pressure differences will be aligned with tangential and radial components of velocity defined in a cylindrical coordinate system with its origin along the stack centerline. This is convenient because the measured flow quantities, total velocity V_T, yaw α, and pitch β, are easily transformed into velocity components in cylindrical form, i.e., axial V_Z, radial V_r and tangential V_θ velocities, by use of the following equations:

$$\begin{aligned} V_Z &= V_T \cos(\alpha)\cos(\beta) && \text{(a)} \\ V_r &= V_T \sin(\alpha) && \text{(b)} \\ V_\theta &= V_T \cos(\alpha)\sin(\beta) && \text{(c)} \end{aligned} \qquad (3.3)$$

The resultant angle RA at a point is defined as the angle between a line parallel to the stack axis and the velocity vector $\overline{V_T}$, and is calculated using the following:

$$RA = \arccos(V_Z / V_T) = \arccos(\cos(\alpha) \cdot \cos(\beta)) \tag{3.4}$$

The cylindrical coordinate system is oriented so that V_Z is positive in the direction of the flow parallel to the stack axis, V_r is positive when the flow moves away from the duct centerline, and V_θ is positive in counterclockwise rotation. Notice that when taking measurements, a positive yaw angle (counterclockwise rotation) registered on the protractor dial is a negative yaw angle in the flow and vice versa (Figure 3.4). To convert the velocity components in Cylindrical coordinates into velocity components in Cartesian coordinates we make use of the following:

$$\begin{aligned} Vx &= V_r \cos(\theta) - V_\theta \sin(\theta) \quad (a) \\ Vy &= V_r \sin(\theta) + V_\theta \cos(\theta) \quad (b) \end{aligned} \tag{3.5}$$

where the angle θ is the angular position of the point in the cylindrical coordinate system.

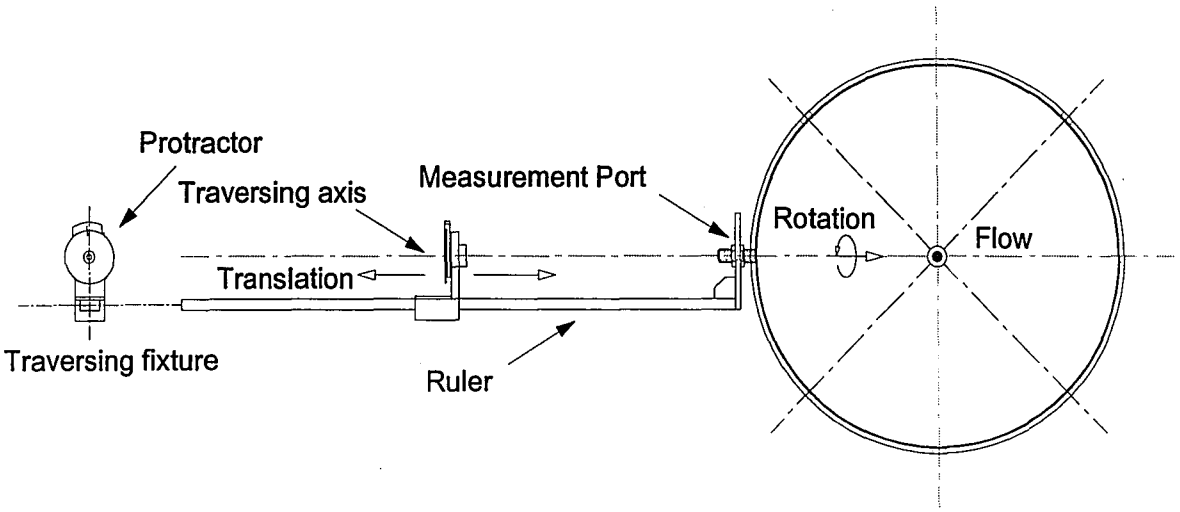

Figure 3.3 Positioning Mechanism Attached to Collar

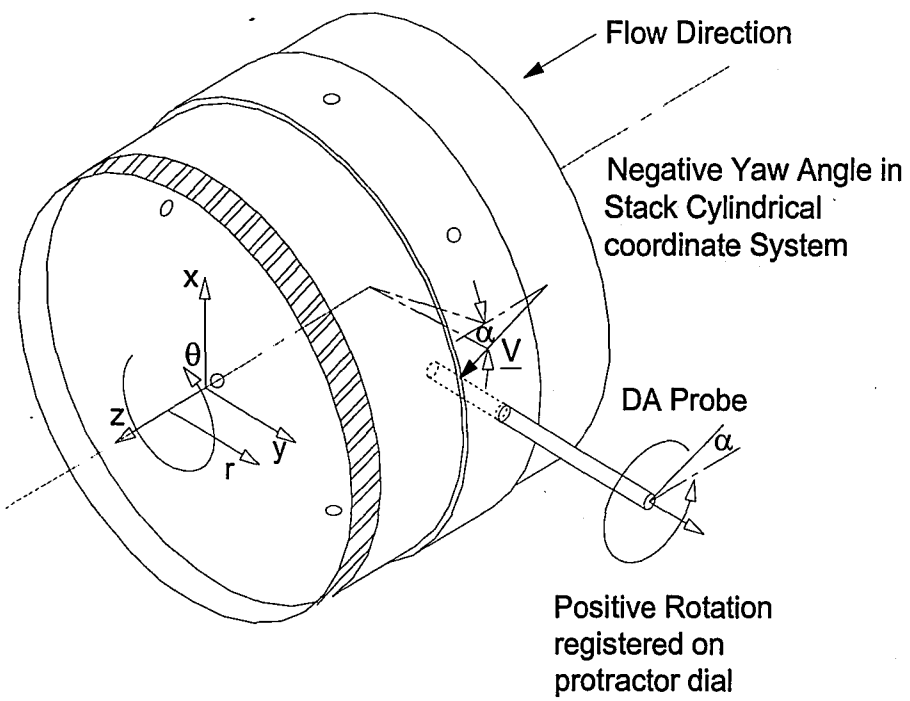

Figure 3.4 Orientation of 3D Probe in a Cylindrical Coordinate System

Measurement Error and Uncertainty

An error analysis was performed to determine the associated error in computed velocities. The objective is to assess the relative effect of uncertainties in primary measurements on velocity readings. Velocity measurements are prone to two types of errors, a bias (systematic) error *B*, and a random (precision) error Δ. The total error is the combination of both bias and random errors.

The overall uncertainty U is the largest expected error, and the interval $\bar{x} \pm U$ represents a band about a sample mean $\bar{x}$ within which the true value is expected to be. The uncertainty interval was computed by

$$U_{ADD} = \Delta + B = B + t \cdot \frac{S}{\sqrt{N}} \tag{3.6}$$

where *B* is the bias limit (error), Δ the random error, *S* the precision index, *t* is the *t* variable (for a 95% confidence level, and an error with a degree of freedom υ), and *N* is the number of measurements.

Experimental uncertainty is typically the largest value the error will have. The uncertainties of the independent variables are a function of their sensitivity coefficient $\partial Y / \partial x_i$ and their relative precision w_{Xi}. The error propagation in the dependent variable *Y* depends on the squares of the uncertainties in the independent variables x_i.

$$w_Y = \sqrt{\left(\frac{\partial Y}{\partial x_1} w_{X_1}\right)^2 + \left(\frac{\partial Y}{\partial x_2} w_{X_2}\right)^2 + \cdots + \left(\frac{\partial Y}{\partial x_i} w_{X_i}\right)^2} \qquad (3.7)$$

Equation 3.7 is used to determine both bias limit *B*, and precision index S_{Xi}.

The procedure followed to determine overall uncertainty in the velocity measurements was:

- List all independent measurement parameters.
- Define the functional relationship.
- Determine or estimate random and bias errors for each measurement parameter.
- Combine the random and bias errors.
- Calculate uncertainty in the final result.

The functional relationship for the prism probe total velocity calculation is given by Equation 3.8.

$$V_T = \sqrt{\frac{2 \cdot VPC \cdot \Delta P \cdot R \cdot T}{P_{ATM}}} \qquad (3.8)$$

Where VPC is the velocity pressure coefficient, ΔP is the dynamic pressure, *T* is the air temperature, P_{ATM} is the atmospheric pressure, and R=287 J/(kg K) is a constant for air. Using $V_T = V_T(VPC, \Delta P, T, P_{ATM})$ it is possible to determine the

sensitivity coefficients for each independent variable. Expected values with the same probability of B_X and S_X for a typical axial velocity were determined and are listed in Table 3.3.

Table 3.3 Prism Probe Uncertainties and Bias Errors

$$V = \sqrt{\frac{2 \cdot (1) \cdot (746.52\ \text{Pa}) \cdot (287\ \text{J/(kg} \cdot \text{K)}) \cdot (298.15\ \text{K})}{101325\ \text{Pa}}} = 35.508\ \frac{\text{m}}{\text{s}}$$

Variable	Typical Values	Relative Uncertainty	Bias Error
ΔP	746.52 Pa (3 in H_2O)	4.0%	12.442 Pa
P	101.325 kPa (29.92 in Hg)	0.2 %	84.65 Pa
T	298.15 K (77 °F)	1 %	2°K
VPC	1	0.05%	0.001

Using the functional relationship for velocity (Equation 3.8) and the values in Table 3.3, we compute a relative precision index $S_V/\overline{V}_T$, and a bias limit $B_V/\overline{V}_T$, using Equation 3.6. Assuming large sample size cases with 30 or more measurements, the value of *t* is equal to 2.0, which assumes that the results are normally distributed. The overall uncertainty in velocity is presented in Table 3.4.

Table 3.4 Prism Probe Overall Uncertainty

	% error
$S_V/\overline{V}_T$	1.032
$B_V/\overline{V}_T$	0.90063
$U_{V,ADD}$	2.96

An order of influence analysis shows that the main source of uncertainty in calculating total velocity is the VPC followed by the ΔP measurement. In our study the VPC was determined by curve fitting the manufacturer's calibration curves using piece-wise cubic polynomial interpolation, so both bias error and uncertainty are kept to a minimum for this quantity. The ΔP varies with velocity, so as the velocity decreases, the measurement uncertainty increases.

In order to determine whether the computed value of 3% in overall uncertainty in total velocity is reasonable, repeated measurements were taken at station C and B, traverses at 0° and 90°. Results show that for the axial velocity component, a 3% error is a sensible estimate of the uncertainty (Figure 3.5 and Figure 3.6). Uncertainty in the secondary flow measurements is higher, and quantifying it is harder because more parameters come into play. The resultant angle calculation has the combined uncertainties of total velocity, yaw and pitch. In locations with low secondary flow velocity such as Station C, resultant angle data show more scatter, and a higher overall uncertainty of the order of 20% (Figure 3.7 and Figure 3.8). Finally, although data resulted in coherent secondary flow patterns, secondary flow results should be analyzed with care.

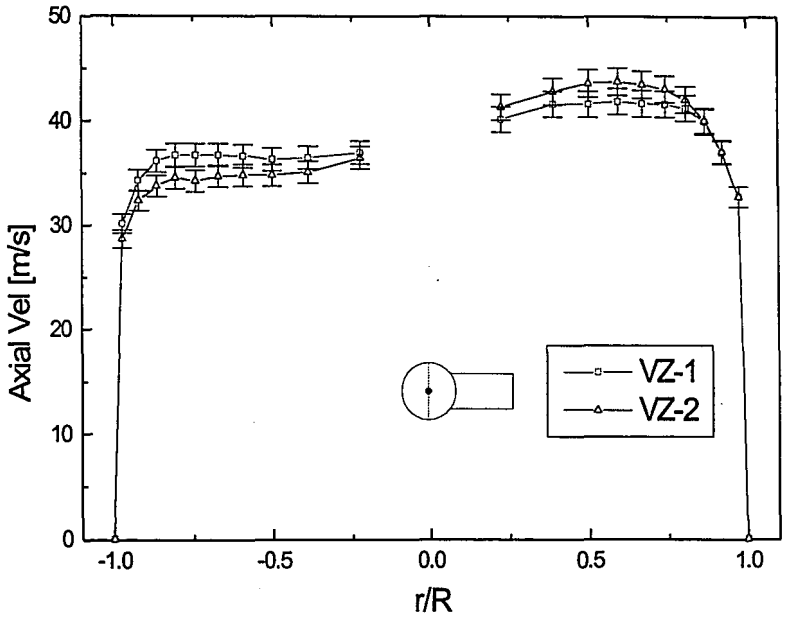

Figure 3.5 Axial Velocity at Station C, traverse @ 90°, Comparison between Repeated Measurements

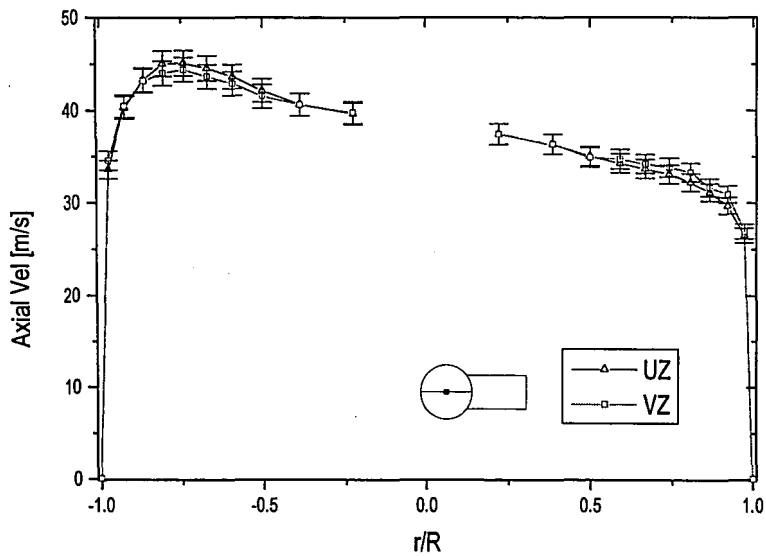

Figure 3.6 Axial Velocity at Station C, Traverse @ 0°, Comparison between Repeated Measurements

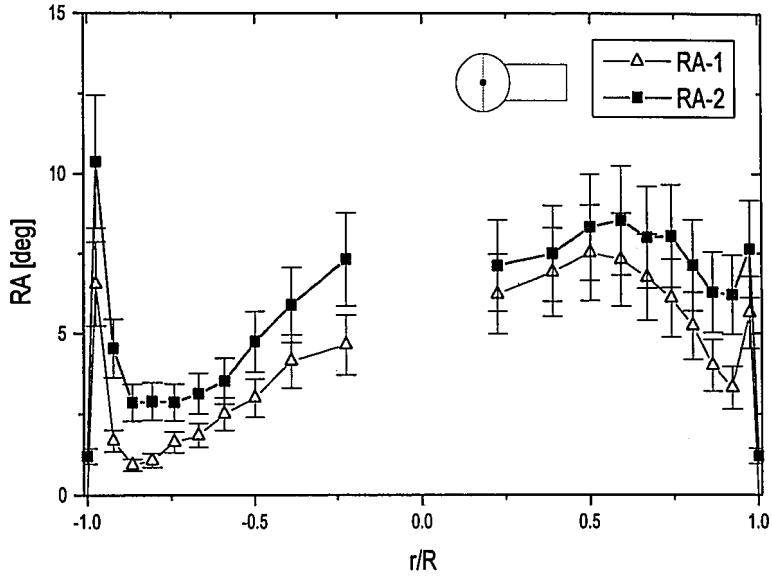

Figure 3.7 RA at Station C, Traverse @ 90°, Comparison between Repeated Measurements

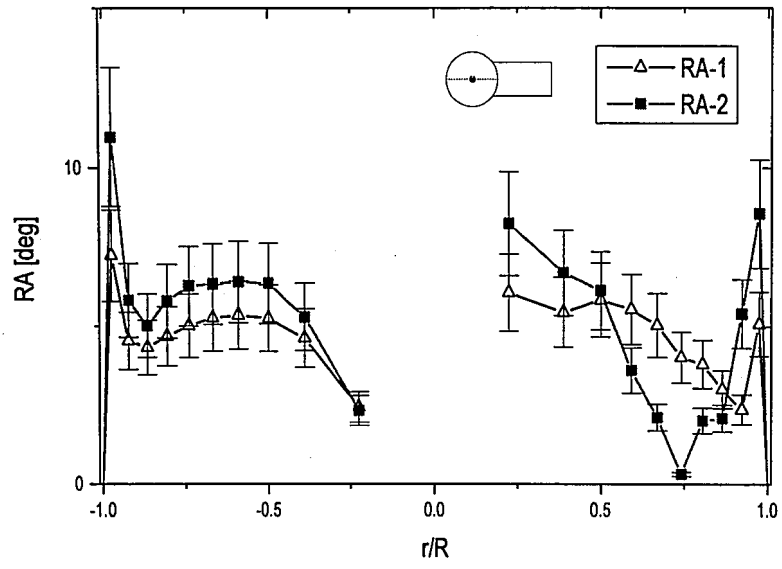

Figure 3.8 RA at Station C, Traverse @ 0°, Comparison between Repeated Measurements

Chapter 4

Flow in the Model Stack

Stack Flow

This chapter presents results obtained from experimental velocity measurements performed in the scale model of the radial inlet stack. The objective of the experimental study was to characterize and describe the flow developing near the inlet region. Experimental results of axial velocity, secondary flow, and swirl are presented for planes located at 1.01, 2.44, and 3.88 diameters from the downstream corner of the inlet breaching (Figure 2.2). The average axial velocity in the stack was approximately 37 m/s (121.4 ft/s). Three-dimensional velocity data were obtained using a five-hole type DA directional pressure probe.

The problem of turning flows in elbows and ducts and of mixing in T-junctions at moderate to high Reynolds numbers has been studied previously by a number of investigators. Results from the literature describe the qualitative behavior of the flow and the pressure drop due to turning geometries. For a detailed literature review see Idelchik I.E. [1994]. Prior work in the experimental setup used in this study by Dalbec [1993], and Levy et al [1997], deals with flow metering errors using total velocity head probes at stations located approximately 21 diameters downstream of the inlet. A detailed description of the flow field within 4 diameters of the inlet for this particular inlet geometry was lacking.

The flow can be characterized as an incompressible, isothermal, internal flow. The Reynolds number is of the order of 10^6, thus the flow is fully turbulent. The inlet geometry and the inlet boundary condition prescribe the flow field development throughout the model stack. The inlet air flow provided by the centrifugal fan is straightened by means of a honeycomb screen before entering the stack (Figure 2.1). This evenly redistributes the inlet flow and provides approximately uniform turbulence intensity.

The inlet stream advances through the inlet duct following the path of least resistance. Before turning, the flow velocity is lower at the bottom wall and larger at the top wall. The flow rate thus becomes unbalanced about the A-A' axis (Figure 4.1 a). The net effect of turning the flow at a sharp angle is, a considerable pressure drop, and a reduction of the effective cross-sectional area of the flow in the stack brought on by the establishment of various recirculation regions (Figure 4.2).

At the bend a diffuser effect occurs near the wall opposite the inlet, i.e. the flow slows down due to a change in area, and a nozzle effect occurs near the top wall, i.e. the flow accelerates over a recirculation eddy. The eddy zone formed as a result of the flow separation from the top wall at the sharp bend propagates far ahead and across the stack, reducing the cross section of the main stream. Thus, after the bend a diffuser effect occurs near the inlet wall, with a nozzle effect near the wall opposite the inlet.

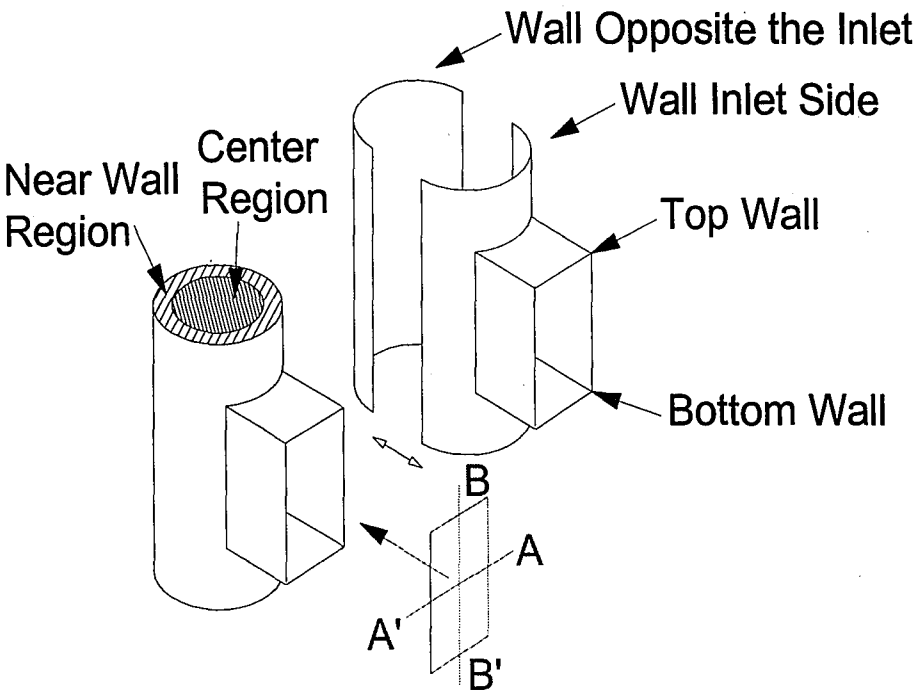

(a)

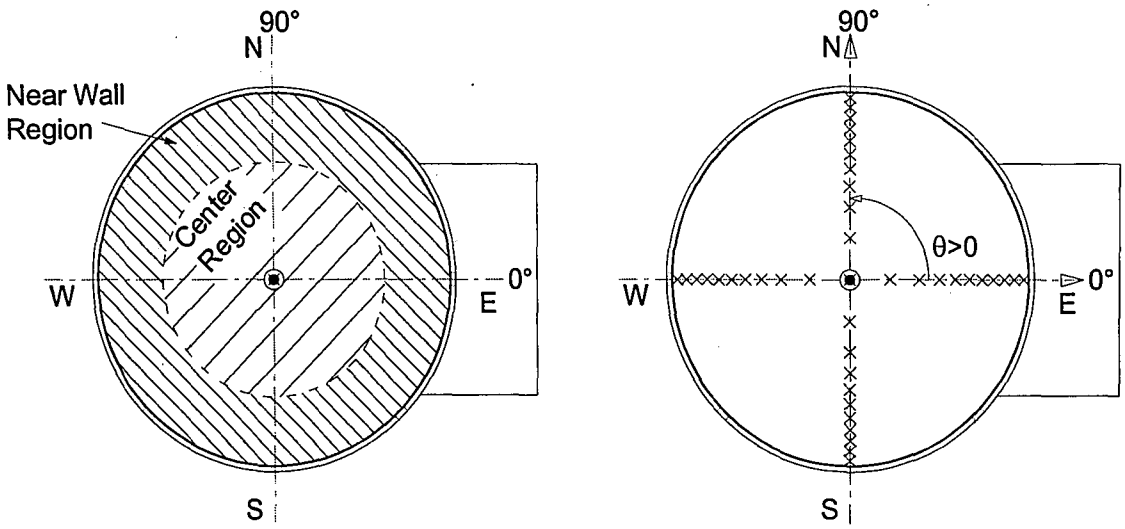

(b)

Figure 4.1 (a) Wall Locations and Flow Regions, (b) Flow Regions and Rectangular Inlet Duct Symmetry Axes, @ 0° and 90°

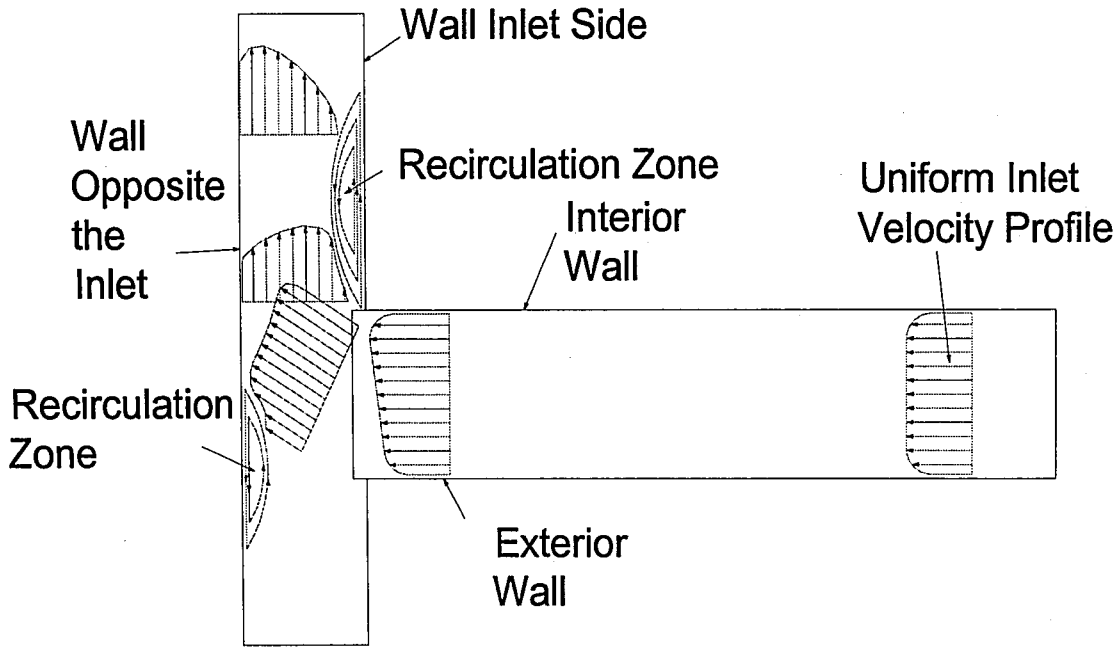

Figure 4.2 Inlet Region Flow

The resulting axial velocity field at Station A (1.01 diameters from the inlet) is highly distorted (Figure 4.3 a). The most prominent feature is the concentration of a higher velocity fluid in the near wall region of the duct (Figure 4.4 a). Moving downstream, at Station B (2.44 diameters from the inlet) the axial velocity profile redistributes itself (Figure 4.3 b). The center region has gained momentum by decelerating the higher velocity fluid still present in the near wall region, (Figure 4.4 b). By the time the flow reaches Station C (3.88 diameters from the inlet), it can be described as a developing turbulent velocity profile (Figure 4.3 c). Although the flow presents a concentration of higher velocity fluid at the S-E quadrant of the duct (Figure 4.1 a), the axial velocity is much more uniformly distributed over the cross-section (Figure 4.4 c).

Pressure losses mostly due to the formation of the eddy at the inlet side wall together with the secondary flow determine the nature of the velocity distribution downstream of the bend. The irregularity of the velocity profile, and its concentration in the near wall regions corresponds to the existence of centrifugal forces inside the flow brought about by the secondary flow.

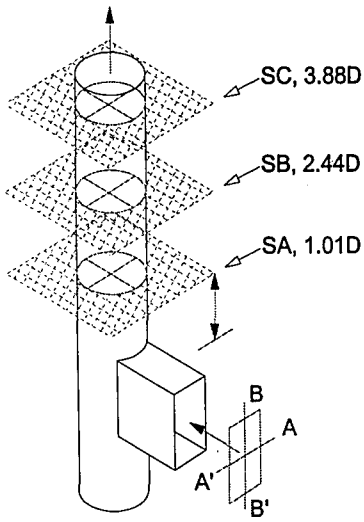

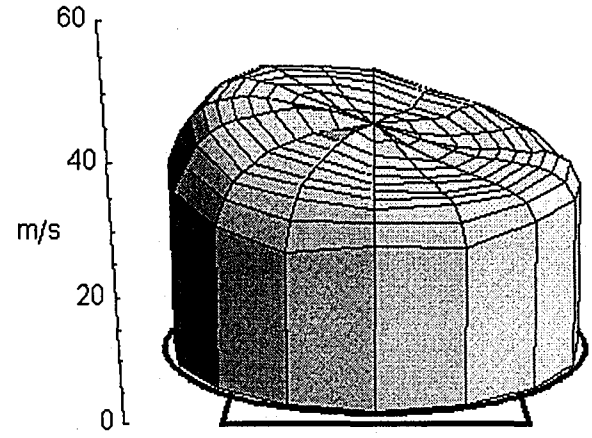

(c) Station C

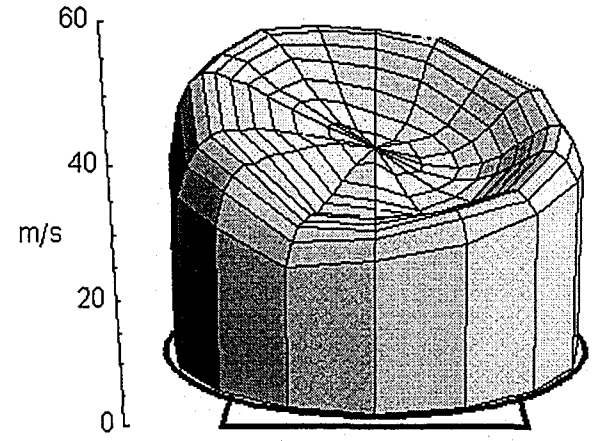

(b) Station B

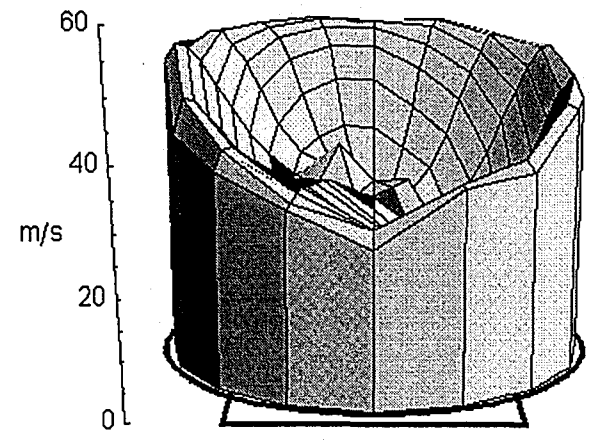

(a) Station A

Figure 4.3 Axial Velocity Field at Different Axial Locations, Radial Inlet is Normal to Page.

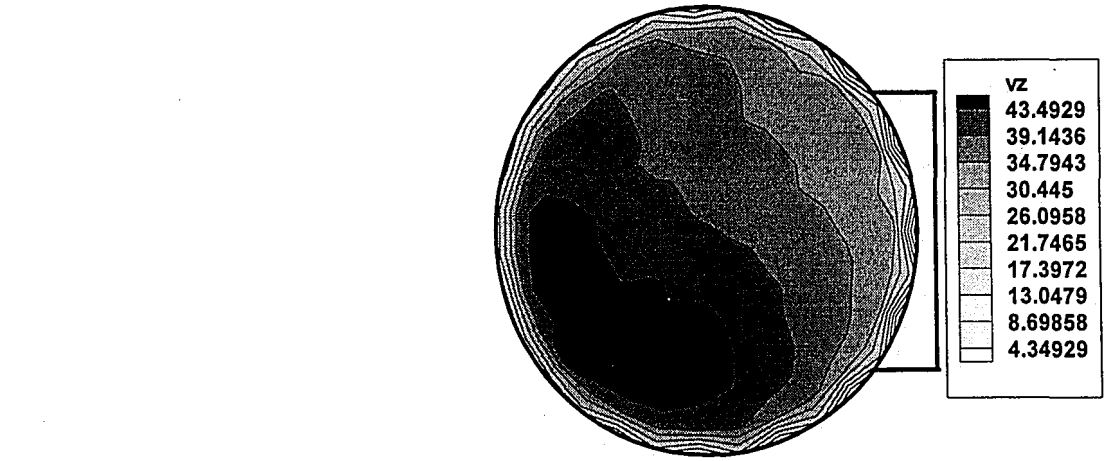

(c) Station C

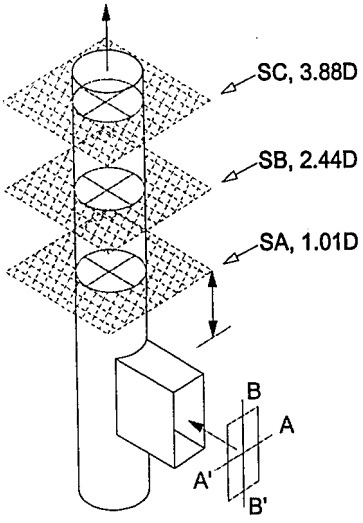

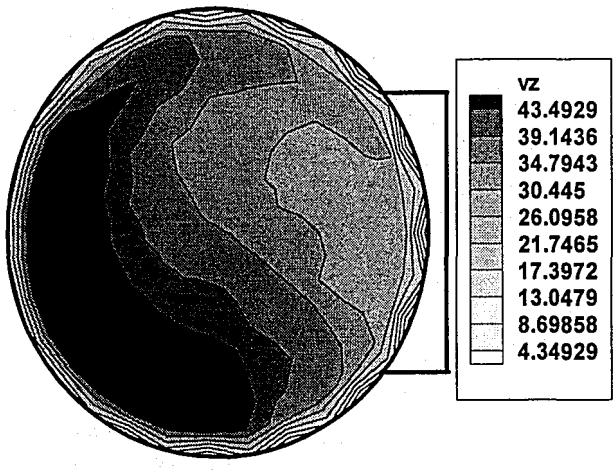

(b) Station B

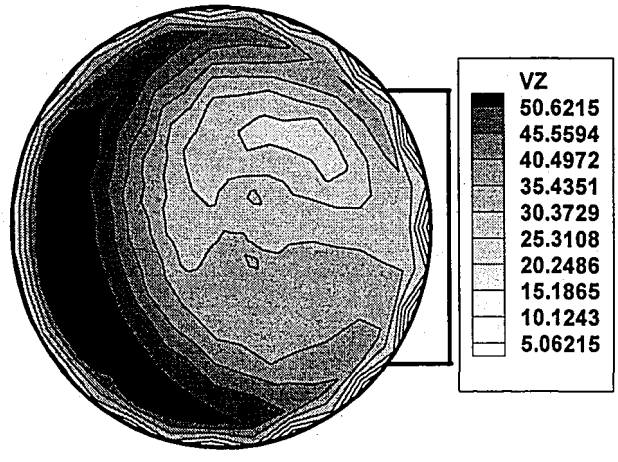

(a) Station A

Figure 4.4 Axial Velocity Distribution at Different Axial Locations.

The net effect of an uneven axial velocity profile is to bias flow rate calculations done with a limited number of velocity traverses. A case in point is the estimation of flow rate using only two perpendicular axial velocity profiles (four radial traverses). Asymmetric velocity profiles can result in an inaccurate estimation of the flow rate. This is explained in more detail in Chapter 6.

Secondary Flows

The appearance of centrifugal forces and the presence of boundary layers at the wall explain the occurrence of secondary (transverse) flows in cross-stream planes perpendicular to the stack axis. As the inlet stream expands on the sides of the inlet breaching and impinges on the wall opposite the inlet, separation from the wall on the inlet side is intensified by the inertial forces acting at the junction in the direction of the wall opposite the inlet. The centrifugal forces give rise to a counter rotating vortex-pair superimposed on the main stream parallel to the channel axis [Idelchik, 1997]. This two-cell vortex structure is peculiar to elbows and symmetrical turning geometries such as the radial inlet. The term "structure" is used here to describe a spatial flow pattern that remains identifiable for some period of time [Panton, 1996].

The vortical motion of the flow imparts a helical shape to the streamlines. The duration of the vortex pair is short lived as circulation in the vortices diffuses in the axial direction. At Station A (1.01 diameters from the inlet) both cells **X** and **Y** appear to have the same strength (Figure 4.5 a), although cell **Y** presents a slightly stronger circulation than cell **X**. The misalignment between the cell interface and the inlet axis is pronounced and of the order of 44°. The distortion of the axial velocity profile in the center region (Figure 4.3 a) is associated with the location where the cross-stream leaves the interior wall approximately 44° clockwise from the inlet duct centerline (Figure 4.5 a).

Further downstream, at Station B (2.44 diameters from the inlet) the two-cell vortex structure has broken down. Both counter rotating motions are still present in the flow but one structure has grown in size while the other one has shrunk (Figure 4.5 b). By the time the flow reaches Station C (3.88 diameters from the inlet), the flow is settling down into a more uniform swirling motion. Only a weak remnant of cell **X** remains (Figure 4.5 c).

The **X** vortex is located in a region of lower axial velocity. The relation between the shape of the axial velocity field and the secondary flow suggests that the flow asymmetry results in unequal axial convection of vorticity for each vortical structure. Also, slight irregularities in the model's geometry might cause the vortices to interact with each other, resulting in one vortex swallowing the other one.

The dynamic process occurring in the flow field leading to the disappearance of the vortex pair is not entirely understood. It would appear that at a high Reynolds number there is an increased instability associated with this type of wall bounded longitudinal vortex pair. Also, any difference in angular velocity between the two vortices would subject the interface between them to a shear stress, possibly increasing the rate of dissipation. As a final note, the vortex structures observed in this laboratory investigation must exist in a full-scale radial inlet stack. Their duration might be longer in terms of length, but it is clear that the vortex pair eventually evolves into a single vortex that loses strength along the length of the stack.

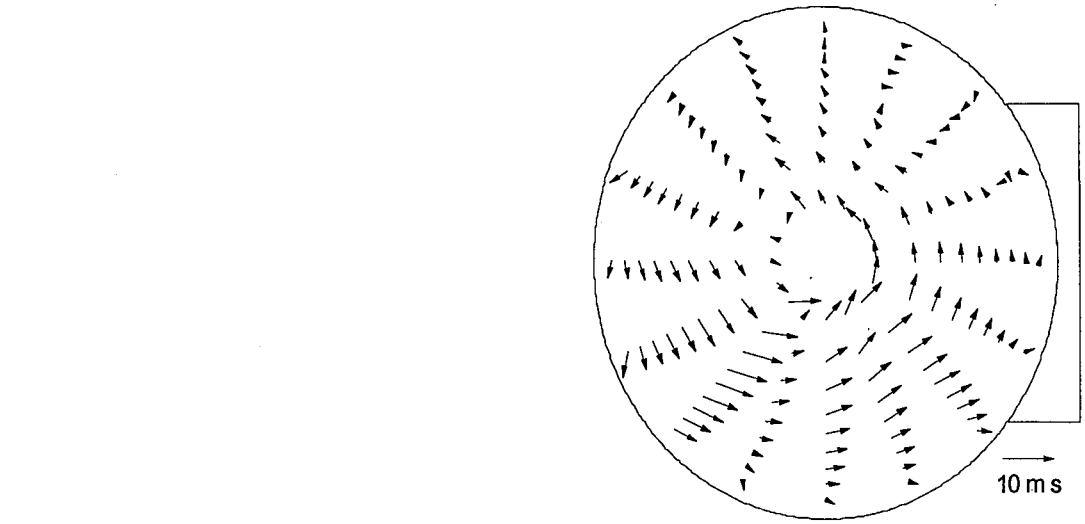

(c) Station C

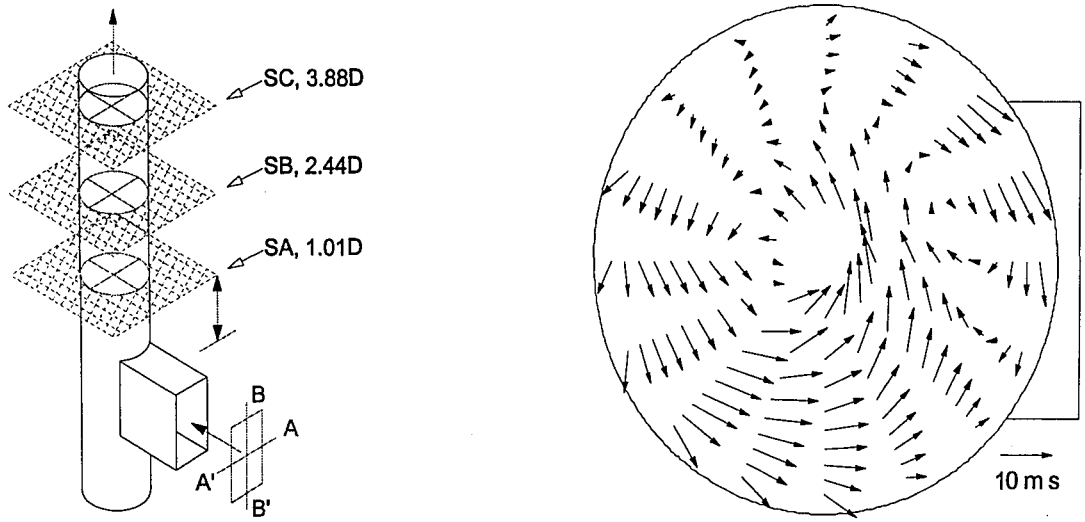

(b) Station B

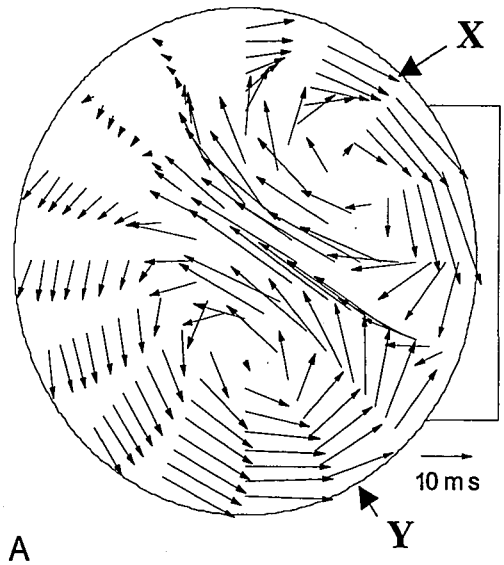

(a) Station A

Figure 4.5 Secondary Flow Pattern at Different Axial Locations

Decay of Swirl in the Stack

The Swirl number was calculated at the measurement locations to quantitatively evaluate the dissipation rate of the secondary flow. Swirling flows can be considered to be a combination of vortex and axial motion along the pipe axis. The axial and tangential components of velocity co-exist at any point in the flow field and the boundary layers near the wall are three-dimensional. Swirling flow is defined in CAA "40CFR Pt. 60 Appendix. A," as a flow with non-zero components of yaw and pitch.

The swirl number *S* is defined by the ratio of the angular momentum flux, M_{ang}, to the axial momentum flux, M_{axial}, at a given cross-section. For incompressible flow, it is given by:

$$S = \frac{M_{ang}}{R\,M_{axial}} = \frac{\int_0^R V_\theta\, V_Z\, r^2\, dr}{R\int_0^R V_Z^2\, r\, dr} \approx \frac{\sum_{i=1}^{N}\left|V_{\theta,i}\, V_{Z,i}\, r_i^2\right|}{R\sum_{i=1}^{N} V_{Z,i}\, r_i} \qquad (4.1)$$

where V_Z is the axial velocity, V_θ is the tangential velocity, and R is the duct radius. The reason for taking the absolute value of the angular momentum flux is that for the radial inlet, both positive and negative tangential velocity components are encountered in the vortex pair, which cancel the Swirl number where the vortices have similar strength. The absolute value of the angular momentum flux amounts to adding the contribution of both vortices into a single parameter.

The rate of decay of the swirling motion is dependent on Reynolds number and the roughness of the pipe wall [Yu and Kitoh, 1994]. Swirl angles and average resultant angles are presented in Table 4.1. Both quantities give an estimate of the strength of the secondary flow. In the model stack, both swirl and average resultant angle decay exponentially as a function of distance from the inlet (Figure 4.6). The general expression for swirl decay is given by

$$S \propto e^{\left(-\beta x/D\right)} \tag{4.2}$$

where the decay rate β is a function of the wall roughness [Reader-Harris, 1994].

Table 4.1 Swirl Number and Average Resultant Angle

Location	Swirl Number	Average RA
Station A	0.168797	18.13743°
Station B	0.099057	8.146332°
Station C	0.050381	4.643177°

With increasing swirl the position of maximum axial velocity moves progressively further away from the pipe centerline. For single vortex motion, at sufficiently high levels of swirl, a cylindrical region of reversed flow would be established about the pipe axis [Ward-Smith, 1980]. This explains the appearance of the higher axial velocity fluid in the outer rim, and of the low axial velocity core.

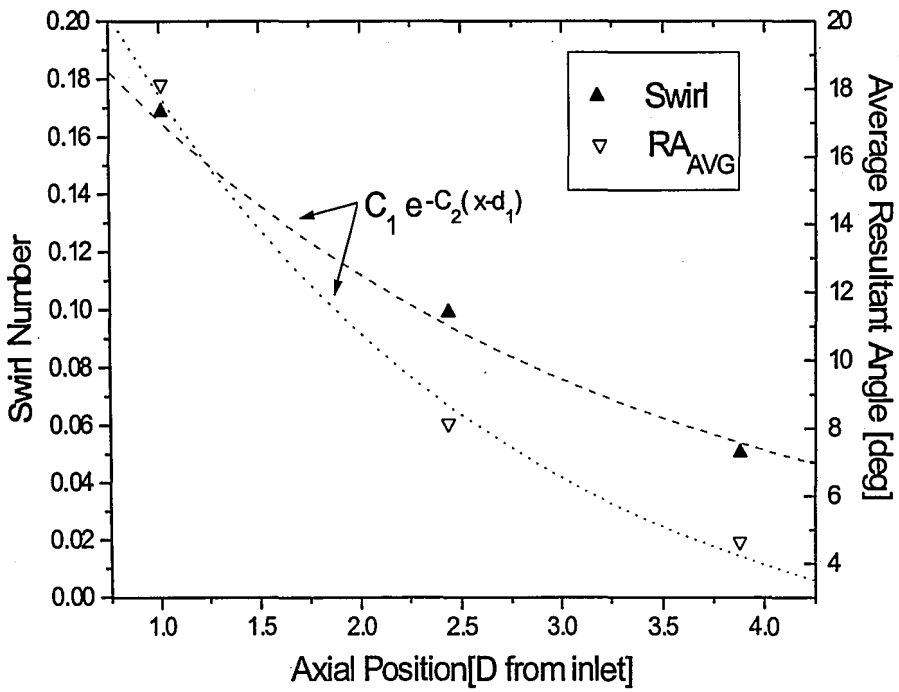

Figure 4.6 Swirl and RA at Different Axial Locatios

Chapter 5

Numerical Modeling

Introduction

The laboratory stack model with a radial inlet configuration was modeled using computational fluid dynamics. The objective of the simulations was to study the flow in the stack downstream from the radial inlet. The numerical predictions were generated at an average axial velocity in the stack of 30 m/s. A systematic grid convergence study was carried out to determine grid independent solutions.

The numerical simulations were performed with a commercial CFD package, CFX-Flow3D version 4.1c, developed by AEA Technology Engineering Software Inc. The computer platform was a HP700 workstation, running under the UNIX operating system (HP-UX 9.0), and 128 MB of RAM memory. The continuity and momentum equations along with an appropriate turbulence model (RNG k-ε) were solved in three dimensions. The code discretizes the governing equations using the control volume finite difference method, and solves the discretized equations using a variant of the SIMPLE (Semi-Implicit Pressure Linked Equations) algorithm.

Mathematical Modeling

Turbulent Gas Flow

High Reynolds number internal gas flows are complex time-dependent turbulent flows governed by the Navier-Stokes equations. CFX-Flow 3D solves a set of Reynolds-averaged Navier-Stokes (RANS) equations, along with closure equations for the Reynolds stresses. The program uses a generalized non-orthogonal body fitted coordinate system to discretize the governing equations. The governing equations are expressed in a non-orthogonal curvilinear coordinate system, referred to as computational space. This coordinate transformation makes it easy to implement boundary conditions on complex geometries.

Considering a steady state turbulent incompressible, isothermal flow with constant molecular viscosity and no body forces, the basic set of Reynolds-averaged equations for turbulent motion in a Cartesian coordinate system are expressed in tensor format. The continuity equation is given by

$$\frac{\partial U_j}{x_j} = 0 \tag{5.1}$$

and the momentum equations are given by

$$\rho \frac{\partial}{\partial x_j}\left(U_i\, U_j\right) = -\frac{\partial P}{\partial x_i} + \frac{\partial}{\partial x_j}\left(\mu \left[\frac{\partial U_i}{\partial x_j} + \frac{\partial U_j}{\partial x_i}\right] - \rho \overline{u_i\, u_j} \right) \tag{5.2}$$

where U_i (i= 1,2,3 correspond to x, y, z components respectively) are mean velocity components, P is the mean pressure, the $-\rho\overline{u_i u_j}$ terms are Reynolds stresses, ρ is the fluid density, and μ the molecular viscosity.

CFX-Flow3D (release 4.1c) offers two turbulence models based on the eddy viscosity hypothesis, i.e. the standard k-ε and the renormalization group based RNG k-ε turbulence models [Yakhot and Orzag, 1986]. Introducing a turbulent viscosity, μ_t, the Reynolds stresses can be expressed as

$$-\rho\overline{u_i u_j}+\frac{2}{3}\rho k\delta_{ij}=\mu_t\left(\frac{\partial U_i}{\partial x_j}+\frac{\partial U_j}{\partial x_i}\right) \tag{5.3}$$

where $k=\frac{1}{2}\overline{u_i u_i}$ denotes the turbulent kinetic energy and δ_{ij} is the Kronecker-delta tensor, the eddy viscosity μ_t, is prescribed by the turbulence model. Ignoring $\frac{\partial U_j}{\partial U_i}$, equation (5.2) becomes

$$\rho\frac{\partial}{\partial x_j}\left(U_i U_j\right)=-\frac{\partial}{\partial x_i}\left(P+\frac{2}{3}\rho k\right)+\frac{\partial}{\partial x_j}\left(\left(\mu+\mu_t\right)\frac{\partial U_i}{\partial x_j}\right) \tag{5.4}$$

The standard k-ε turbulence model [Jones, Launder, 1972] appears to be inadequate for predicting complex turbulent shear layers, such as in flows subjected to curvature [Wilcox, 1994]. The RNG k-ε turbulence model [Yakhot and Orzag, 1986] has shown better performance over the standard k-ε model in

predicting the streamwise, radial velocity components and Reynolds shear stresses of a turbulent flow through 90° circular pipe bend [Yin et al, 1996, Yilmaz, 1997]. The radial inlet develops similar flow conditions to the 90° pipe bend. Therefore the RNG *k*-ε model was used in our study to predict turbulent quantities within the flow field.

The RNG *k*-ε model is derived from a renormalization group analysis of the Navier-Stokes equations. In addition to using a different set of model constants, the RNG *k*-ε model differs from the standard *k*-ε model through a modification to the equation for ε. The RNG *k*-ε model, assumes that

$$\mu_t = C_\mu \rho \frac{k^2}{\varepsilon} \tag{5.5}$$

where the constant C_μ is equal to 0.085.

The transport equations for the turbulence kinetic energy *k* and turbulence dissipation rate ε are:

$$\rho \frac{\partial}{\partial x_i}(U_i\, k) = \frac{\partial}{\partial x_i}\left(\left(\mu + \frac{\mu_t}{\sigma_k}\right)\frac{\partial k}{\partial x_i}\right) + P - \rho\varepsilon \tag{5.6}$$

and

$$\rho \frac{\partial}{\partial x_i}(U_i\, \varepsilon) = \frac{\partial}{\partial x_i}\left(\left(\mu + \frac{\mu_t}{\sigma_\varepsilon}\right)\frac{\partial \varepsilon}{\partial x_i}\right) + C_1 \frac{\varepsilon}{k} P - C_1 \rho \frac{\varepsilon^2}{k} \tag{5.7}$$

where P is the shear production defined by

$$P = \mu_t \left(\frac{\partial U_i}{\partial x_j} + \frac{\partial U_j}{\partial x_i} \right) \frac{\partial U_i}{\partial x_j} \tag{5.8}$$

The model parameters σ_k, σ_ε, and C_2 have constant numerical values of 0.7179, 0.7179, and 1.68 respectively. The model parameter C1 is given by

$$C_1 = 1.42 - \frac{\eta \left(1 - \frac{\eta}{\eta_0} \right)}{\left(1 + \beta \eta^3 \right)} \tag{5.9}$$

and

$$\eta = \left(\frac{P}{\mu_t} \right)^{1/2} \frac{k}{\varepsilon} \tag{5.10}$$

Here η_0 and β are additional model constants whose numerical values are 4.38 and 0.0015, respectively.

Wall Boundary Conditions

Two-equation turbulence models such as the RNG k-ε model cannot be extended to the viscosity dominated sublayer of the turbulent boundary layer. Applying the no-slip boundary condition and integrating through the viscous sublayer yields unsatisfactory results [Wilcox, 1994]. Therefore CFX-Flow3D implements a synthetic boundary condition to extend the k-ε model up to the wall.

The wall function concept assumes that, at a nodal point adjacent to the wall (with a wall distance of y_p) just outside the viscous sublayer, the velocity component parallel to the wall follows the logarithmic law of the wall. It can be shown that the shear stress for node *p* is given by

$$\tau_p = \tau_w = \rho C_\mu^{1/2} k \tag{5.11}$$

where the subscript *p* indicates values at grid nodes *p*, while subscript *w* represents the wall. It is assumed that the logarithmic velocity profile prevails in the region between the wall and the node *p* adjacent to the wall. Using nondimensional distance $y^+ = \frac{(\rho\tau_w)^{1/2}}{\mu} y$ and nondimensional velocity $u^+ = U_p/(\tau_w/\rho)^{1/2}$, the law of the wall is given by

$$y_0^+ = \begin{cases} y^+, & \text{for } y^+ < y_0^+ \\ \frac{1}{\kappa}\ln(E y^+), & \text{for } y^+ > y_0^+ \end{cases} \tag{5.12}$$

The crossover point y_0^+ between the viscous sublayer and the logarithmic region is the upper positive root of

$$y_0^+ = \frac{1}{\kappa}\ln(E y_0^+) \tag{5.13}$$

Governing Equations

The flow solution is obtained with a set of six partial differential equations, which can be written in generic transport form [Yilmaz 1997]:

$$\frac{\partial}{\partial x_i}(\rho U_i \phi) = \frac{\partial}{\partial x_i}\left(\Gamma_\phi \frac{\partial \phi}{\partial x_i} \right) + S_\phi \qquad (5.14)$$

where the terms U_i are mean velocity components (U,V,W). The parameter ϕ represents the variables (U,V,W,k,ε). The quantity Γ_ϕ is the effective viscosity. The terms S_ϕ are source terms. Table 5.1 lists the values of ϕ for each equation, with the respective coefficients and source terms.

Table 5.1 Definition of Variables, Coefficients and Source Terms

Equation	ϕ	Γ_ϕ	S_ϕ
Continuity	1	0	0
Momentum	U_I	$\mu+\mu_t$	$-\frac{\partial}{\partial x_i}\left(p+\frac{2}{3}\rho k\right)$
Turbulent kinetic energy	k	$\mu+\frac{\mu_t}{\sigma_k}$	$P-\rho\varepsilon$
Turbulence dissipation	ε	$\mu+\frac{\mu_t}{\sigma_\varepsilon}$	$(\varepsilon/k)(C_1P-C_2\rho\varepsilon)$

Boundary Conditions

The transport equations presented in the preceding section are elliptic in space coordinates and hence require that values or gradients of transported variables be defined all around the flow geometry. A uniform velocity profile was assumed at the inlet to the horizontal section. Mean flow values for *V*, *k* and ε were specified at this point. Uniform profiles for the turbulence quantities k and ε were approximated using the following relations

$$k_{inlet} = 0.002 \cdot u_{inlet}^2 \tag{5.15}$$

and

$$\varepsilon_{inlet} = \frac{k_{inlet}^{3/2}}{0.3 D_h} \tag{5.16}$$

Equation (5.15) assumes that the kinetic energy at the inlet is equal to 10% of the mean flow kinetic energy.

At the outlet, Neumann boundary conditions were imposed on all transport variables so that

$$\frac{\partial(..)}{\partial z} = 0 \tag{5.17}$$

except the axial velocity which was given a constant normal gradient. The value of that constant is internally determined by CFX-Flow3D so that the total flow rate out of the domain remains equal to the total flow into the domain at all stages of the solution. This constant tends to zero as the flow approximates fully developed flow. Finally the no-slip condition was specified at the model wall surfaces.

Numerical Solution

CFX-Flow3D uses the finite volume approach to obtain numerical solutions at discrete points of a grid that encompasses a sequence of elemental control volumes. The computational mesh generated by the code is characterized as boundary fitted multi-block, structured grids, and non-staggered, i.e. the grid is constructed over the geometry by gluing an arbitrary number of topologically rectangular grids, or blocks. CFX-Flow3D uses the Rhie-Chow algorithm [Rhie 1981; Rhie, Chow, 1983] that allows for the implementation of the SIMPLE based algorithms [Patankar, Spalding, 1972; Patankar, 1980] on non staggered grids, while avoiding the problem of checker-board oscillations in pressure and velocity.

Highly distorted cells close to the wall region would create instabilities when using k-ε based turbulence models. Therefore the flow domain was discretized in such a way as to distribute the grids as orthogonally as possible. Using a combination of 5 blocks for the pipe cross section provided grids which were near orthogonal close to the wall region and orthogonal in the pipe center (Figure 5.1 a). The radial inlet geometry was divided into a rectangular duct section with a length of 10 hydraulic diameters (2 blocks), the radial inlet section where the flow turns (15 blocks) (Figure 5.1 b), and a circular duct section with a length of 20 diameters (5 blocks).

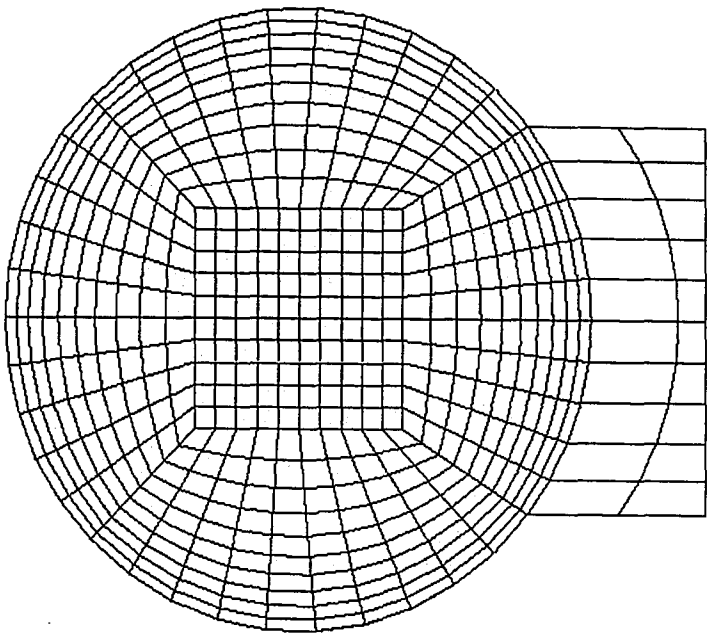

(a)

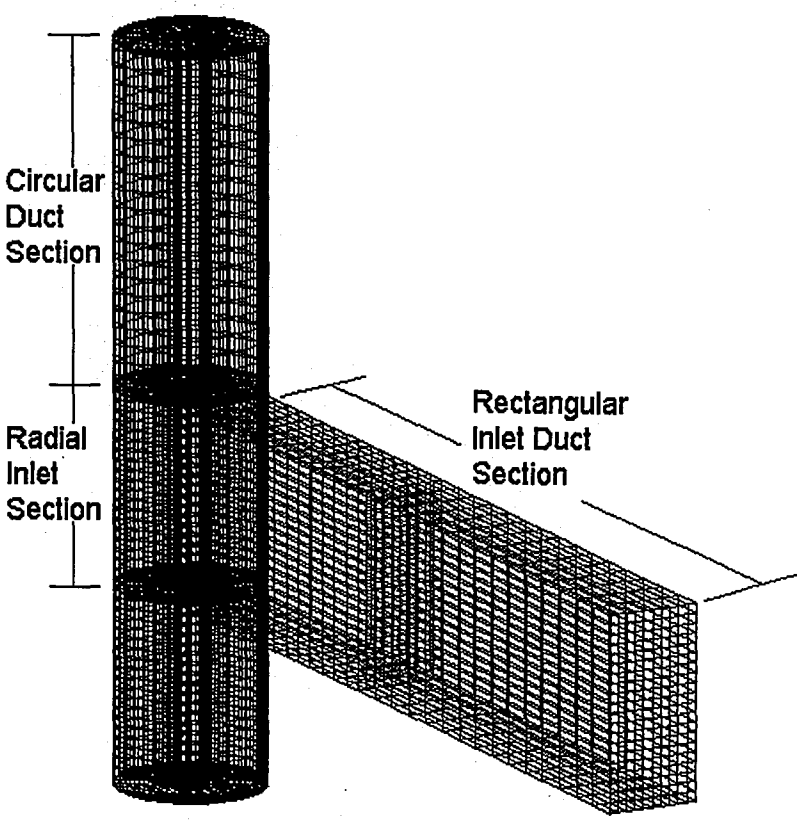

(b)

Figure 5.1 Detail of Computational Working Grid: (a) Stack Cross-Section, (b) Stack inlet

Due to the use of boundary fitted grids, the discretization procedure requires that the governing equations be converted from the Cartesian coordinate system adopted in the physical domain to the curvilinear coordinate system used in the rectangular computational domain [Thompson et al., 1985]. The transformed governing equations are integrated over the unit cube control volumes in computational space to obtain a discrete equation which connects the variables at the centers of the control volumes with their neighbors. All terms in all the equations except convection terms are discretized in space using second-order centered differencing. A third-order accurate QUICK algorithm was used for the convection terms. To handle the non-linearity of the equations the treatment of all transported variables involved two nested levels of iterations referred to as inner and outer iterations. Pressure was handled by a special procedure, the velocity-pressure coupling algorithm [Yilmaz, 1997].

Outer iterations were repeated until the problem satisfied a convergence criterion. For the simulations performed in this study, the convergence of outer iteration was judged by the accuracy in the continuity equation when evaluated by the current values of the dependent variables. The solution procedure was considered converged when the ratio of the summation of absolute mass source residuals to the total rate of mass inflow fell below a prescribed tolerance.

$$\frac{\sum_{i=1}^{N_{cell}} |R_{M,i}|}{\dot{m}_{air}} \leq \delta \qquad (5.18)$$

For the simulations performed in this study, the prescribed tolerance δ was equal to 1×10^{-5}.

Solving the momentum equations requires previous knowledge of the pressure gradient. The constraint that uniquely determines the pressure field is the continuity equation. The treatment of pressure involved using simplified versions of the discrete momentum equations to link pressure correction to velocity-component correction, and then substituting into the continuity equation. A linear solver subsequently updated both the pressure and velocity fields. CFX-Flow3D offers a pressure correction procedure based on the standard SIMPLE algorithm [Patankar, 1980].

Grid Refinement Study

Once an appropriate block structure was determined, the influences of grid refinement and boundary position were evaluated to obtain grid converged solutions. To verify the numerical model, several simulations were performed on the radial inlet geometry with different orders of discretization. A comparison of the velocity profiles from different simulations was made at 3.88 diameters from the inlet, Station C

By cutting the stack length in half (Figure 5.2) (Working Grid half-length simulation), and comparing results to those of the full-length stack (Working Grid full-length simulation) it was found that the position of the outlet boundary did not affect the solution. Figure 5.3 a, shows the comparison of the N-S axial velocity profile 3.88 diameters from the inlet (Station C).

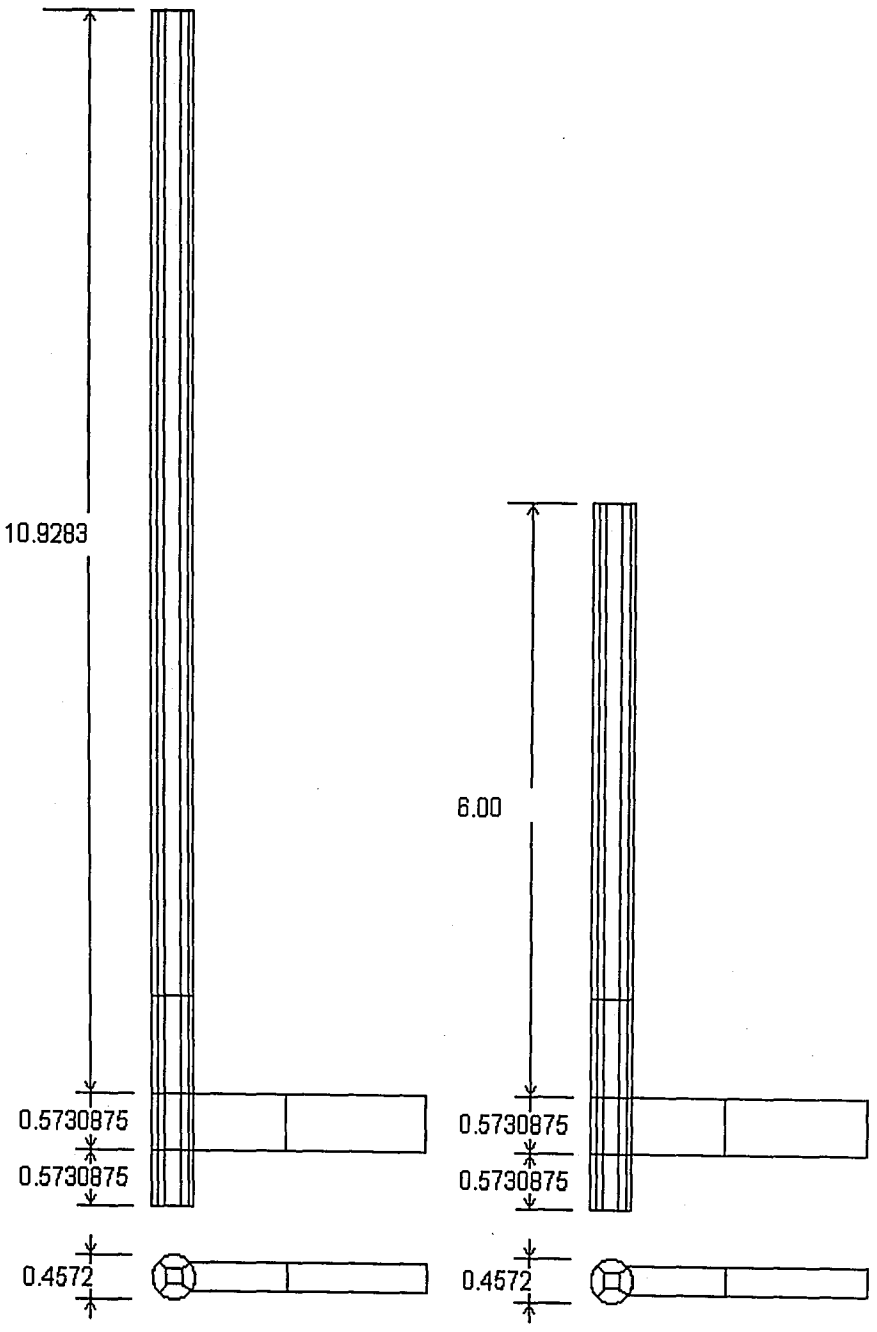

Figure 5.2 Full-Length and Half-Length Stack Models

Grid refinement was carried out in axial, radial and tangential directions. For a given geometry if the solutions of the "Working Grid (WG)" and a (refined) "Fine grid (FG)" are essentially the same, then the WG solution is considered to be grid independent. To make the best use of the available computer resources, grid refinement was done with the half-length stack geometry, the "WG" half-length model had 70,000 nodes, and the "Fine grid" half-length model had an equivalent of 240,000 nodes. Results for the axial velocity profiles of the traverse @ 90° 3.88 diameters from the inlet are shown in Figure 5.3 b. The "Working Grid" model was used for all subsequent CFD calculations. Information on the different cases solved with CFX-Flow3D is listed in Table 5.2.

Table 5.2 Grid Discretization for CFD Simulations

Case	Blocks	Cells CS	Cells	Nodes	Int. Nodes
WG full-length	22	500	70312	70312	43668
WG half-Length	22	500	94512	94512	59868
FG half length Symmetry plane	18	850	119583	119583	83447
FG Unbalanced inlet flow.	48	624	111360	143316	84020

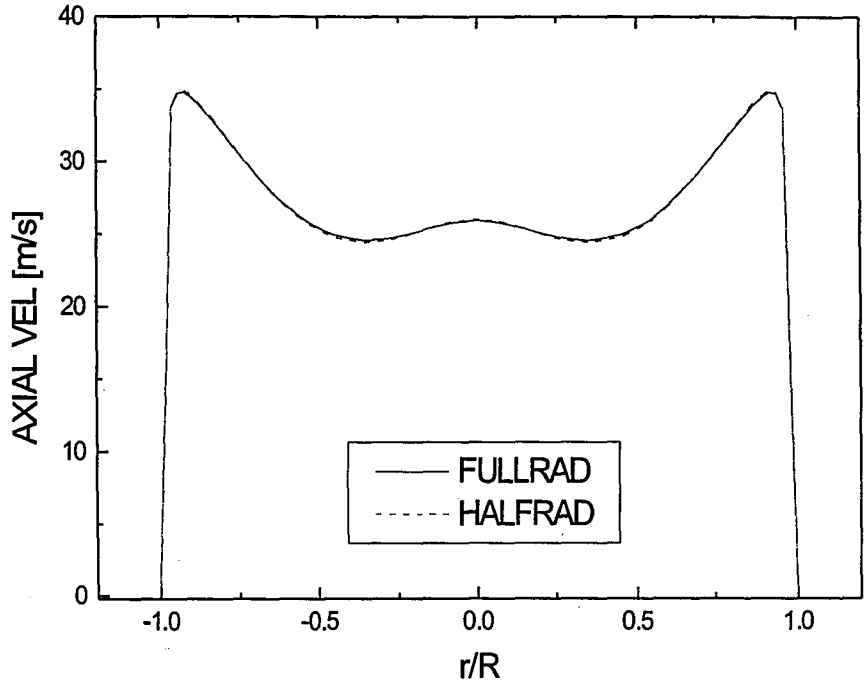

(a)

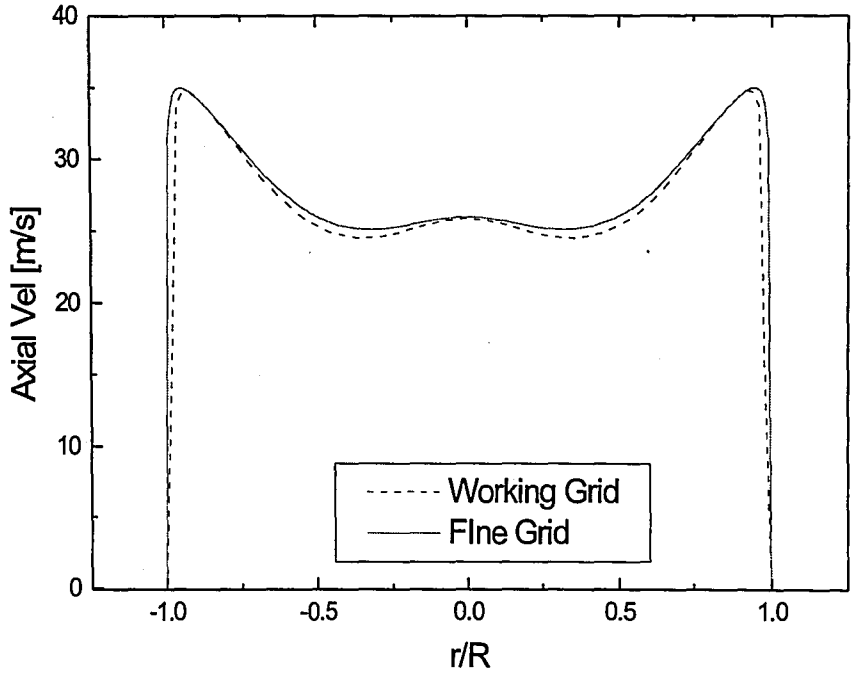

(b)

Figure 5.3 Axial Velocity profiles, Station C, N-S traverse; (a) Comparison of WG and FG Half-Length, (b) Comparison of WG Full-Length and WG Half-Length

Results

Once an appropriate model was established, simulations were carried out to determine the flow resulting from a uniform inlet stream. The effect of a asymmetric inlet velocity profile was also studied by running simulations with an unbalanced inlet flow. Data were compared in two perpendicular axes passing through the stack centerline (Figure 5.4), the E-W axis (parallel to the inlet duct centerline), and the N-S axis (normal to the inlet duct centerline).

As the inlet flow turns into the stack it follows the bend described by the radius joining the inlet duct centerline to the stack axis. Flow separation from the corner of the interior wall results in an eddy zone that propagates far ahead and across the stack. The velocity distribution in the stack at this point is extremely non-uniform with high velocities on the wall opposite the inlet. These velocities result from the acceleration of the flow outside the re-circulation region, as it must flow over the widest part of the separation. Consequently, there is an increased velocity gradient and a high shear stress in the near wall.

Secondary flows are generated in cross-stream planes in the stack downstream of the inlet due to the appearance of inertia forces. The counter-rotating motion of these flows is influenced by the separation of the flow at the sides of the inlet breaching, generating cross-stream plane circulation.

The computational fluid dynamics simulations show that for a uniform inlet stream the numerical results are mirrored on both sides of the model symmetry plane. The secondary flow pattern at Station C shows two counter-rotating vortex structures (Figure 5.5 a). This flow pattern loses strength as it convects along the stack axial direction. The computed vortex structures maintain a stable interface along the whole length of the stack without interacting. The interface remains aligned with the symmetry plane, i.e. the E-W direction. Fluid pressed against the stack wall by the action of centrifugal forces creates a high axial velocity fluid region in close proximity to the stack wall (Figure 5.5 b). Centrifugal forces also establish a transverse pressure gradient with low pressure in the center of each vortex cell and high pressure at the wall. From the simulations it is clear that the axial velocity distribution in planes close to the inlet region is heavily influenced by the secondary flow pattern existing within the flow field.

In the simulation, average resultant angle decays in an exponential manner (Figure 5.6). Its rate of decay is dependent on the turbulence model and on the dissipation function of the scheme employed to discretize the convective terms of the momentum equations. The rate of decay of the experimental data seems to agree with the rate of decay in the numerical simulation, although the secondary flow pattern is not the same at the downstream locations.

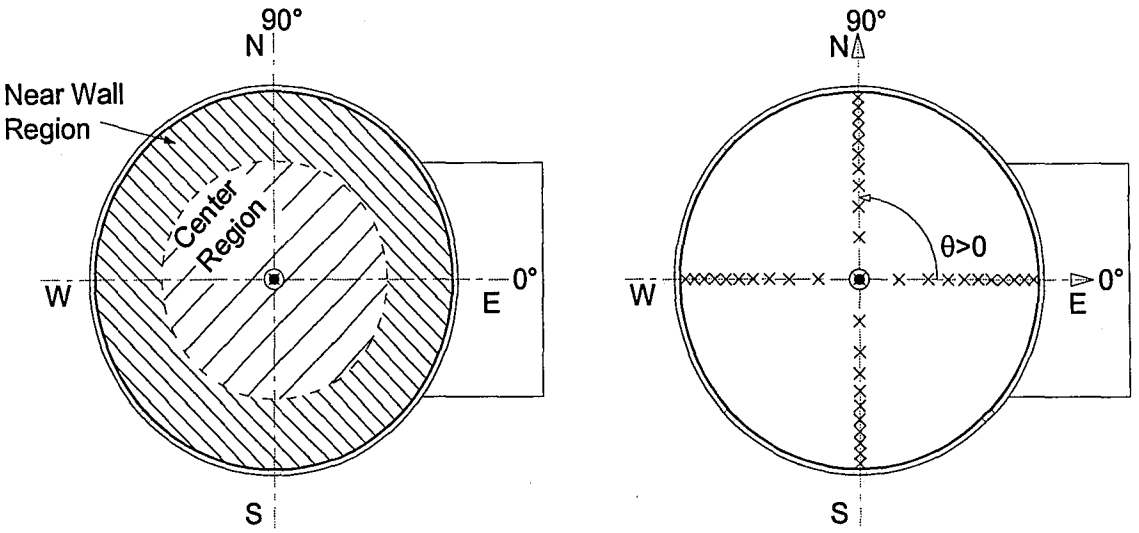

Figure 5.4 Traverse location at 0° and 90°, Rectangular Inlet Duct Symmetry Axes

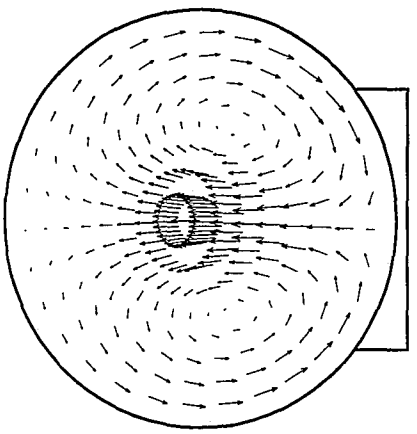

(a) Station C

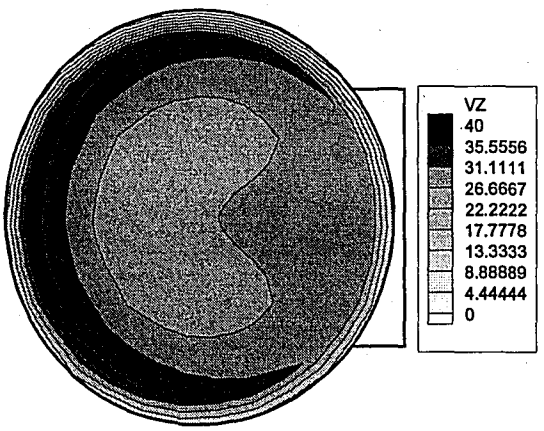

(b) Station C

Figure 5.5 (a) Secondary Flow Pattern, and (b) Axial Velocity Distribution at Station C, Uniform Inlet Profile, WG Half-Length Model

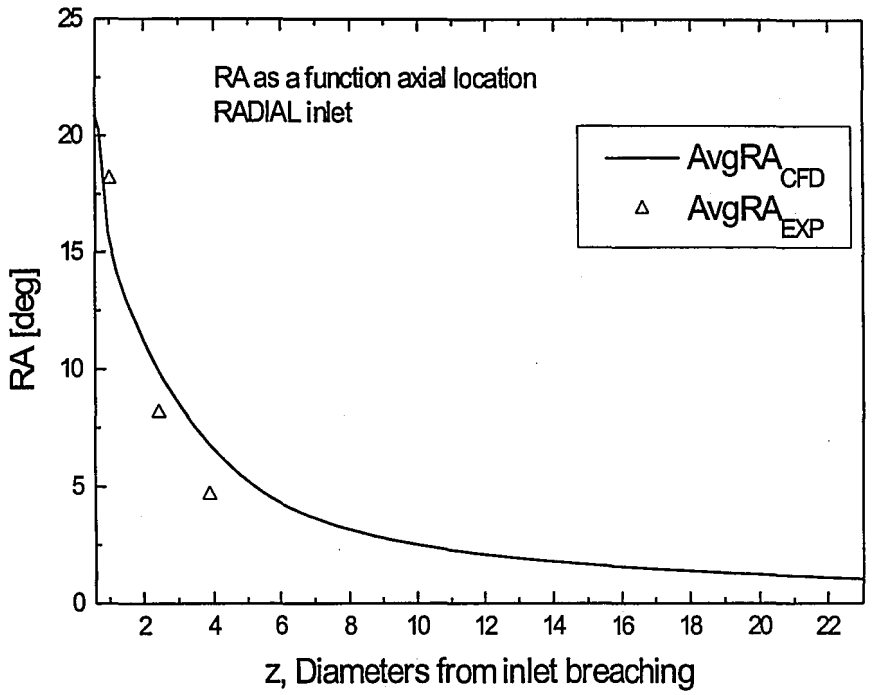

Figure 5.6 Average Resultant Angle as a function of Axial Position.

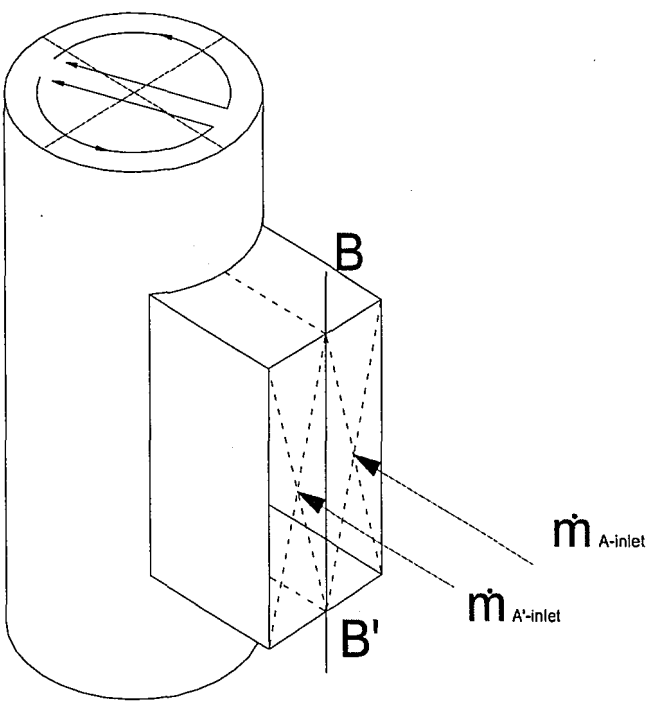

Figure 5.7 Flow Rate Unbalancing

The asymmetric inlet flow was generated by dividing the inlet block geometry on the B-B' plane, and inputting different flow rates on each side (Figure 5.7). The degree of imbalance was determined by computing the approximate mass flow on each side of the inlet using experimental velocity measurements taken at the model stack. The imbalance was determined to be around 5%, the flow rate is calculated from

$$\dot{m}_{A'-inlet} \Big/ \dot{m}_{A-inlet} \approx 0.95 \tag{5.19}$$

and

$$\dot{m}_{A'-inlet} + \dot{m}_{A-inlet} = \dot{m} \tag{5.20}$$

where $\dot{m}$ is the stack flow rate. Results from this simulation show that the strength of the individual vortex structures depends on the shape of the inlet velocity profile, particularly the flow rate imbalance about the B-B' axis. The stronger vortex corresponds to the inlet side with higher flow rate, the alignment of the interface follows accordingly (Figure 5.7).

Axial velocity distribution for the unbalanced case at the equivalent measurement stations is presented in Figure 5.8. The concentration of higher axial velocity fluid in the wall opposite the inlet is present in all three locations. Secondary flow pattern for the unbalanced flow simulation is presented in Figure 5.9. The secondary flow interface has rotated approximately 5° clockwise from the inlet duct centerline. In the simulation the vortex structures remain unaligned for the length of the stack. Again, the vortex pair does not interact with itself.

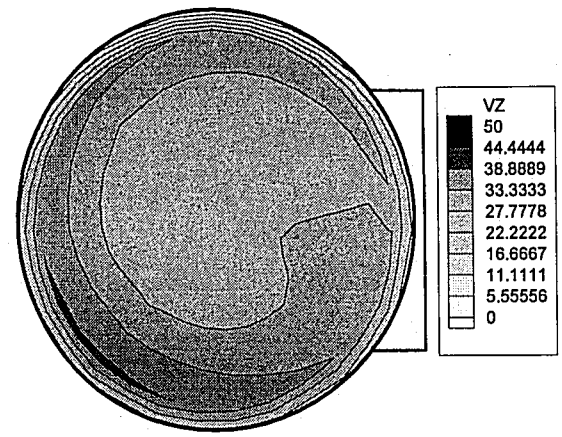

(c) Station C

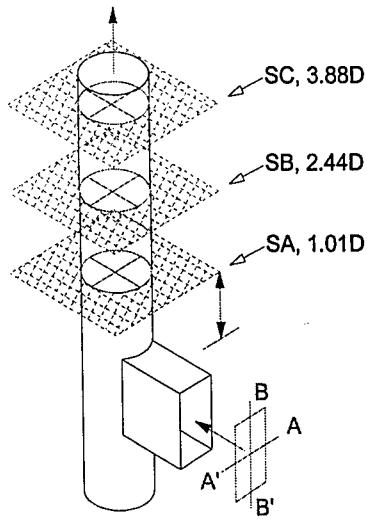

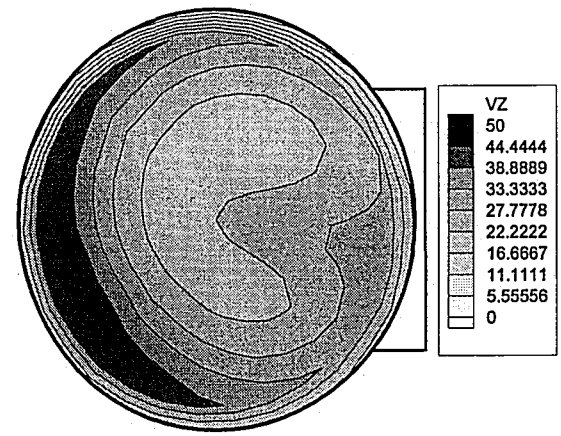

(b) Station B

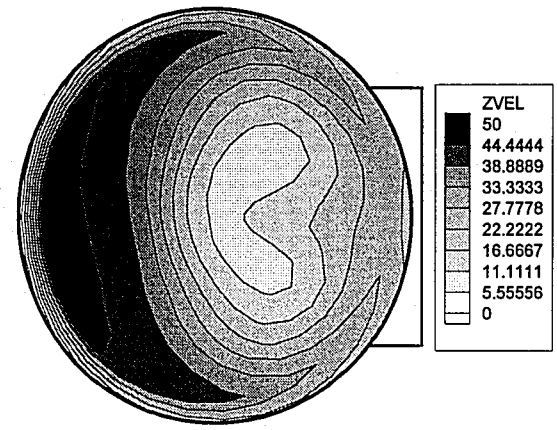

(a) Station A

Figure 5.8 Axial Velocity Distribution at Different Axial Locations, Unbalanced Inlet Model, WG Half-Length Model

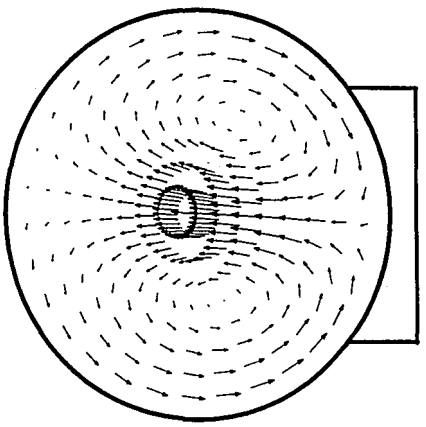

(c) Station C

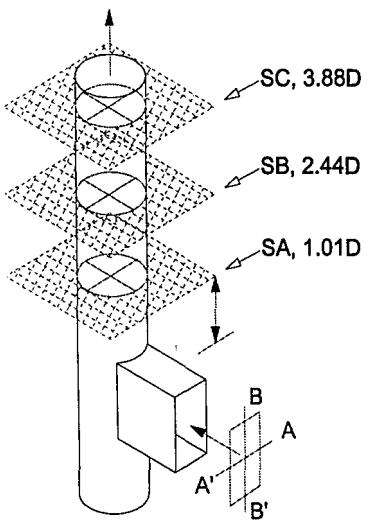

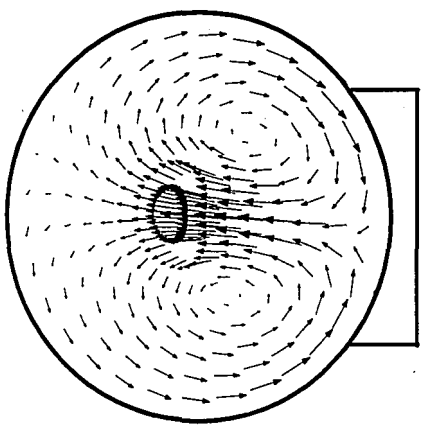

(b) Station B

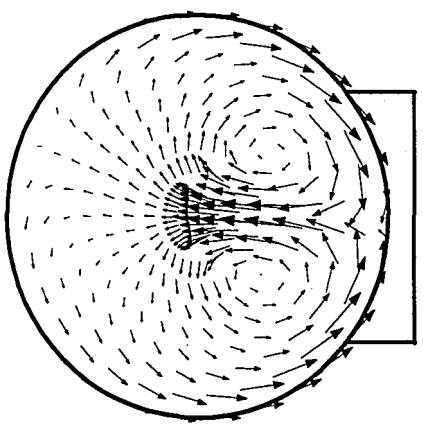

(a) Station A

Figure 5.9 Secondary Flow Pattern at Different Axial Locations, Unbalanced Inlet Model, WG Half-Length Model

Comparison with Experimental Data

Experimental results presented in the previous chapter tell us that the paired vortices evolve into a single vortical structure by Station C. Therefore, reasonable agreement between the numerical results and the experiment was not found at axial locations other than Station A. Comparison of experimental velocity data at Station A shows that the axial velocity profiles in the N-S traverse (Figure 5.10 a), and the E-W traverse (Figure 5.10 b) are in good agreement with the unbalanced numerical simulation. Comparison of data at Stations B (Figure 5.11 a and b) and at Station C (Figure 5.12 a and b) shows increasing disagreement in the downstream direction.

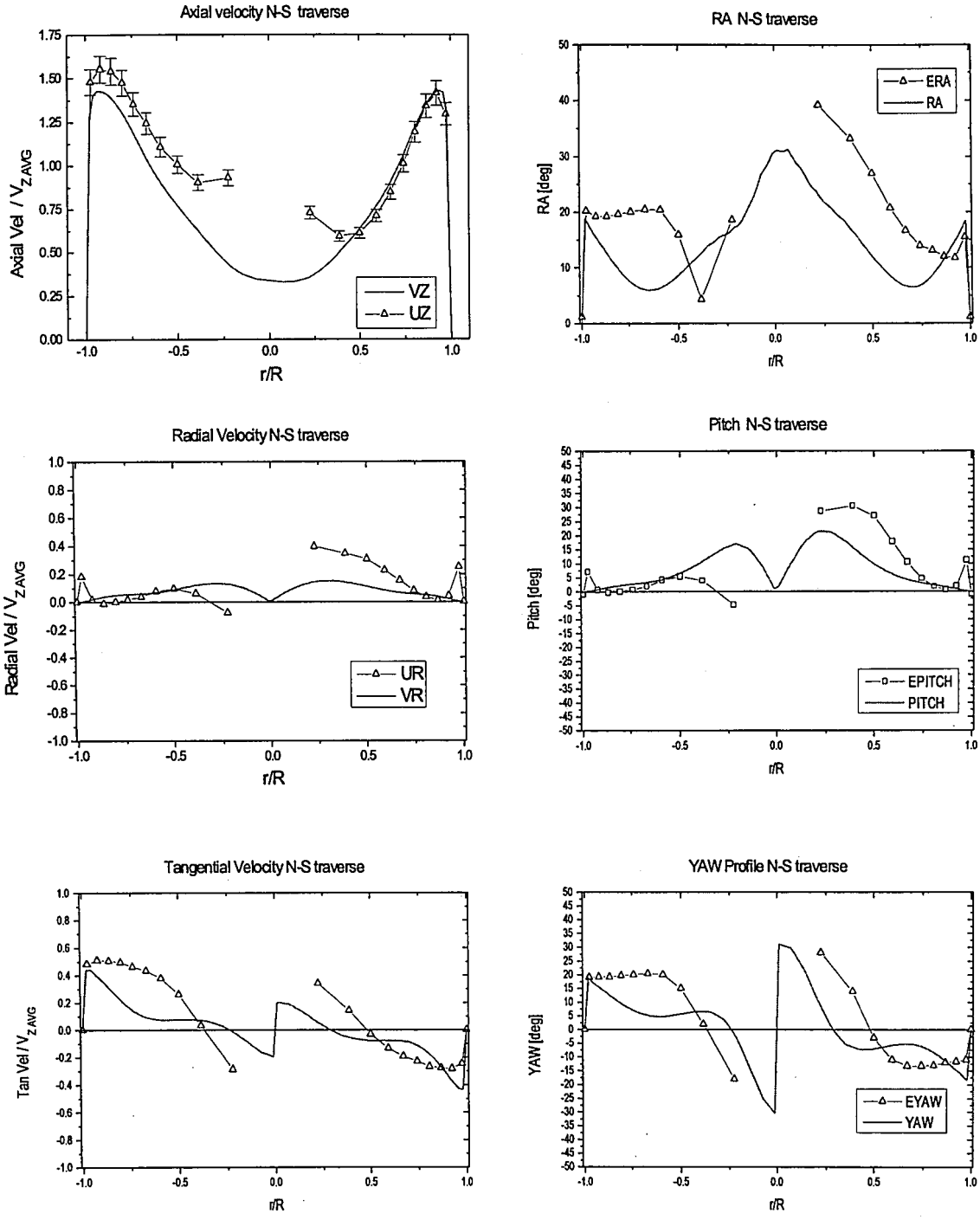

Figure 5.10 (a) Comparison of Experimental Data and Numerical Simulation of N-S Traverse at Station A, Unbalanced Inlet Model, WG Half-Length Model.

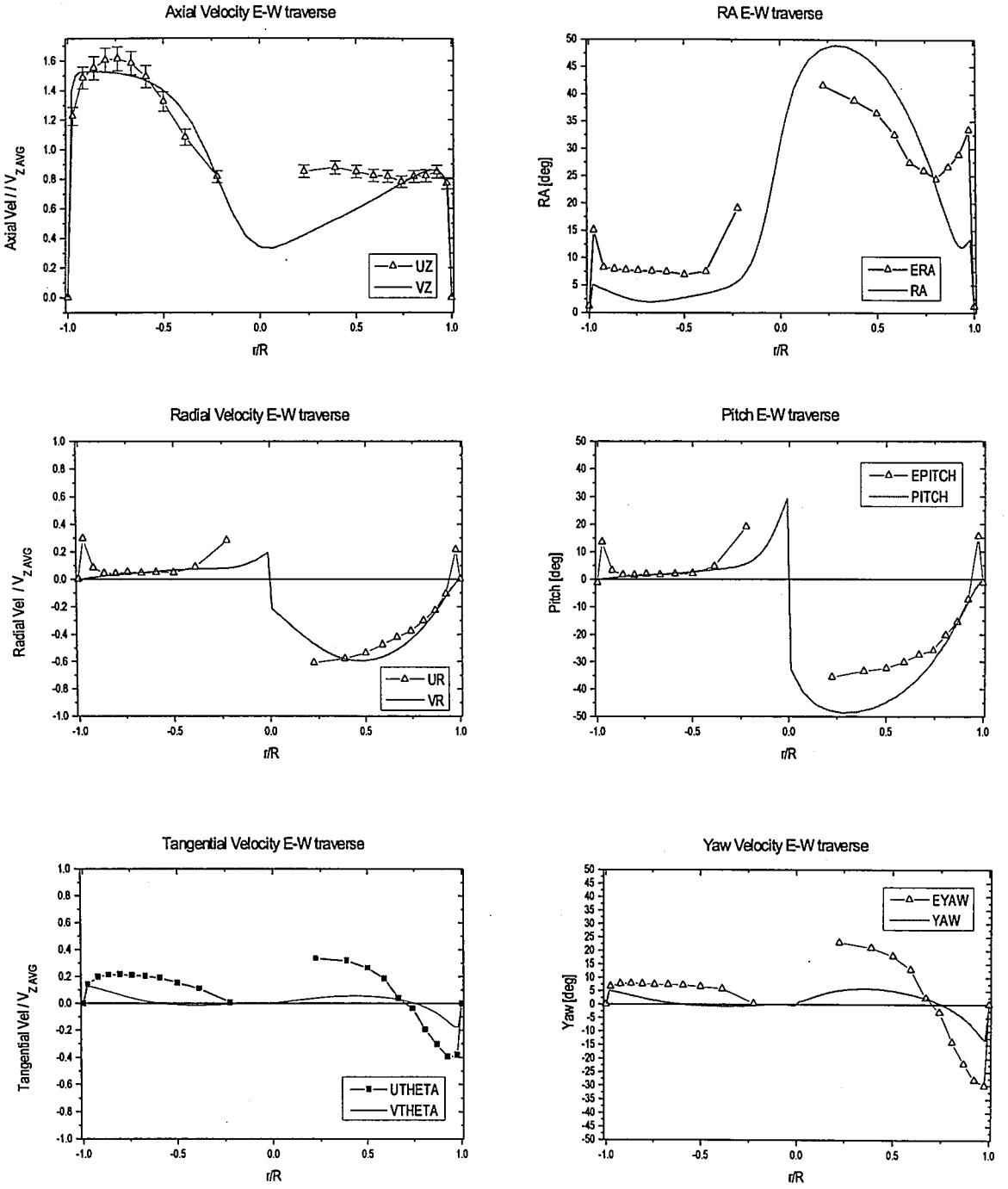

Figure 5.10 (b) Comparison of Experimental Data and Numerical Simulation of E-W Traverse at Station A, Unbalanced Inlet Model, WG Half-Length Model

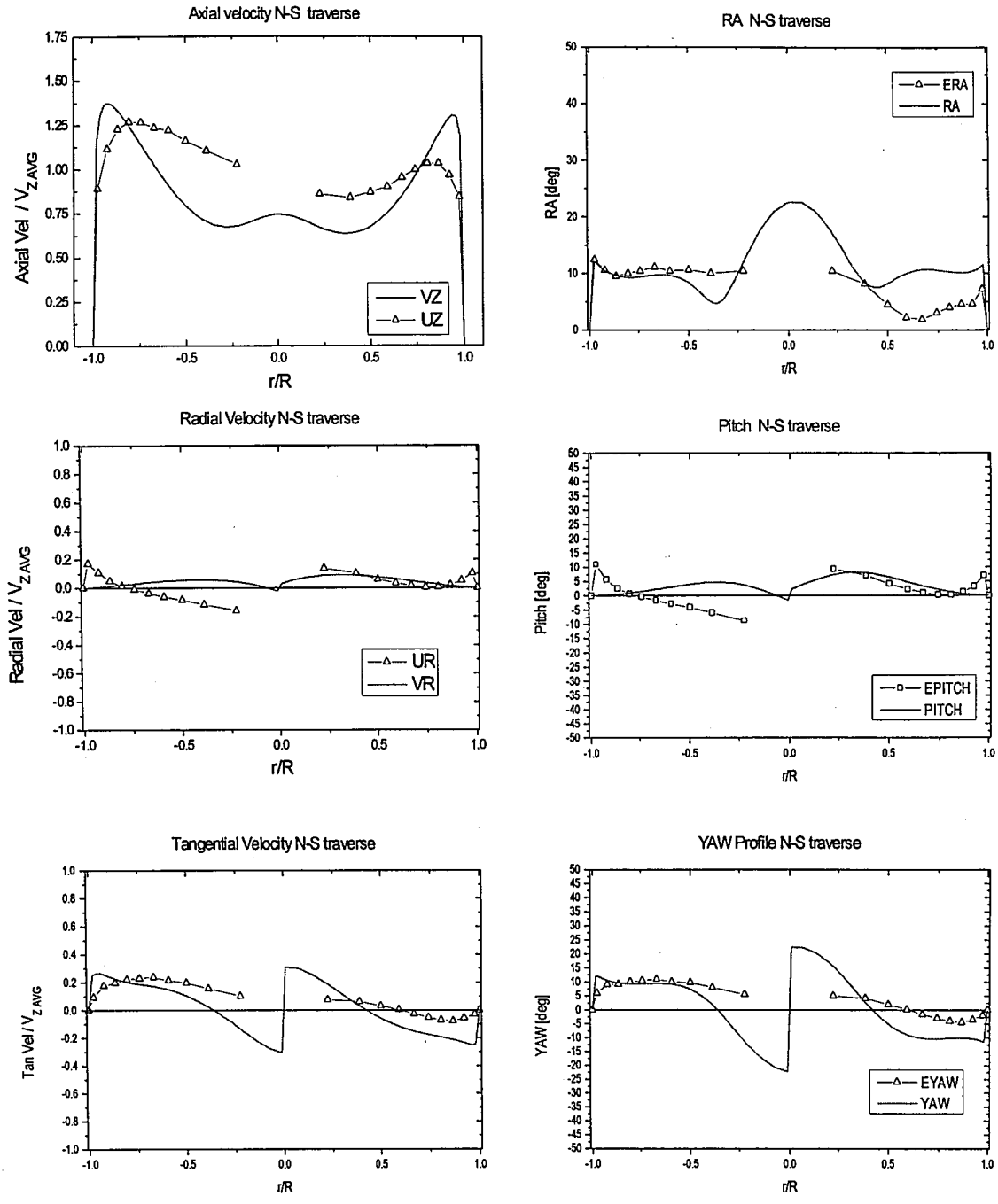

Figure 5.11 (a) Comparison of Experimental Data and Numerical Simulation of N-S Traverse at Station B, Unbalanced Inlet Model, WG Half-Length Model

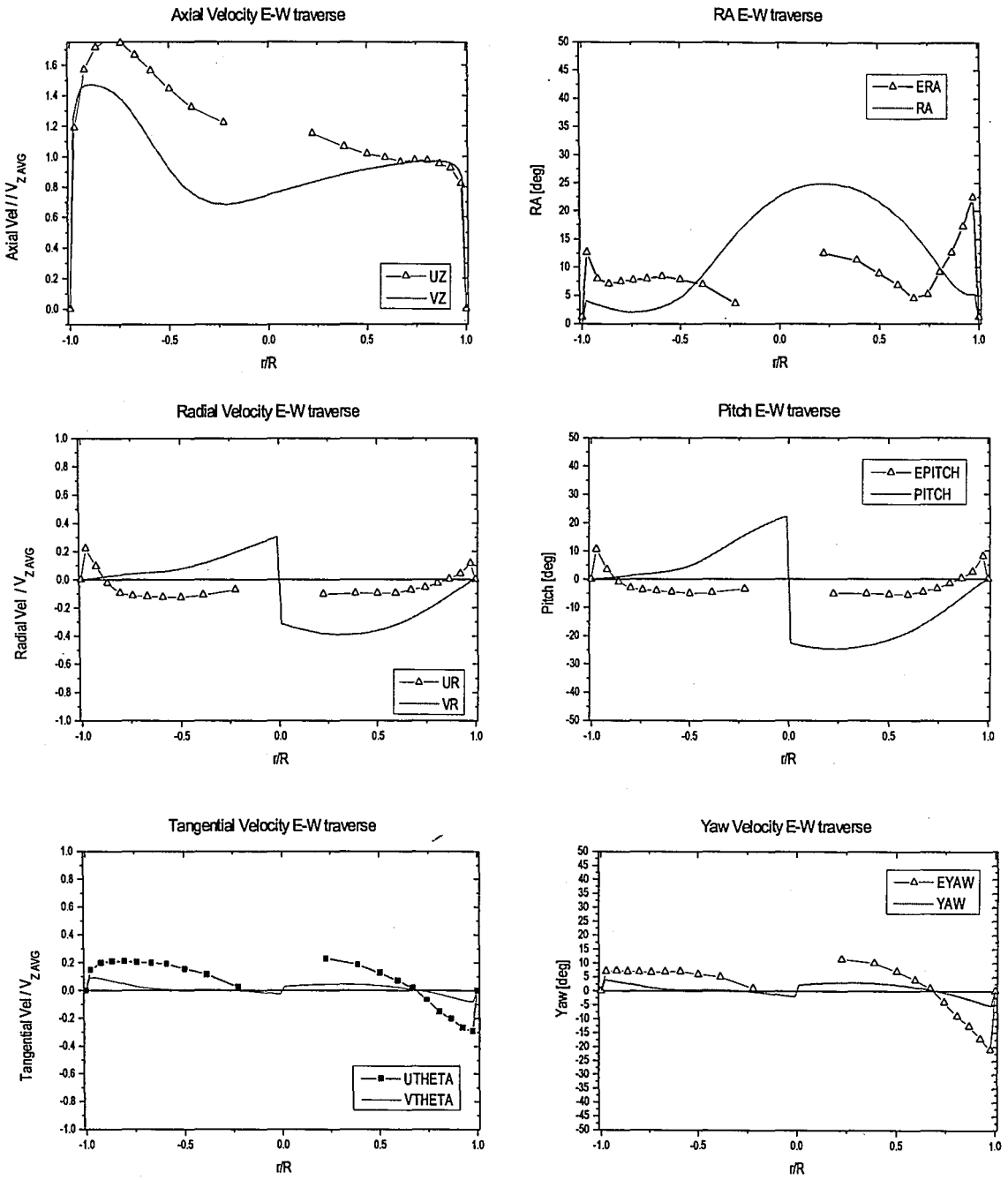

Figure 5.11 (b) Comparison of Experimental Data and Numerical Simulation of E-W Traverse at Station B, Unbalanced Inlet Model, WG Half-Length Model

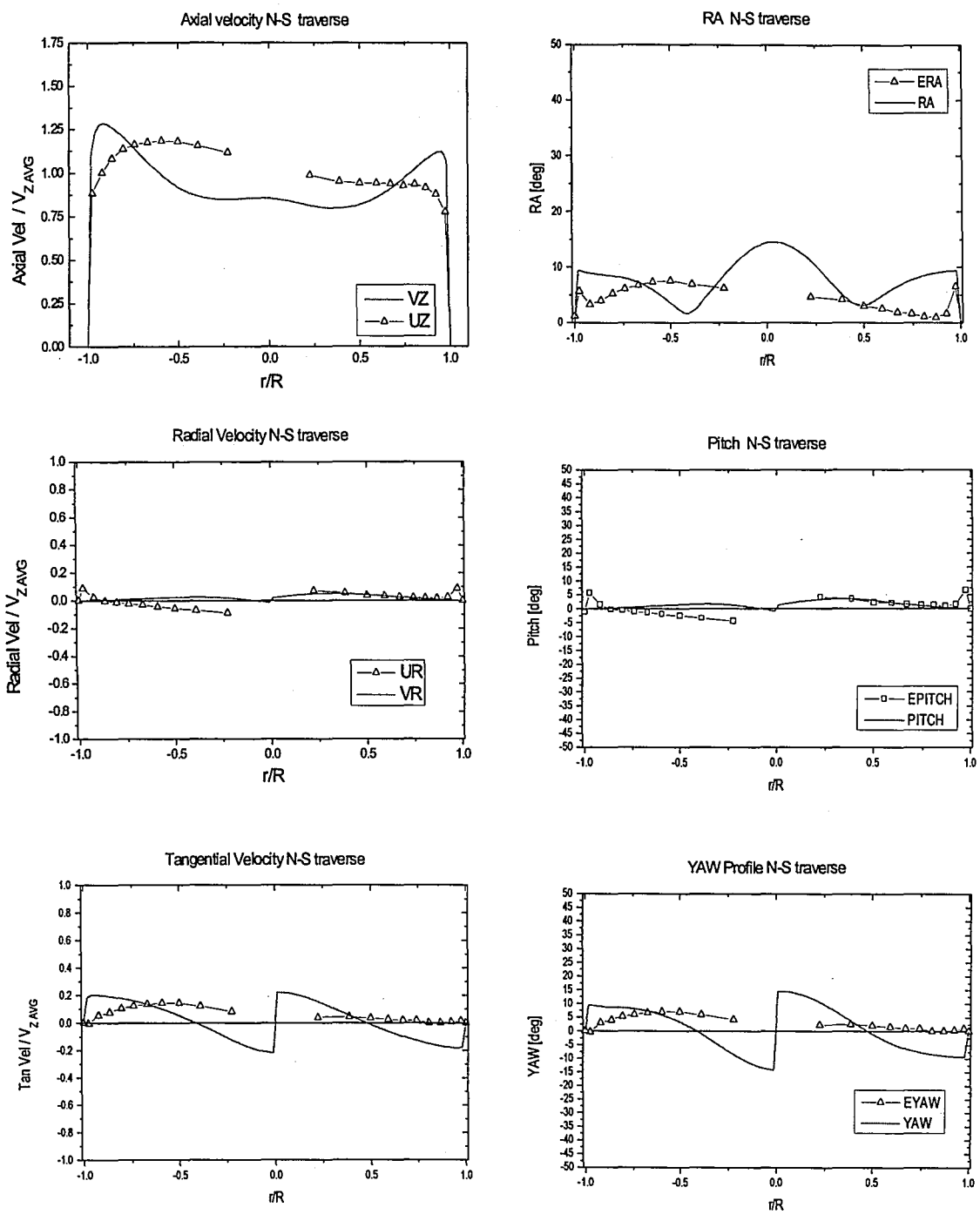

Figure 5.12 (a) Comparison of Experimental Data and Numerical Simulation of N-S Traverse at Station C, Unbalanced Inlet Model, WG Half-Length Model

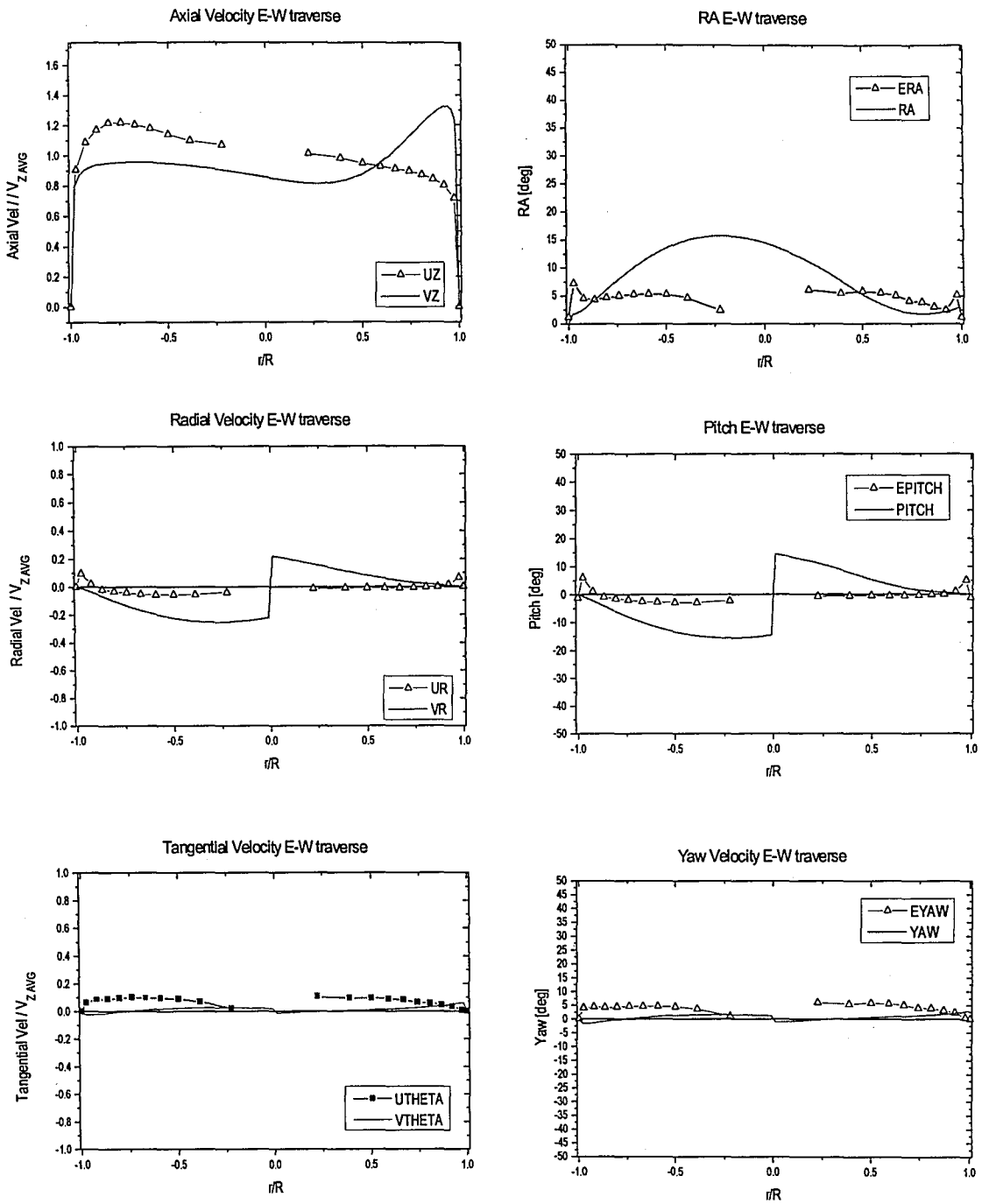

Figure 5.12 (b) Comparison of Experimental Data and Numerical Simulation of E-W Traverse at Station C, Unbalanced Inlet Model, WG Half-Length Model

The secondary flow velocity vector plots provide a view of the vortex transport in the flow and the secondary flow strength and decay at the cross-stream planes. From the experimental and numerical secondary flow patterns, it is evident that at these locations the flow does not present the same structure (Figure 5.13). In the numerical simulation centrifugal forces continue to deform the axial velocity field in downstream locations up to 6 diameters from the inlet. After this point, the flow could be considered to be a flat turbulent velocity profile.

There are a number of reasons why the numerical simulations and the velocity measurements differ. For one, the RNG k-ε turbulence model, although able to predict the qualitative behavior of the flow field after the inlet, cannot predict how the flow evolves due to the presence of strong concentrated vortices. A more complex turbulence model, such as a Reynolds-stress average model, might yield a better approximation of the vortex behavior. One must also ask, "How closely can the numerical solution approximate the conditions present during experimentation, such as slight differences in geometry, very small-scale vibration in the model's wall, and wall roughness effects?

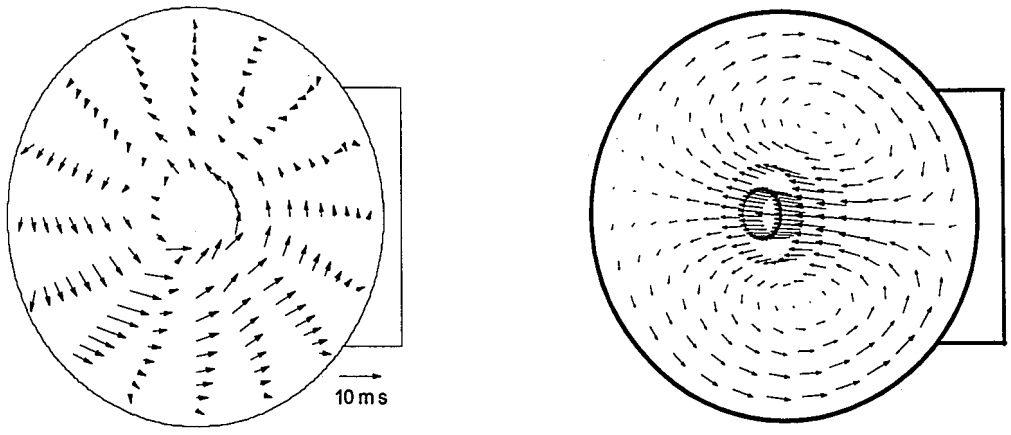

(c) Station C

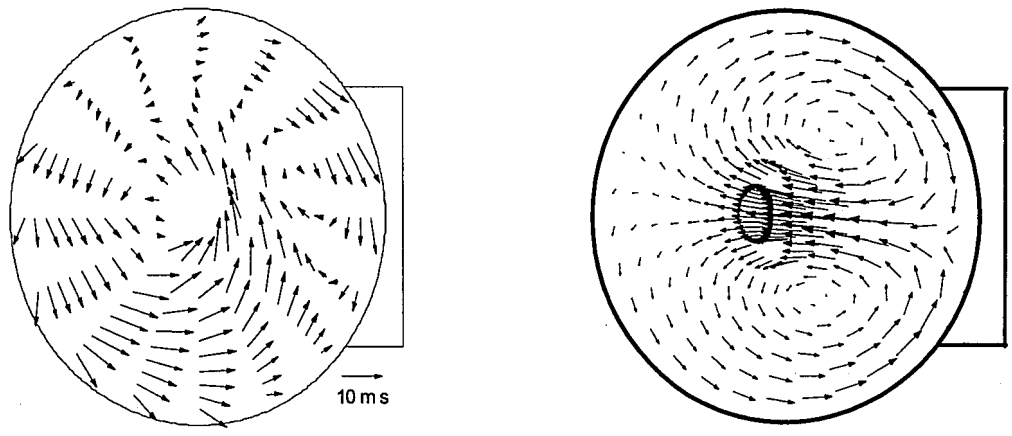

(b) Station B

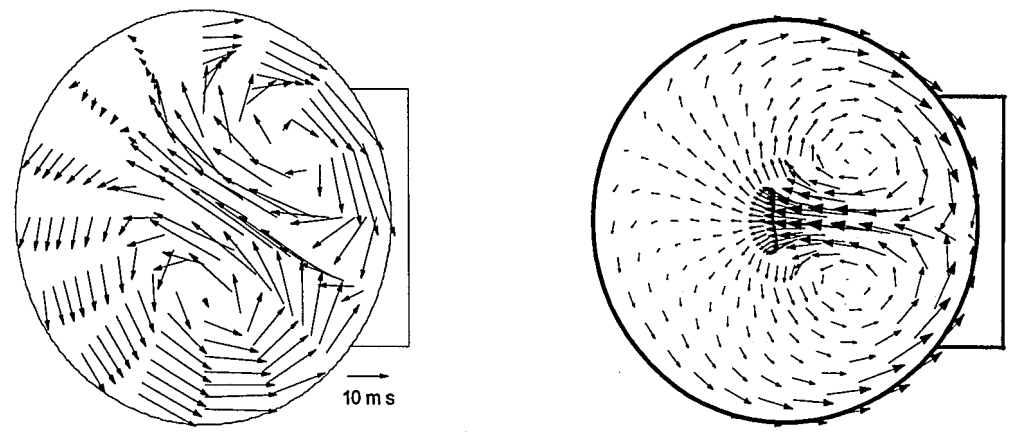

(a) Station A

Figure 5.13 Comparison of Numerical and Experimental Secondary Flow Pattern at Different Axial Locations, Unbalanced Inlet Model, WG Half-Length Model

Chapter 6

Computing Flow Rate and Average Resultant Angle

Introduction

The objective of this chapter is to describe the effect that flow conditions existing in the radial inlet geometry have on flow rate and average resultant angle calculations at different axial locations in the model stack. Emphasis is placed on measurement planes close to the inlet where the strength of the secondary flow is strong enough to affect the results. The variation of flow rate and average resultant angle at the same axial location when computed by data from different sets of radial traverses is also reported. The flow rate and average resultant angle are calculated using EPA procedures described in "CAA 40CFR Pt. 60 Appendix. A, Reference Method 1 and 2."

EPA regulations concerning emission monitoring in stationary sources dictate the use of certain probes for taking velocity measurements and thereby calibrating CEM flow monitors. The most common probe used for CEM flow monitor calibration is the standard S-probe. In the present study, the error associated with the use of an S-probe in the radial inlet stack was predicted using S-probe error data reported by Noble [1996] obtained from Reference [14]. A comparison of alternative procedures for calculating flow rate is presented using experimental data and CFD velocity predictions.

Computing Flow Rate

There are several ways to establish the average velocity across a circular duct from velocity measurements taken at several radial locations. The precision in the flow rate computation depends on mathematical issues, such as the method by which flow rate is computed; and on experimental issues, such as the quantity and quality of the experimental data.

The stack axial velocity field can be described using a cylindrical coordinate system with its origin on the stack centerline, $V_z = V_z(r,\theta,Z)$. At any axial location the flow rate $\dot{m}$ is computed as follows

$$\dot{m} = \rho \int_A V_z \, dA = \rho \int_0^{\pi} \int_0^{R} V_z(r,\theta)\, r \, dr \, d\theta \qquad (6.1)$$

where *A* is the cross-sectional area, ρ is the gas density and *R* is the stack radius. Under the assumption that the axial velocity field has an approximately uniform spatial distribution along the tangential direction, i.e. $V_z(r,\theta) \approx V_z(r)$, it is common practice to discretize Equation 6.1 in using only two perpendicular velocity traverses yielding

$$\dot{m} = \rho \frac{\pi}{2} \int_0^{R} V_z(r)\, r\, dr \Big|_{\theta=0^\circ} + \rho \frac{\pi}{2} \int_0^{R} V_z(r)\, r\, dr \Big|_{\theta=90^\circ}$$
$$\rho \frac{\pi}{2} \int_0^{R} V_z(r)\, r\, dr \Big|_{\theta=180^\circ} + \rho \frac{\pi}{2} \int_0^{R} V_z(r)\, r\, dr \Big|_{\theta=270^\circ} \qquad (6.2)$$

This is shown schematically in Figure 6.1, where a 3-D velocity field is approximated by two perpendicular 2-D velocity profiles, which in turn are integrated by the Equal Area Method, Equation 6.3.

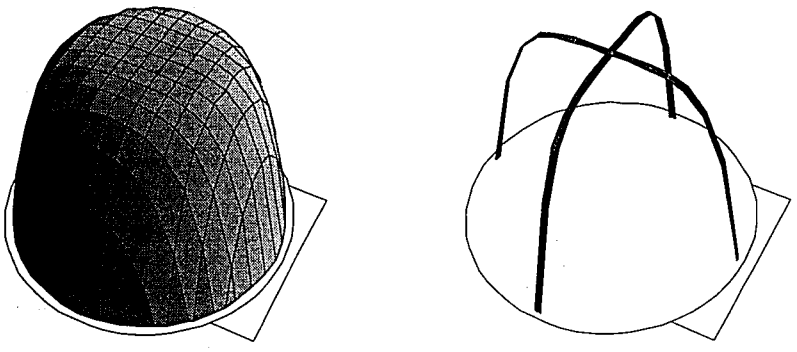

Figure 6.1 Axial Velocity Field approximated using two Perpendicular Velocity Profiles

The Equal Area Method.

The basis for the Equal Area Method is the division of the stack cross-section into equal annular sector areas (Figure 3.1). It is assumed that the measured velocity at the area centroid is representative of the average velocity in that area. For a given number of measurement points, ***N***, the computed flow rate $\dot{m}$ is given by

$$\dot{m} = \rho \, \Delta A \sum_{i=1}^{N} V_i \qquad (6.3)$$

where ΔA is total area A divided by ***N***, ρ is the density of the stack gas, and V_i is the measured axial velocity.

The Equal Area Method introduces a positive bias error into the calculated flow rate by ignoring the no-slip condition at the wall [Elliot 1995, McRanie & Dene 1996, Levy & Eldredge June 1997]. A second source of error results from use of the S-probe in the presence of "mild" cyclonic flow ($\overline{RA} < 20°$) [McRanie & Dene 1996, Levy et al January 1997].

The positions of the measurement points in a circular cross-section are determined using Table 1.2 of "40 CFR Part 60, Appendix A, Method 1," or alternatively they can be computed by determining the centroids of the equal areas, by calculating the radii r_k of the boundaries separating them using the following equation:

$$r_k = R\left(\frac{k}{N}\right)^{1/2} \qquad 0 \le k \le N \tag{6.4}$$

where R is the radius of the cross-section, N the number of equal areas, and k denotes the k^{th} area. The radial position of the centroids X_k are then determined using

$$X_k = \frac{\int_{r_{k-1}}^{r_k} r\,dA}{\int_{r_{k-1}}^{r_k} dA} = \frac{2}{3}\left[\frac{r_k^3 - r_{k-1}^3}{r_k^2 - r_{k-1}^2}\right] \tag{6.5}$$

Modeling S-Probe Velocity Measurements.

The Environmental Protection Agency standardized the design of the Stausscheibe ("S") probe or reverse type Pitot static probe in CAA 40CFR Pt.60, Appendix A Method 2. The S-probe consists of two parallel tubes with openings in opposing directions (Figure 6.2). When inserted into the sampling duct, the probe is oriented such that one of its openings faces directly into the flow stream and the other faces downstream. S-probes are favored in source testing applications because of the susceptibility of the smaller sized conventional Pitot-static tubes to plugging in particulate laden gases [Hall et al, 1976].

In order to study the performance of the S-probe when inserted in the flow field downstream of the radial inlet, experimental velocity data obtained with the prism probe and results simulated using computational fluid dynamics were mathematically biased using

$$V_{S\,PROBE} = (1+\epsilon)\, V_{DATA} \qquad (6.6)$$

where $V_{S\,PROBE}$ is the axial velocity which would be measured by the S-probe, V_{DATA} is the axial velocity obtained from the DA probe or from the numerical simulation, and is the S-probe measurement error from Figure 6.3. The measurement error due to non-axial flow is a function of the local values of Yaw α and Pitch β, and was modeled from experimental results by Noble [1993], obtained from Reference [16].

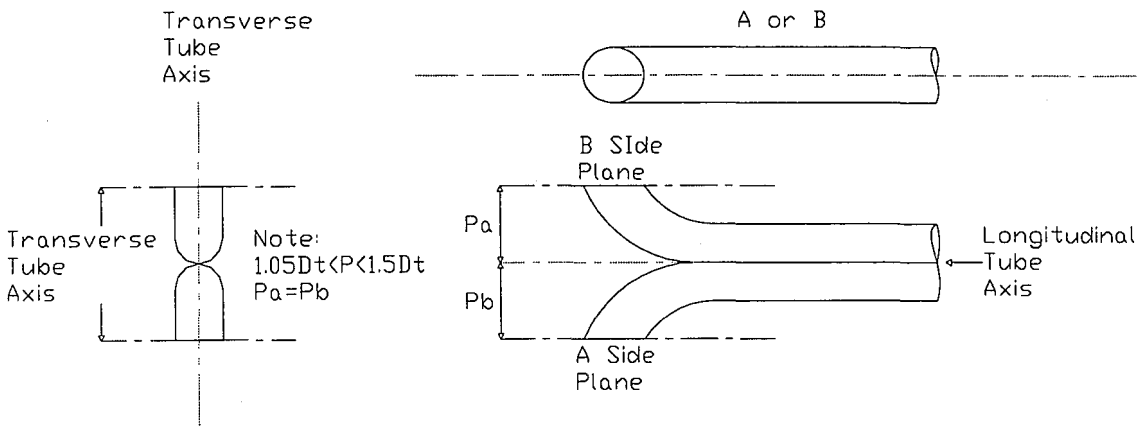

Figure 6.2 Stausscheibe S-Probe

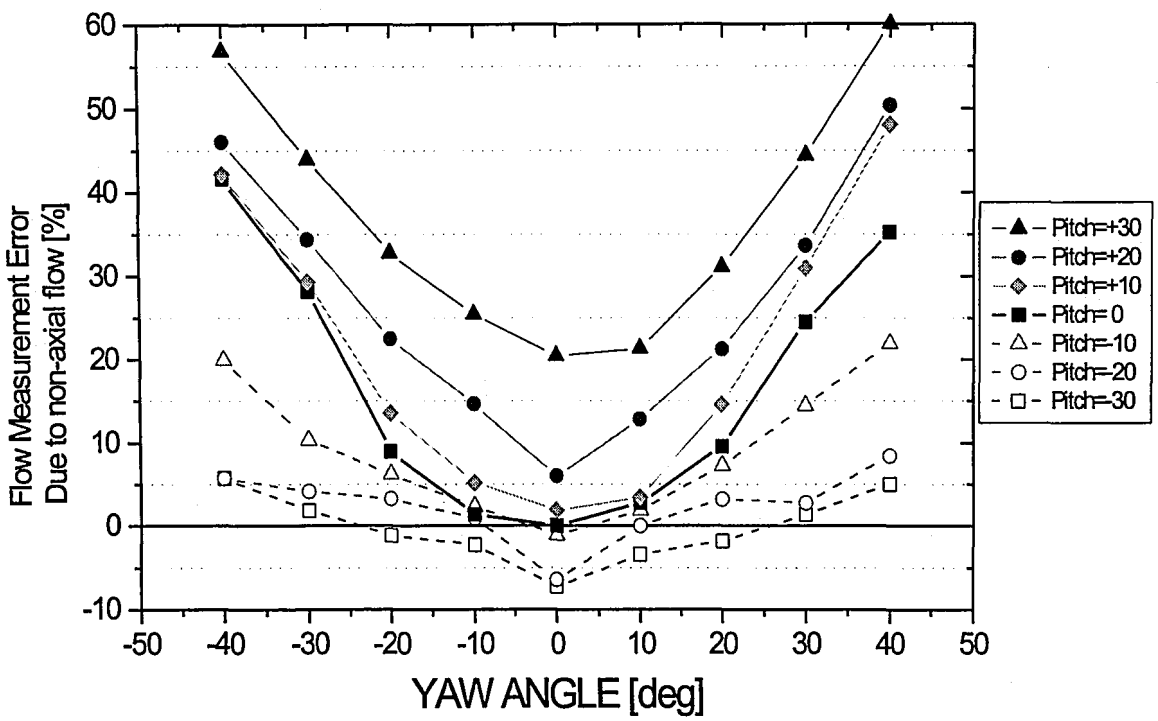

Figure 6.3 Effect of Yaw and Pitch Angles on Flow Measurement Error with Conventional S-probe (data by Noble)

Alternative Procedures

As mentioned earlier, the error in the Equal Area Method arises because the measured velocity at the first point away from the wall is not representative of the average velocity in that area, due to wall effects. Previous work by Eldredge and Levy [1997], evaluated two modifications of the Equal Area Method that account for the no slip condition at the wall. The First Modified Equal Area Method changes the weighting of the equal area points nearest the wall in order to compensate for flow rate over estimation, and is given by

$$\dot{m} = \rho \Delta A \left[\frac{3}{4} V_1 + \sum_{i=2}^{N-1} V_i + \frac{3}{4} V_N \right] \tag{6.7}$$

The second approach, referred to as Curve Fit Integration, is to curve fit the Equal Area points velocity data using cubic splines, and perform a numerical integration to obtain the flow rate. A trapezoidal rule is used to compute the flow in the regions between the wall and the measured points adjacent to the wall.

Although not evaluated in this study, an alternative to the division of the circular cross-section into equal annular areas is presented by Underhill [1993]. His procedure derived from Gaussian quadrature optimizes the spacing of the sampling points, incorporates weighting factors into the quadrature, and implements the no-slip condition in the integration as a boundary condition.

Flow Rate Measurement Error in the Inlet Region

Experimental Results: Effect of Circumerential Discretization and Orientation of Traverses

When the variation of V_Z in the circumferential direction ( ) is considerable, any method based on Equation 6.2 is biased by the velocity profile skewness. So far the influence of this variation with has been overlooked by those performing field measurements in stacks. As long as the flow is not fully developed, this variation should impact the flow rate computation as a positive or negative error.

In the present study, the experimental velocity profiles have 20 data points on a diameter. One set of field data suggests that further discretization in the radial direction has little effect on the value of the flow rate calculation [Sarunac et al; 1998]. Therefore, this analysis isolates the effect of discretization in the circumferential direction. Flow rate error was determined from laboratory velocity measurements taken with the DA probe and computed using the Equal Area Method. Values were calculated using an increasing number of traverse locations in the circumferential direction to assess the total number of measurements needed to reduce the error below a certain level. Due to the fact that in most applications it is not practical to perform more than one set of two perpendicular traverses, flow rate error was also assessed using sets of traverses with different orientations with respect to the inlet duct centerline. Results from this analysis are presented in Table 6.1.

The bias error for the different cases was computed by assuming that the flow rate at Station C (computed by the Equal Area Method using 160 velocity measurements) is the actual flow rate. The relative error ε_{mass} is given by

$$\varepsilon_{i,mass} = \frac{(\dot{m}_i - \dot{m}_T)}{\dot{m}_T} \times 100\% \tag{6.8}$$

where $\dot{m}$ is the mean mass flow for which the error is being evaluated.

Table 6.1 Flow Measurement Error and Average Resultant Angle Values Computed from Measurements Performed at the Model Stack

Layout	θ°	# of Points	Station A.		Station B.		Station C.	
			RA°	ε_{mass} %	RA°	ε_{mass} %	RA°	ε_{mass} %
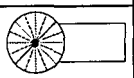	0.0°	160	18.137°	2.433	8.146°	0.010	4.644°	0.0
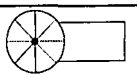	0.0°	80	18.026°	1.858	8.07°	0.103	4.998°	0.087
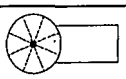	22.5°	80	18.248°	3.009	8.21°	-0.083	4.287°	-0.087
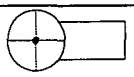	0.0°	40	18.949°	1.207	7.938°	-0.124	4.349°	-0.122
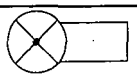	45°	40	17.104°	2.509	8.211°	0.330	5.647°	0.295
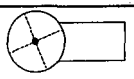	22.5°	40	17.145°	1.708	7.977°	-0.226	4.775°	-0.228
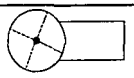	-22.5°	40	19.350°	4.309	8.457°	0.059	3.800°	0.055

Results presented in Table 6.1 confirm that for measurement locations close to the inlet, both average resultant angle and flow rate depend on the number and traverse locations used. Increasing the number of circumferential divisions by increasing the number of diametrical traverses from 2 to 4 narrows down the uncertainty band in the flow rate to ±0.5% (Figure 6.4).

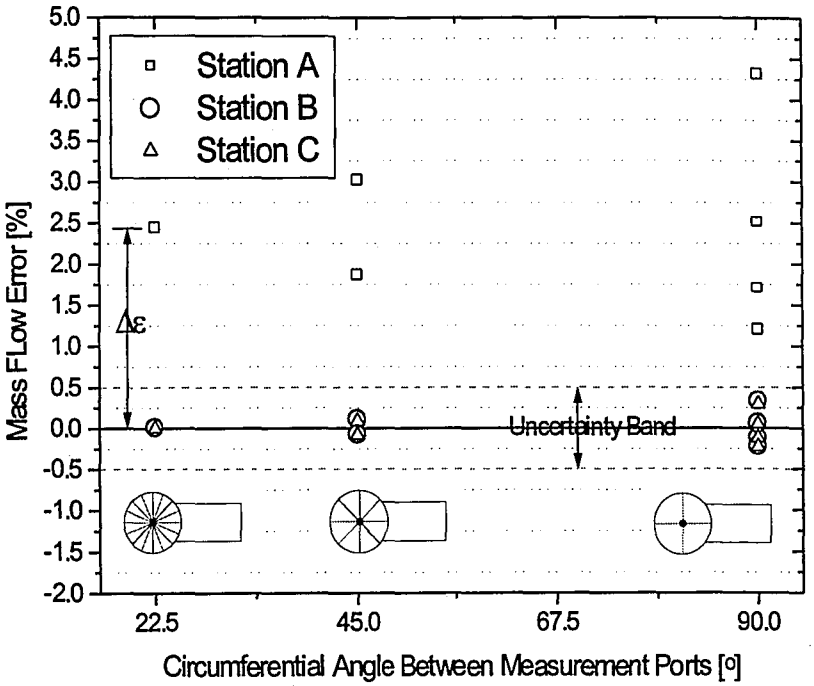

Figure 6.4 Flow Rate Error vs. Circumferential Discretization

Results indicate that in the axial vicinity of Station A, the axial velocity field asymmetry has a strong influence on the flow rate calculation. At this location there is a constant positive bias $\Delta\varepsilon$ in the flow rate calculation which will not decrease, as in the other locations, by further discretizing in the circumferential direction. The origin of this bias is twofold. First, the concentration of high axial velocity fluid in the near wall region of the duct introduces a higher error into the flow rate calculation when using the Equal Area Method. Second, due to the strong variation of V_Z in the radial direction, the calculation suffers from poor discretization in this direction. The flow rate calculation at this location would benefit from an increased number of points per traverse, or from the use of a method such as curve fit integration, which is less susceptible to the variation of V_Z in the radial direction.

Results also indicate that from Station B onwards, the concentration of fluid in one quadrant of the flow results in similar error behavior due to profile asymmetry at Station C. The flow field after Station B, although asymmetric, has a suitable distribution for an equal area sampling.

Flow rate and average resultant angle values calculated with two traverses depend on the orientation of these with respect to the secondary flow. Changing their orientation can either underestimate or overestimate the flow depending on the location of the higher and lower axial velocity regions. For the radial inlet model the set of axes aligned with the inlet duct centerline seem to give the best results at all three locations (Figure 6.5). The average resultant angle, although varying, does not have as strong a dependency on the traverse set used (Figure 6.6). However, its usefulness is questionable since it does not give any real insight into the error behavior, or the secondary flow pattern occurring in the stack. Different patterns may give rise to the same average resultant angle depending on their strength. So validation of results using average resultant angles may be misleading, and therefore a comparison of the secondary flow pattern should be presented to make sense of the average values.

The advantages gained from performing measurements in at least 4 axes, i.e. increasing circumferential discretization, are more accurate values of flow rate and of average resultant angle. Moreover, this information is enough to determine the secondary flow pattern, from which the best traverse orientation can be established.

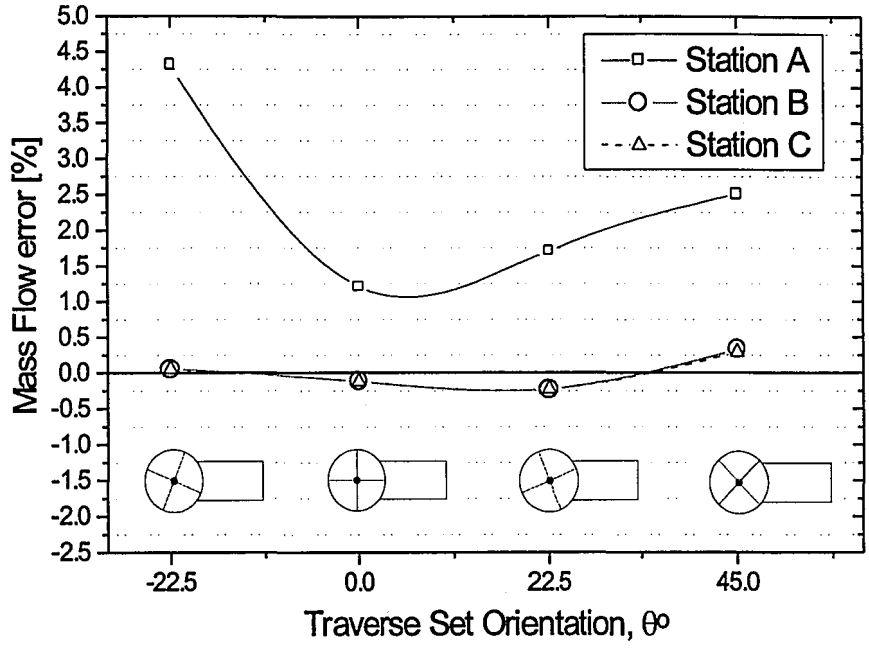

Figure 6.5 Flow Rate Error vs. Traverse Set Orientation

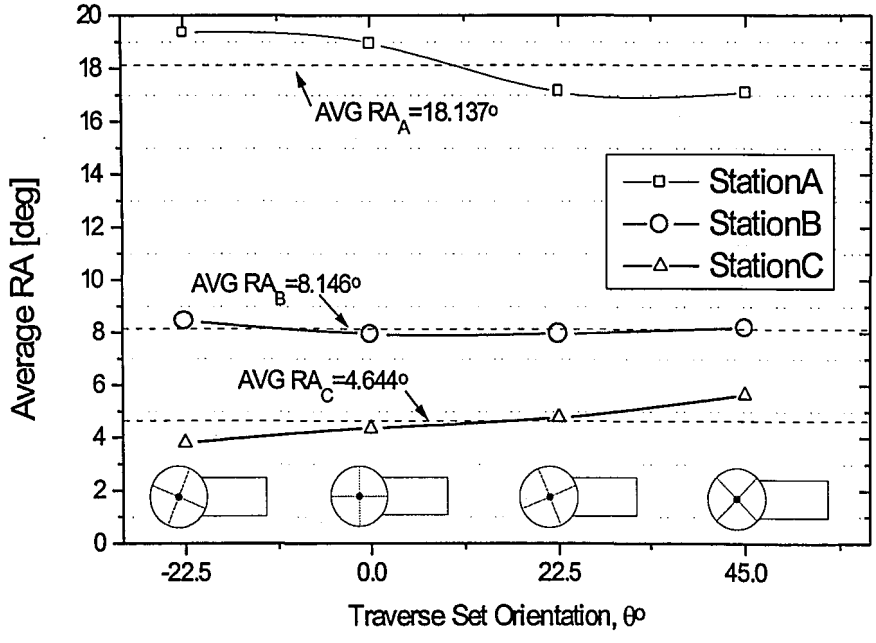

Figure 6.6 Average Resultant Angle vs. Traverse Set Orientation

Simulated S-Probe Results: Effects of Yaw and Pitch Angles on S-probe Error

In the following analysis, the DA probe traverse data were used in conjunction with Figure 6.3 and Equation 6.6 to estimate the S-probe bias error in the flow rate calculations. The objective of this was to model the effect of performing measurements with an S-probe in locations close to the inlet of stacks that present a flow structure with counter-rotating vortices in cross-sectional planes. Results are presented in Table 6.2. The effect of the S probe bias is particularly noticeable at Station A, where the positive bias error is 7.77% when using 160 equal area points. Results show a positive bias that does not decrease with an increase in measurement points (Figure6.7).

Table 6.2 Predicted S-probe Flow Measurement Error using Noble's Data for S-probe error with measured Yaw and Pitch Angles.

Layout	θ°	# of Points	Station A.		Station B.		Station C.	
			RA°	ε_{mass} %	RA°	ε_{mass} %	RA°	ε_{mass} %
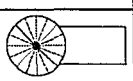	0.0°	160	18.137°	7.772	8.146°	1.453	4.644°	0.456
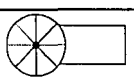	0.0°	80	18.026°	7.133	8.07°	1.548	4.998°	0.582
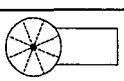	22.5°	80	18.248°	8.411	8.21°	1.357	4.287°	0.330
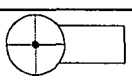	0.0°	40	18.949°	5.954	7.938°	1.229	4.349°	0.148
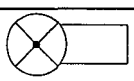	45°	40	17.104°	8.311	8.211°	1.868	5.647°	1.017
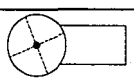	22.5°	40	17.145°	7.259	7.977°	1.313	4.775°	0.294
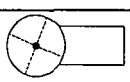	-22.5°	40	19.350°	9.563	8.457°	1.401	3.800°	0.366

Traverse orientation has a significant impact on accuracy when performing S-probe measurements. The radial inlet secondary flow pattern presents a high radial velocity region at the vortex pair interface. This translates into a high pitch component about any radial traverse that is closely aligned with it. S-probes are particularly sensitive to pitch (Figure 6.3), and therefore any traverse which is in close alignment with the vortex structure interface will introduce a higher measurement error in the flow rate calculation (Figure 6.8).

At Station A, the traverse sets @ -22.5° and 45° show S-probe measurement errors as high as 9.56%. This measurement error, which is composed of errors due to flow profile asymmetry, S-probe bias, coarse discretization (in both radial and circumferential directions), and an accentuated Equal Area Method error due to high axial velocity in the near wall region, can be considered a worst case scenario. This analysis does not take into account additional biases such as wall proximity effects on the probe and the no-slip condition at the wall. However, it is clear that for this geometry, errors higher than 10% are unrealistic or are due to very different reasons, such as the implementation of the measurement procedure in a full scale application.

Station B and C have comparatively uniform error behavior with respect to Station A. At these locations, the vortex pair has positioned itself in such a way that its interface is not aligned with the measurement axes, and therefore does not impart a radial component into the flow.

It would appear that the location and manner in which the vortex pair merges into a single vortex presents regions that are better suited for performing flow rate measurements. Using the S-probe error data (Figure 6.3) to map the S-probe error zones (Figure 6.9), it can be confirmed that at Station A, the error is mostly due to the two-cell interface. At station B, the error zone is pressed against the stack walls and lies in one quadrant of the cross-section. At Station C the flow has redistributed itself and the secondary flow strength is almost negligible, thus imparting a small error of the order 0.5% into the measurement. Error in this location is mostly due to the asymmetry in the axial velocity profile.

In industrial installations the orientation of the interface and the axial location where the vortex cells merge in the radial inlet stacks are probably site specific and flow rate dependent. This dependency is really a function of the parameters that affect the shape of the inlet velocity profile, and of geometric considerations such as dimensional symmetry. However, any variation in length of the vortexes and orientation of the cells will remain within a certain range.

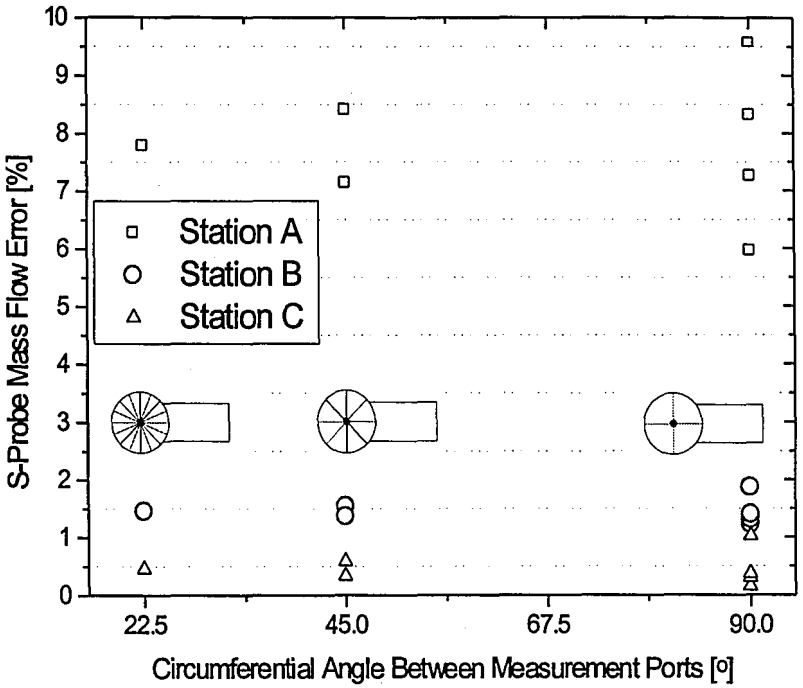

Figure 6.7 S-Probe Flow Rate Error vs. Circumferential Discretization

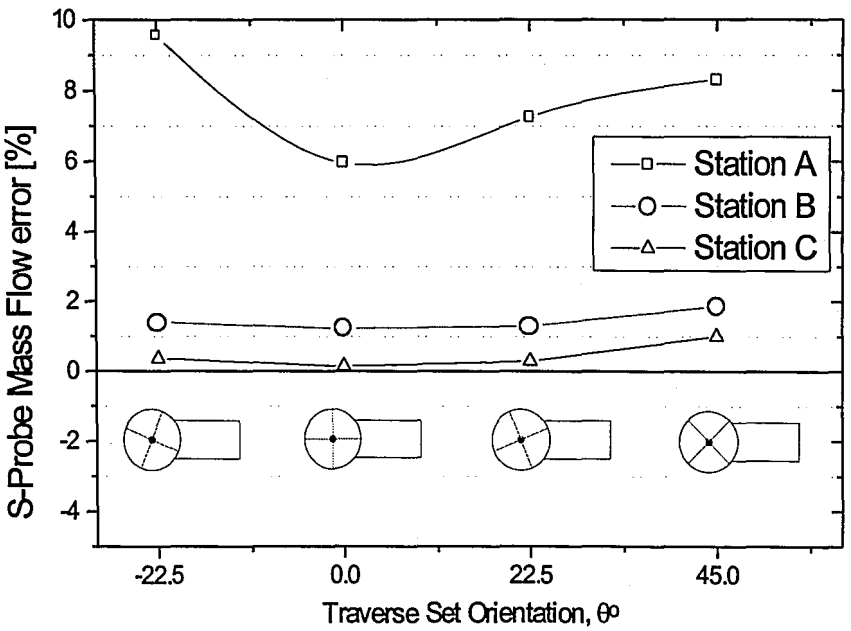

Figure 6.8 S-ProbeFlow Rate Error vs. Traverse Set Orientation

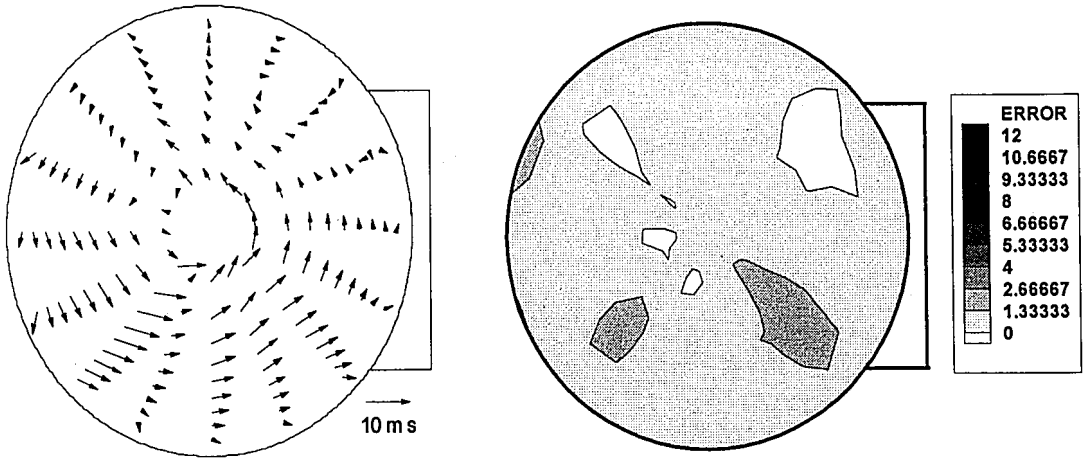

(c) Station C

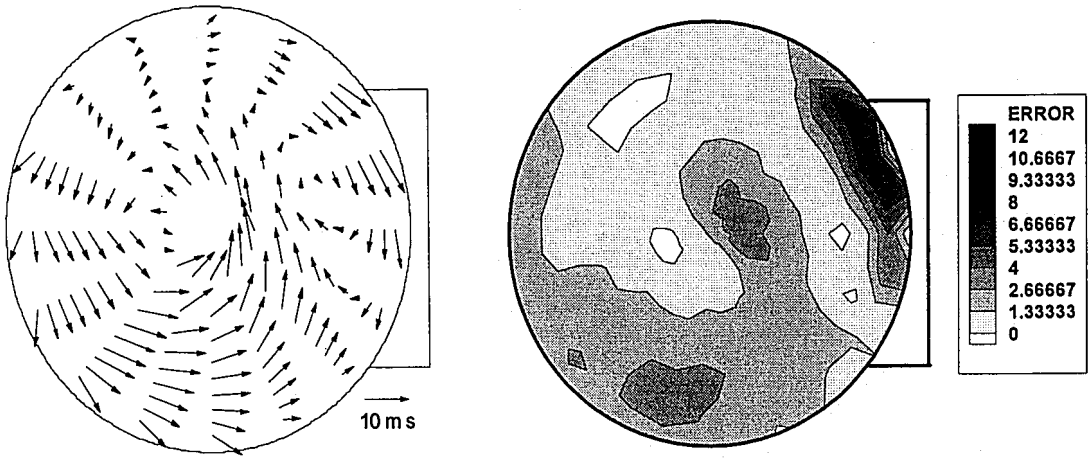

(b) Station B

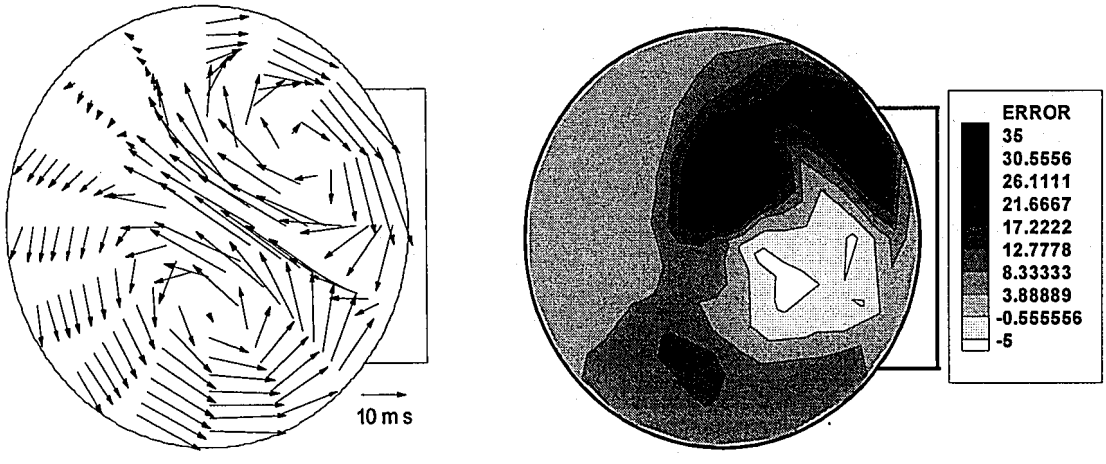

(a) Station A

Figure 6.9 S-Probe Flow Rate Error Maps

Numerical Results

When using experimental data there are limits on the amount of measurements that can be taken in a given time period. However, the use of computational fluid dynamics has no such restriction. By extracting data in a limited fashion from a numerical simulation and comparing it with the same results extracted in detail, the effect of lack of information in the calculated flow rate can be assessed.

Flow field information was extracted from the computational fluid dynamics simulation in two ways: first, two perpendicular traverses oriented and referred to as the N-S traverse and the E-W traverse (Figure 5.4) with 20 equal area points each were extracted every 0.10 m along the stack axial direction. It was then possible to evaluate flow rate calculation methods as a function of axial position. Second, 16 radial velocity profiles with 100 points each at Station C (3.88 diameters from the inlet), and at Station D (20.56 diameters from the inlet) were extracted from the simulation.

As previously stated, the asymmetry in the velocity profiles may give rise to an error in computing flow rate using any method based on Equation 6.2. The base value used to calculate the error is computed at Station D by numerically integrating the N-S traverse and the E-W traverse with 100 points using a trapezoidal rule. This value can be interpreted as the "best" flow rate computation achievable with the restriction of two measurement traverses.

The mathematical error associated with profile asymmetry should decrease rapidly some distance after the inlet. Figure 6.10 shows such behavior, where just after the inlet there is a peak in the flow rate error caused by the difference in shape of the axial velocity profiles. After Station C, the flow profiles quickly tend towards a steady value. Therefore, from this location onwards, the Equal Area Method tends to overestimate the flow by 1 % on average. The 1st Modified Equal Area Method underestimates the flow by 0.6% on average. Finally, Curve Fit Integration presented excellent results having a 0.01% error on average. The Curve Fit Integration procedure used in this study was based on the method described by Eldredge and Levy [1997]. Curve Fit Integration is also susceptible to the coarse integration step in θ. However, it is almost insensitive to a sharp variation of axial velocity in the radial direction, and therefore it reaches the true flow rate faster. An error comparison for Station C and D is presented in Table 6.3.

Table 6.3 CFD Error Comparison for Station C and D

	Curve Fit ε%	**Equal Area Method ε%**	**1st Mod. Equal Area Method ε%**
Station C	0.1854	1.2893	-0.5932
Station D	0.0416	0.8302	-0.5049

In order to model the effect of using an S-probe, the previous numerical results were biased using Equation 6.6. As the flow advances through the stack it becomes fully developed. Therefore, after Station C, the curves converge slowly towards a steady error. The Equal Area Method overestimates the flow by 1.25 % on average. The 1st Modified Equal Area Method tends to underestimate the flow by 0.5% on average. In this case, the overestimation of the S-probe is compensated for by the underestimation of the method. Curve Fit Integration presented excellent results showing the same 0.01% error on average. An error comparison for Station C and D is presented in Table 6.4 for biased results.

Table 6.4 Predicted S-probe Flow Measurement Error using Noble's Data for S-probe error with Numerical Yaw and Pitch Angles

	Curve Fit ε%	**Equal Area Method ε%**	**1st Mod. Equal Area Method ε%**
Station A	0.5869	1.6937	-0.2057
Station D	0.0595	0.8481	-0.4872

Close inspection of the data showed that the reason for the small error difference between Figure 6.10 and Figure 6.11 is that the symmetrical secondary flow pattern solved in the simulation cancels out its error, because, for the range α = 10° (YAW) and β = 10° (PITCH) the S probe error chart presents regions of underestimation and overestimation of velocity.

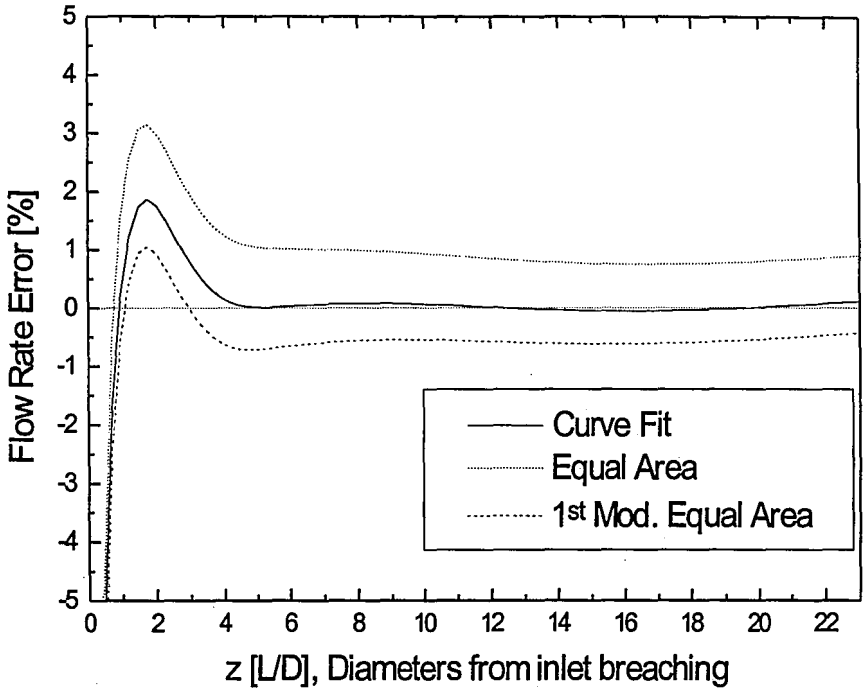

Figure 6.10 CFD Flow-Rate Error at different Stack Elevations

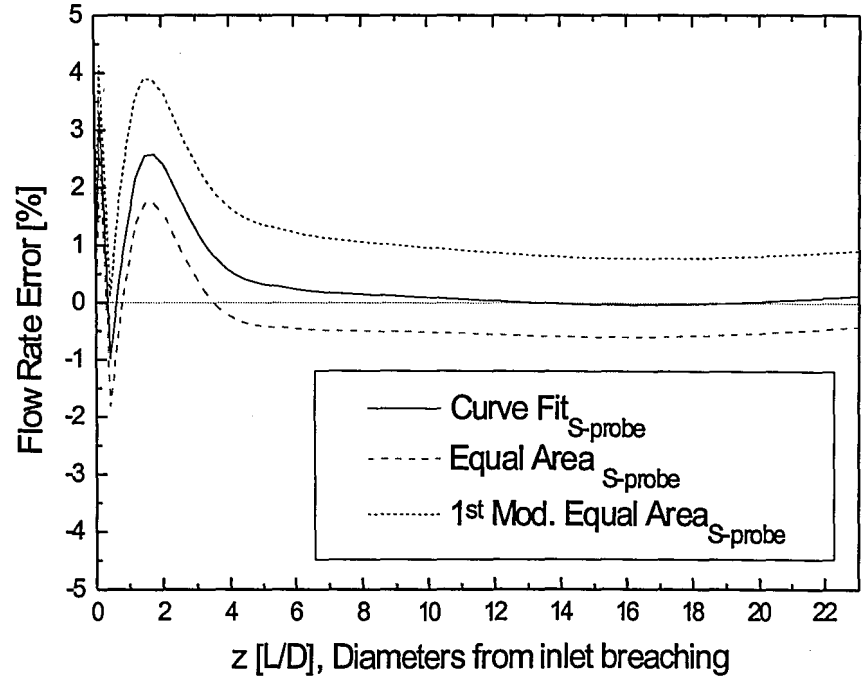

Figure 6.11 CFD S-Probe Flow-Rate Error at different Stack Elevations

Chapter 7

Conclusions and Recommendations for Future Work

Conclusions

Flow characteristics occurring in a stack with a radial inlet geometry were investigated using a $1/10^{th}$ scale laboratory model. The model's dimensions were 0.4572 m (18 in) in diameter and 12.1 m (476.4 in) in length. Experimental results of axial velocity, secondary flow, and swirl were studied for planes located at 1.01, 2.44, and 3.88 diameters from the downstream corner of the inlet breaching. The average axial velocity in the stack was approximately 37 m/s (121.4 ft/s). Three-dimensional velocity measurements were collected in the inlet region using a type DA three-dimensional velocity head probe.

As the inlet stream is forced into the stack, the flow abruptly changes direction. As a result the velocity distribution becomes highly non-uniform, generating secondary flows in cross-stream planes downstream of the inlet. The radial inlet geometry induces a counter-rotating vortex pair that evolves into a single vortical secondary flow structure a short distance after the inlet.

It was found that for measurement locations close to the inlet, the configuration of the axial velocity field and the strength of the secondary flows can affect average resultant angles and flow rate measurements, depending on the number and position of the traverse locations used.

Flow rate values determined with two traverses depend on their circumferential orientation. Changing their orientation can either underestimate or overestimate the flow by as much as 4.3%, depending on the axial location of the measurement plane. At this location, flow rate measurement error is governed by the asymmetry in the axial velocity profiles, which is, in turn, determined by the cross-sectional region with a concentration of high axial velocity fluid.

Increasing the number of diametrical traverses from 2 to 4 narrows down the uncertainty band in the flow rate measurements to ±0.5%. The advantage gained from performing measurements in at least 4 axes, is a more accurate value of flow rate and of average resultant angle, although the average resultant angle does not have as strong a dependency on the traverse set used. Moreover, the 4 axes information is enough to determine the secondary flow pattern, from which the best traverse orientation can be established.

Three-dimensional velocity measurements and numerical results were used in conjunction with S-probe error data reported in the literature to estimate the S-probe bias error in the flow rate calculations. The effect of S probe bias in locations close to the inlet where counter-rotating vortices were present, was particularly noticeable at 1.1 diameters from the inlet, where the error was approximately 7.7% even when using 160 equal area points. An increase in the number of circumferential measurement points did not reduce the positive bias.

Traverse orientation has a higher impact on accuracy when performing S-probe measurements. The radial inlet secondary flow pattern presents a high

radial velocity region at the vortex pair interface. Because S-probes are particularly sensitive to pitch, i.e. radial velocity, the set of axes aligned with the vortex structure interface will cause a relatively high measurement error.

A comparison of alternative procedures to compute flow rate showed that Curve Fit Integration, although susceptible to flow asymmetry, is almost insensitive to a sharp variation of axial velocity in the radial direction, and therefore, it reaches the true flow rate faster.

The flow field was modeled numerically using a two-equation turbulence model (RNG k-ε). A comparison between the experimental and numerical secondary flow patterns showed that the RNG k-ε turbulence model, although able to predict the qualitative behavior of the flow field after the inlet, does not accurately predict how the flow evolves due to the presence of strong concentrated vortices.

It would appear that the location and manner in which the vortex pair merges into a single vortex presents regions that are better suited for performing flow rate measurements. In industrial installations the orientation of the interface and the axial location where the vortex cells merge are likely to be site specific and flow rate dependent. This dependency is really a function of the parameters that affect the shape of the inlet velocity profile, and geometric considerations such as dimensional symmetry.

Recommendations for Future Work

The following is a list of recommendations for further study of some of the aspects related to flow characteristics in power plant stacks.

- Perform detailed three-dimensional velocity measurements in stacks with offset inlets to investigate the effect traverse (circumferential) orientation has on flow rate accuracy for these geometries.

- Perform computational fluid dynamics simulations with higher order turbulent models to improve modeling predictions of the wall bounded vortex pair interaction.

- Determine a proper combination of inlet turning vane and flow conditioner in stacks with different inlets. The results of this analysis will be used for the design and location of the flow conditioning elements.

References

[1] "Steam, Its Generation and Use," Babcock and Wilcox Company, 40th edition, 1992.

[2] Becker H.A, and Brown A.P.G., (1974), "Response of Pitot Probes in turbulent Streams," Journal of Fluid Mechanics, Vol. 62, Pt.1, pp. 85-114.

[3] Code of the Federal Registry, (1998), " (CFR) CAA title IV, Acid Rain Deposition Control Requirements."

[4] Dalbec D., (1993), "Flow Patterns and Measurement Accuracy in a Scale Model of a Power Plant Stack," M.S. Thesis, Lehigh University, 1993.

[5] Elliot T. C., (1994), "Monitoring Emissions, Instrumentation Aims for Total System Commitment," Power, June 1994, pp. 42-60.

[6] Elliot T.C., (1995), "CEM System," Power, May. 1995, pp. 31-40.

[7] Environmental Protection Agency, (1998), "Monthly Average Price of Sulfur Dioxide Allowances Under the Acid Rain Program," Update Report, Environmental Protection Agency, August 1998.

[8] Eldredge T. V., (1996), "Computational Fluid Dynamics Modeling for the Brunner Island Unit 3 Stack", Lehigh University Energy Research Center, Report No. 96-400-21-28, June 1996.

[9] Eldredge T. V., and Levy E.K., (1998), "CEM Flow Accuracy Project Phase II," Lehigh University Energy Research Center, Draft Report. November 1998.

[10] Gretta W.J., Grieco G.J., (1995), "Consideration of Scale in Physical Modeling of Air Pollution Equipment," Joint Power Generation Conference ASME 1995, Vol. 1, pp. 109-116.

[11] Hall J.L., Leland B.J., Joensen A.W., Carrol J.M., (1976), "Correction of S-Type Pitot-Static Tube Coefficients when used for Isokinetic Sampling from Stationary Sources," ASME Winter Annual Meeting, New York 1976.

[12] Hinze, J. O. (1959), "Turbulence," McGraw-Hill, 3rd ed., 1975.

[13] Idelchik I.E. (1994), "Handbook of Hydraulic Resistance," CRC Press, 3rd ed., 1994.

[14] Jones W.P., Launder, B.E. (1972), "The Prediction of Laminarization with a Two-equation Turbulence Model," International Journal of Heat and Mass Transfer, Vol. 15, pp. 301-314.

[15] Kok J.B.W. and Van der Wal S.(1996), "Mixing in T-Junctions," Applied Mathematics Modeling, Elsevier, Vol. 20, March 1996.

[16] Levy E.K., Eldredge T. V., Roache J., (1997), "Effects of Flow Conditions on Accuracy of Stack Flow Instrumentation," Lehigh University Energy Research Center, Report No. 97-500-01-01, January 1997.

[17] Levy E.K., Eldredge T. V., (1997), "Analysis of Errors in the EPA Equal Area Method Using Computational Fluid Dynamics," Memorandum Energy Research Center, Lehigh University, June 1997.

[18] McRanie R. D., Dene C. E., (1996), "The Electric Power Research Institute Continuous Emission Monitoring Heat Rate Discrepancy Project," Environmental Protection Agency, Update report, December 1996.

[19] Merriam, K. G., Spaulding (1935), E. R. "Comparative Tests of Pitot-Static Tubes," NACA TN 546, Nov. 1935.

[20] Mitchell W.J., Blagun B.E., Johnson D. E., Midgett M.R., (1979), "Angular Flow Insensitive Pitot Tube Suitable for Use with Standard Stack Testing Equipment," EPA 600/4-79-042, NTIS June 1979.

[21] Panton R.L., "Incompressible Flow," John Wiley and Sons, 2nd edition, 1996.

[22] Patankar S.V., Spalding D.B. (1972), "A Calculation Procedure for Heat, Mass and Momentum Transfer in three dimensional Parabolic Flows," Int. Journal of Heat and Mass Transfer, Vol. 15, 1787.

[23] Patankar S.V. (1980), "Numerical Heat Transfer and Fluid Flow," McGraw-Hill, 1st edition, 1980.

[24] Reader-Harris M.J. (1994), "The Decay of Swirl in a Pipe," Int. Journal of Heat and Mass Transfer, Vol. 15, No. 3, pp. 212-217, June 1994.

[25] Rhie C.M. (1981), "A numerical Study of the flow past an isolated Airfoil with Separation," Ph.D. Thesis Dept. of Mech. And Indust. Eng., Univ. of Illinois at Urbana-Champaign.

[26] Rhie C.M., Chow W.L. (1983), "Numerical Study of a Turbulent Flow Past an Airfoil with Trailing Edge Separation," AIAA Journal, Vol. 21, pp. 1525-1532.

[27] Rossow V.J., (1991), "Probe Shapes for Streamwise Momentum and Cross-Stream Turbulence Intensity," Journal of Aircraft, Vol. 28, No. 11, November 1991.

[28] Sarunac N., Eldredge T.V., Levy E.K., Bilirgen H. (1998), "Stack Flow Measurement Accuracy at Morgantown Unit 2," Lehigh University Energy Research Center, Report No. 98-400-15-19, July 30, 1998.

[29] Tang Y. D., Ou J. J., Heist R.H., Chen S. H., Dukat A.J., Eberle A.C., (1993) "Dynamics of Fluid Mixing Induced at a T-Junction," Ind. Eng. Chem. Res. 1993, Vol. 32, pp. 1727-1733.

[30] Thompson J.F., Warsi Z.U., Mastin C.W. (1985),"Numerical Grid Generation," Elsevier, 1st edition, 1985.

[31] Underhill D.W., (1993), "A New Quadrature for Determining the Mean Duct Velocity," Air & Waste, Vol. 43, pp. 1493-1499, November 1993.

[32] "Calibration Data for Type DA & DAT 3-Dimensional Directional Probes," United Electric Controls Company, United Sensor and Control Corp., 1993.

[33] "Theory and Application of Fluid Flow Probes," United Electric Controls Company, United Sensor and Control Corp., Technical Bulletin T-2, 1993.

[34] Ward-Smith A.J., "Internal Fluid Flow," Oxford University Press, 1980.

[35] White F. M., "Fluid Mechanics," pp. 285-287, McGraw-Hill, Third edition 1994.

[36] Wilcox D.C., (1994), "Turbulence Modeling for CFD," DCW Industries, 1st edition 1994.

[37] Wilson S.M., Wright T., (1988), "Alternate Probe Geometries for three component Velocity Measurement in Large Scale Applications," ASME, 88-JPGC/PTC-4, U.S.A. 1988.

[38] Yakhot, V., Orzag, S.A., (1986), J. Scientific Engineering, Vol. 1, 1986.

[39] Yilmaz A. (1997), "Roping Phenomena in Lean Phase Pneumatic Conveying," Ph.D. Dissertation Lehigh University, 1997.

[40] Yin M., Shi F. & Xu Z., (1996), "Renormalization group based *k-e* turbulence model for flows in a duct with strong curvature," Int. Journal of Engineering Science 34, 243-248.1996.

[41] Yu S.C.M., Kitoh O. (1994), "A General Formulation for the Decay of Swirling Motion along a Straight Pipe," Int. Communications in Heat and Mass Transfer, Vol. 21, No. 5, pp. 719-728, 1994.

Appendix A-Total Velocity Head Probes

Total velocity head probes produce a pressure reading that is directly related to the local flow velocity at a measuring point at the tip of the probe. They give a reliable measurement of the local flow velocity in both laminar and turbulent flow regimes. Also, there is a considerable amount of information documenting expected measurement error associated with the use of such probes in different applications. A list of references on the subject can be found in Rossow [1991].

Total velocity head probes operate on the principle that a moving fluid exerts pressure on any object placed in its path. This pressure, which is termed impact pressure or total pressure P_T, is the sum of the dynamic pressure P_d and the static pressure P_S. Dynamic pressure is a measure of the momentum of the molecules in the fluid resulting from their movement in the overall direction of fluid flow, while static pressure is a measure of the random motion of molecules that exists in all fluids whether moving or at rest [Mitchell et al, 1979]. By determining P_s, P_T, and the fluid density ρ, it is possible to determine the velocity *V* of the fluid using the following equation:

$$\begin{aligned} P_T &= P_S + P_d \\ P_d &= P_T - P_S = \frac{1}{2}\rho V^2 \\ V &= \sqrt{\frac{2}{\rho}(P_T - P_S)} \end{aligned} \tag{A.9}$$

Note that in Equation A.1 the velocity is proportional to the square root of the pressure drop.

Pitot Probe

The accuracy in measuring static and total pressure of Pitot tubes is a function of yaw, pitch, orifice size and velocity. Merriam and Spaulding [1935] designed and evaluated a Pitot Static tube that had a predictable degree of error under most flow conditions. This Pitot tube became the basis for the ASME and ASTM Pitot tubes. Because of its long tip and small orifices this type of tube is not generally applicable for stack testing.

The response of a Pitot probe in a uniform laminar stream is expressed in the form of Equation A.1. The response in a turbulent stream, where the velocity vector fluctuates in both magnitude and direction, is based on knowledge of the directional response in a laminar stream. Assuming that the turbulence scale is large compared with the critical probe dimensions, the flow around the probe is locally quasi-steady, quasi-uniform and quasi-laminar and the instantaneous signal pressure in the probe head is virtually the same as in a steady uniform laminar stream. The time-mean response is formed by time averaging the instantaneous signal. H.A. Becker and A.P.G. Brown [1974] indicate that the previous assumption fails when the turbulence scale is small relative to the probe dimensions, or when the frequency response characteristics of the probe affect the results.

For axisymmetric Pitot probes, the incoming flow can be represented using a Cartesian (x,y,z) reference frame, with origin at the center of the probe mouth, x axis along the probe axis and x positive in the direction into the probe, Figure (A.1). Since the plane of the probe mouth is perpendicular to the probe axis, the resultant angle **RA** is defined as the angle between the axis and the stream velocity *V*; the **RA** can also be unambiguously called the angle of incidence of *V* on the probe. The velocity *V* may be resolved into $V_x = V\cos(RA)$ and $V_n = V\sin(RA)$. The component V_n is outward, normal to the probe axis and represents the stream speed in the plane of the probe mouth.

For a round nosed Pitot probe, i.e. a hemispherical truncated tube the effect of orientation in laminar flow is described by

$$P_d = P_T - P_S = C\frac{1}{2}\rho V^2 \qquad \text{(A.10)}$$

Under these conditions, the coefficient *C* depends only on the diameter ratio D_i/D and the external geometry. Information on *C* for standard Pitot static probes can be found in ASTM D 3796-90.

In the analysis developed by Becker and Brown [1974], the following generalization, Equation A.3, describes most results within the margins of experimental error.

$$P_d = P_T - P_S = \frac{1}{2}\rho V^2\left(1 - K\left(\sin^2(RA)\right)^m\right. \qquad \text{(A.11)}$$

Where *K* and *m* are constants for a given probe, for ideal transverse response *m=1*, for ideal total response *m=∞*, and for real probes *1<m<∞*. The Pitot probe used in this study has the following characteristics $D_i/D = 0.35$, m=1.665, and K=1.75, where K and m were evaluated using results presented in Reference [2]. Figure A.2 shows that for an incidence angle in the range $-12 < \theta < 12$, the probe measures 98% of the ideal total static response.

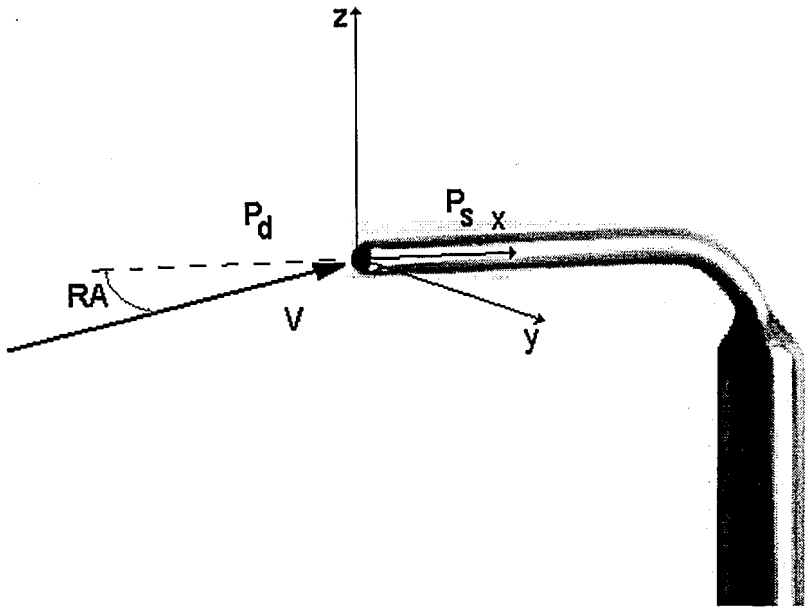

Figure A.1 Pitot Tube

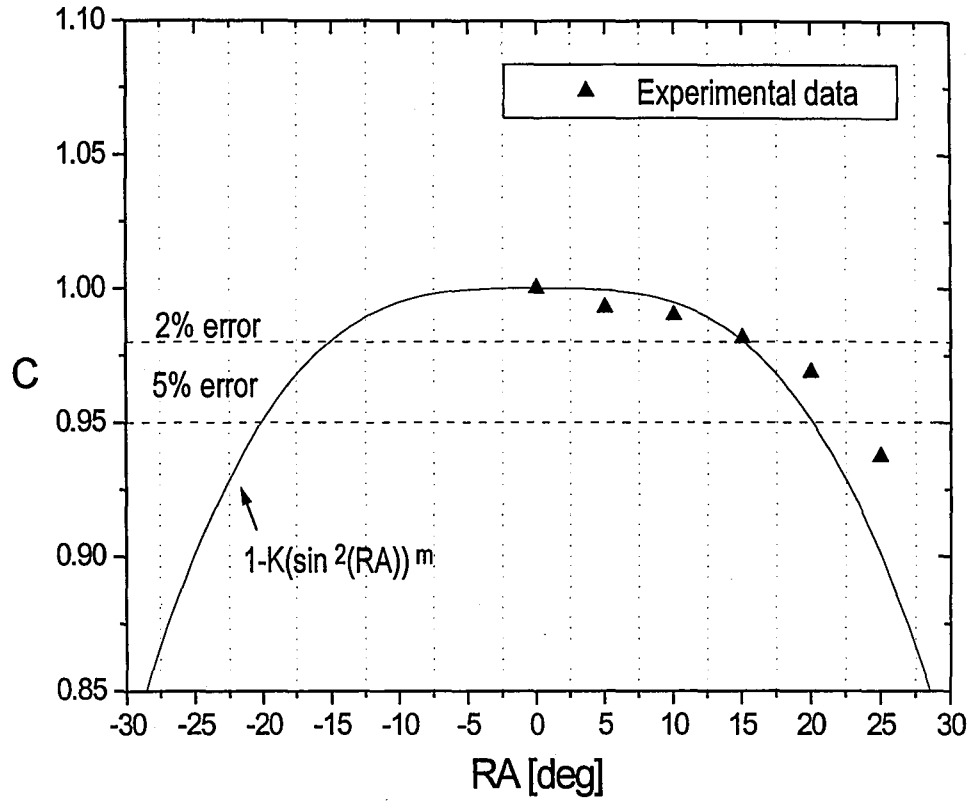

Figure A.2 Effect of Resultant Angle on Pitot Tube Accuracy, Experimental Data, Reference [9]

Five Hole Type DA "3D" (Prism) Probe.

The type DA "3D" directional (Prism) probe is capable of resolving a three-dimensional velocity vector as a magnitude and two angles. The Prism probe has 5 pressure sensing ports (Figure A.3). In this design, two ports are used to produce a differential pressure unique to the first angle, yaw (α). Two additional ports are used to produce a differential pressure calibrated to the second angle, pitch (β). The final port indicates the total pressure P_T. Static pressure is determined by calibrating the output of one of the yaw and pitch sensing ports to the known static pressure P_S, Reference [33].

The Prism probe senses the dynamic pressure and its orientation using two angles; yaw (α) and pitch (β). The five ports serving as pressure taps on the probe tip are numbered 1 through 5. Once the probe is in the flow, it is rotated about its axis aligning it with the direction of the flow, i.e. the probe is nulled or balanced in the yaw angle (Figure A.4). This procedure, known as single-null method, requires a calibration curve of the pitch pressure differential coefficient $(P_4 - P_5)/(P_1 - P_2)$ over a range of pitch angles. The probe is properly oriented when the pressure readings at holes 2 and 3 are equal, Reference [21]. When the probe is properly oriented, the dynamic pressure is measured P_{DYN}. The dynamic pressure is the difference between the total pressure P_T, port 1, and the static pressure P_S, port 2.

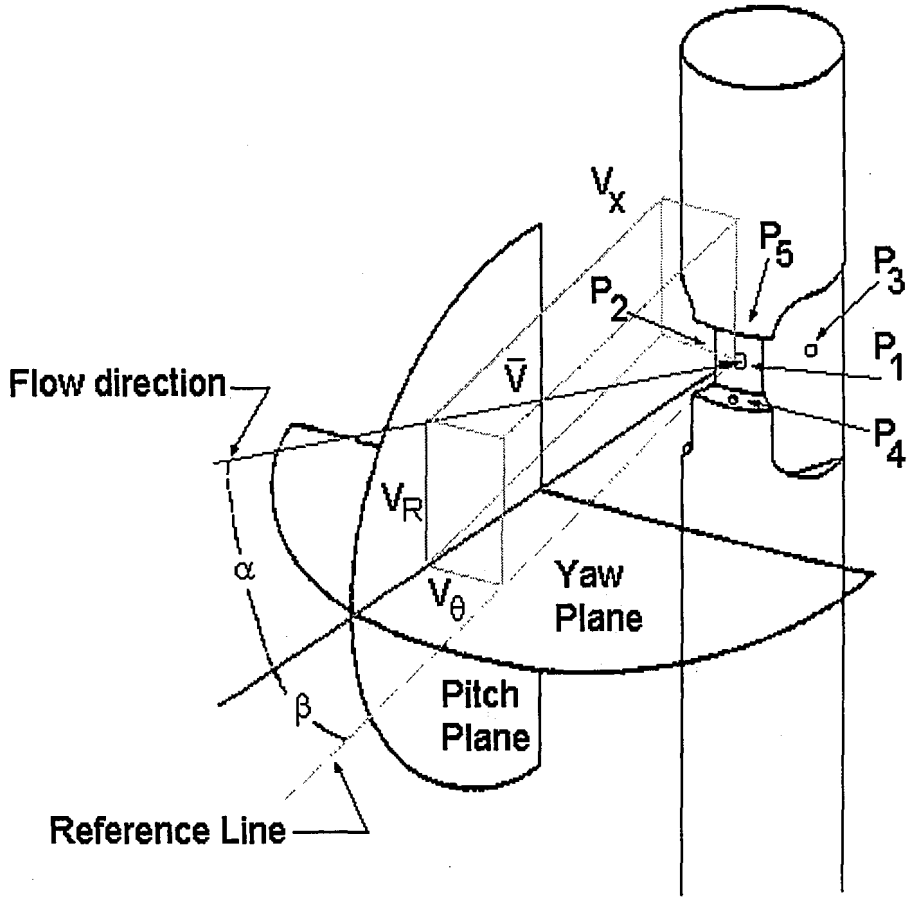

Figure A.3 Prism Probe.

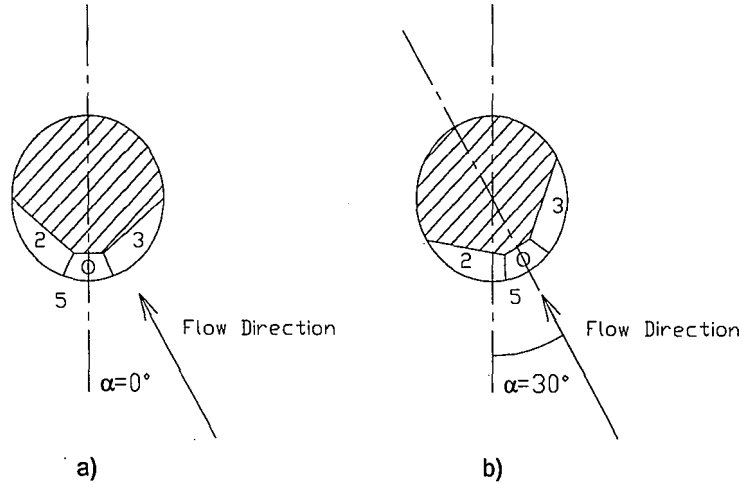

Figure A.4 Orientation of Prism Probe in the Flow

The pitch angle is determined by the differences in pressures measured from ports 4 and 5. Since the probe cannot be rotated into the direction of the flow on the pitch plane, a calibration curve is used. The calibration curves for the Prism probe used in the experiments are duplicated in Figures A.5 from Reference [32].

The pitch angle is found using Figure A5 (a). The pitch pressure differential coefficient $(P_4 - P_5)/(P_1 - P_2)$, is located on the y-axis, while the pitch angle can be read along the x-axis. Once the pitch angle is determined, the velocity pressure coefficient *VPC* can be determined from Figure A.5 (b). The dynamic pressure is multiplied by the *VPC*. This adjusted dynamic pressure accounts for the effect of the pitch angle on the dynamic pressure, Equation A.4.

$$P_{DYN} = VPC \cdot (P_1 - P_2) = \frac{1}{2} \rho V_T^2$$
$$V_T = \sqrt{\frac{2 \cdot VPC \cdot (P_1 - P_2)}{\rho}} \qquad \text{(A.12)}$$

Where P_{DYN} is the dynamic pressure [Pa], P_1 is the total pressure [Pa], P_2 is the static pressure [Pa], and V_T is the resultant velocity [m/s]. In order to process the data, the procedure was automated by curve fitting the calibration curves using cubic splines and programming the resulting equations onto a spreadsheet.

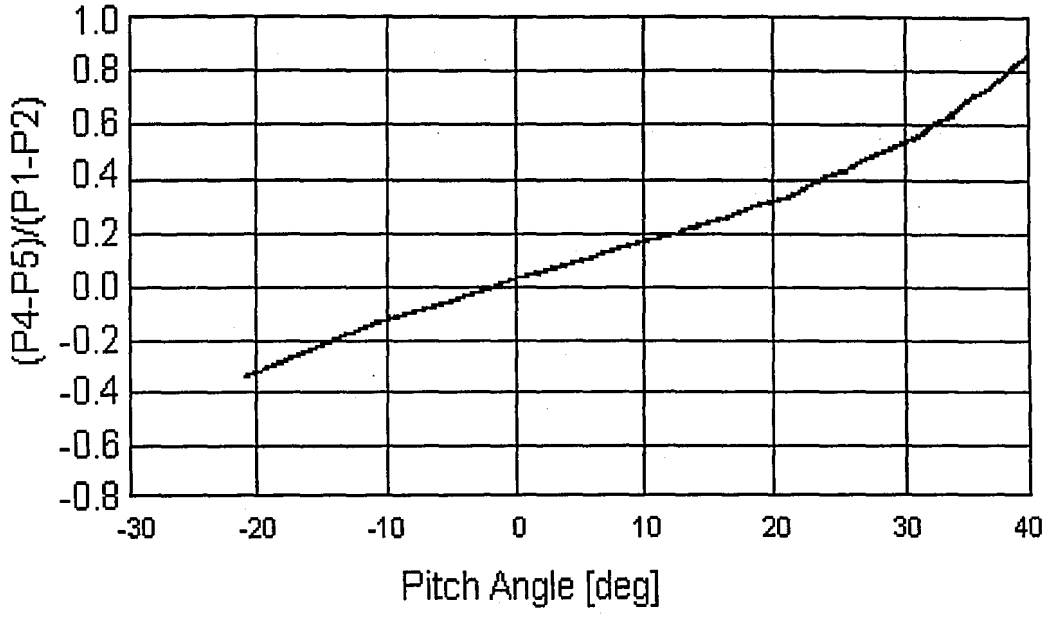

Figure A.5 (a) Pitch Angle Calibration Curve for DA-125-24-F-22-CD Probe

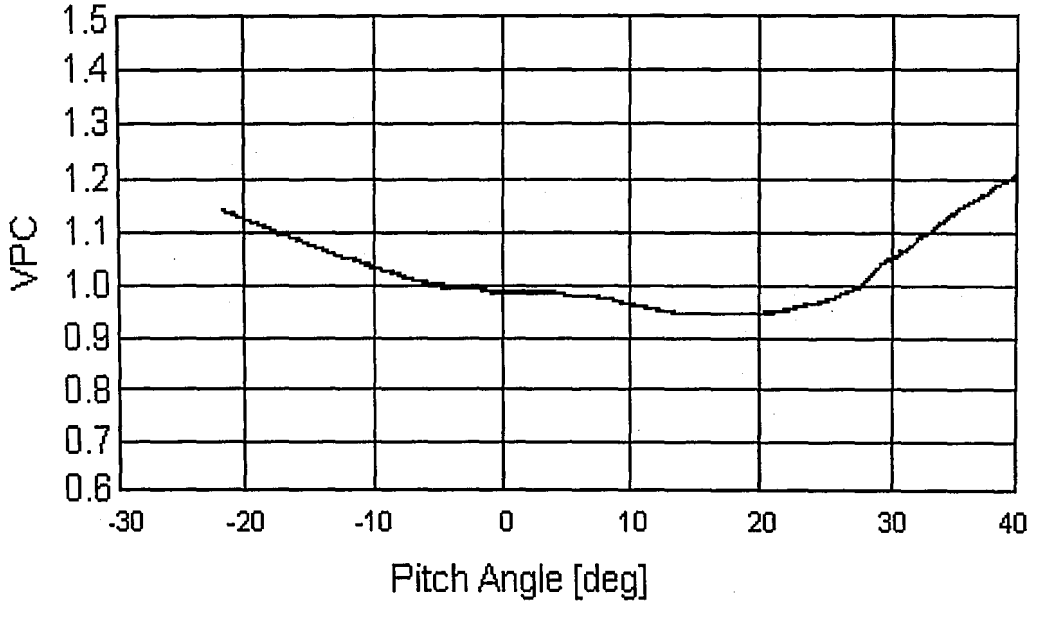

Figure A.5 (b) Velocity Pressure Coefficient Calibration Curve for DA-125-24-F-22-CD Probe

Appendix B-Flow Conditioners in Power Plant Stacks

There are a number of techniques available for the improvement of flow conditions in fluid systems. The term *flow straightener* describes a device which removes swirl, and the term *flow conditioner* refers to a device which removes swirl and also produces a redistribution of the velocity profile to some acceptable form. Ideally the redistribution would result in conditions close to those pertaining to fully developed turbulent flow. Depending on their operating principle, flow conditioners can be classified into two categories [Laws, Quazzane; 1995]:

- Turbulent Mixing Devices
- Vortex Action Devices

Turbulent mixing devices include perforated plates and tube bundles. Swirl and asymmetry in the flow are destroyed in the turbulent mixing zone within 1 and 2 diameters downstream of the device. The individual jets formed by the holes in the plate, or individual tubes in the bundle cause localized peaks in both turbulence and velocity which then decay rapidly. Vortex action devices include the honeycomb and etoile devices and the Vortab^{TM} flow conditioner [Smith et al; 1990]. In these devices swirl is removed and flow distortions are attenuated largely as a result of vortex action induced within the cellular passages of these devices.

All flowmeters are affected to some extent by the quality of the flow approaching the meter. For flow metering application in large stacks, it is desirable to improve flow conditions in order to decrease the error associated with velocity measurements. In power plants, the size and flow conditions in the chimneys require that any flow-conditioning scheme satisfy the following criteria:

- Low pressure drop
- Structural soundness and low installation cost
- Ability to withstand a corrosive environment
- No susceptibility to fouling
- Length equivalent to a few stack diameters

Most of the devices reported in the literature were designed for optimal swirl removal and profile restoration. In general, they provide more flow conditioning than is necessary for the stack, and as a consequence are too long and produce too great a pressure drop [Levy et al; 1997].

Reports of flow conditioning applications in different stack installations confirm that by placing strategically located passive swirl removal tabs, it is possible to remove swirl by a process of cross-stream vorticity cancellation [Smith et al; 1990, Eldredge et al; 1998]. Therefore, for power plant applications the flow conditioning technique of choice is what is known as an open Etoile flow straightener [Laws, 1995] or a single stage Vortab^{TM} flow conditioner. The number and dimensions of the tabs vary, but a common array is shown in Figure B.1, in which the tab height is 0.225D and its length is 1.0D.

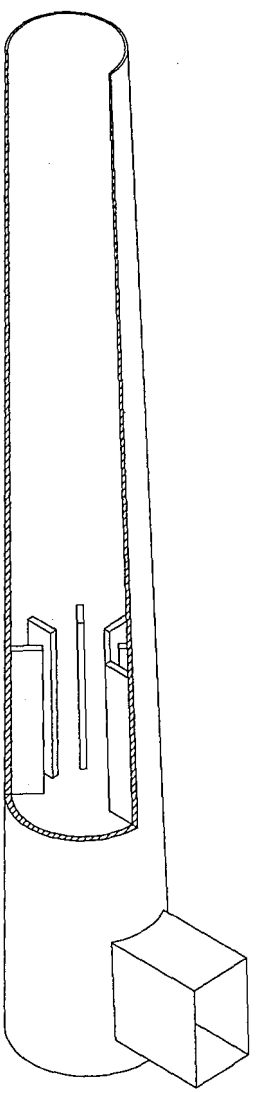

Figure B.1 Short Stack with Open Etoile Flow Conditioner.

References Appendix-B

[1] Eldredge T.V., Levy E.K. (1998), "CEM Flow Accuracy Project-Phase II," Lehigh University Energy Research Center, Draft Report, October 14, 1998.

[2] Laws E. M., Quazzane A.K. (1995), "A Preliminary Study into the effect of length on the Performance of the Etoile Flow Straightener," Flow Measurement Instruments, Vol. 6, No. 3, pp. 225-233, 1995.

[3] Laws E. M., Quazzane A.K. (1992), "Effect of Plate depth on the performance of a Zanker Flow Conditioner," Flow Measurement Instruments, Vol. 6, No. 3, pp. 225-233, 1995.

[4] Laws E. M. (1990), "Flow Conditioner-A New Development," Flow Measurement Instruments, Vol. 1, pp. 165-170, April 1990.

[5] Smith C.R., Hopper P.B., Yordy E.L. (1995),"Elimination of Cyclonic Flow in Chimneys to meet C.E.M's Criteria," Proceedings of the American Power Conference, pp.1409-1412, (1995).

Appendix C-Experimental Velocity Data

This Appendix includes experimental data obtained with the type DA prism probe at measurement planes located at 1.01, 2.44, and 3.88 diameters from the downstream corner of the inlet breaching. The coordinate system used is presented in Figure C.1, flow is in the direction out of the page, the x-axis is aligned with the inlet duct centerline.

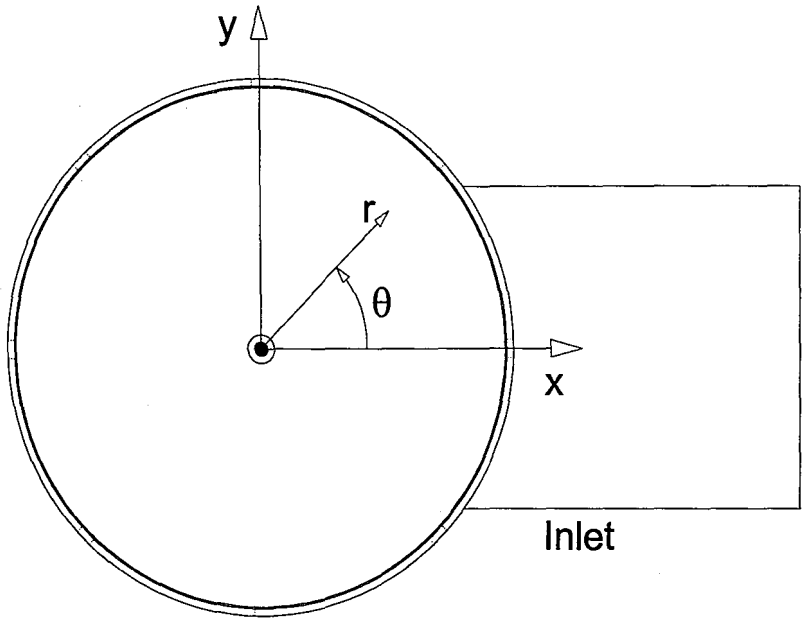

Figure C.1 Coordinate System

Station A	1.1 L/D	$V_{Z,AVG}$=37.75 m/s					
x	y	V_Z	V_r	V_θ	Yaw	Pitch	RA
0.0000	0.2286	0.0000	0.0000	0.0000	0.0000	0.0000	0.0000
0.0000	0.2228	44.3466	8.5611	-8.4617	-10.8027	10.7374	15.1861
0.0000	0.2108	48.4522	1.4498	-9.7427	-11.3693	1.6803	11.4912
0.0000	0.1979	45.9083	0.3988	-9.5449	-11.7452	0.4873	11.7551
0.0000	0.1842	40.8197	1.1640	-9.1825	-12.6777	1.5936	12.7759
0.0000	0.1697	34.6292	2.7382	-7.9076	-12.8630	4.4080	13.5853
0.0000	0.1532	29.0322	5.2567	-6.6295	-12.8630	10.0108	16.2475
0.0000	0.1354	24.3023	7.7742	-4.6371	-10.8027	17.4442	20.4294
0.0000	0.1143	20.9042	10.5643	-1.0940	-2.9959	26.7789	26.9337
0.0000	0.0886	20.2676	11.9193	4.9032	13.5998	29.7526	32.4528
0.0000	0.0513	24.9124	13.5945	11.6957	25.1487	26.2877	35.7482
0.0000	-0.0513	31.9125	-2.6548	-9.8615	-17.1720	-4.5444	17.7457
0.0000	-0.0886	30.9986	2.0851	1.0818	1.9988	3.8458	4.3335
0.0000	-0.1143	34.5690	3.2558	8.9471	14.5108	5.2098	15.3988
0.0000	-0.1354	38.0135	2.6045	13.0014	18.8817	3.7092	19.2296
0.0000	-0.1532	42.6544	1.2644	14.8682	19.2172	1.6033	19.2814
0.0000	-0.1697	46.4332	0.5617	15.8811	18.8818	0.6558	18.8927
0.0000	-0.1842	50.6148	0.0195	16.9789	18.5442	0.0210	18.5442
0.0000	-0.1979	52.8980	-0.4068	17.3965	18.2044	-0.4186	18.2090
0.0000	-0.2108	53.2913	0.5799	17.5258	18.2044	0.5922	18.2137
0.0000	-0.2228	50.7914	6.2291	16.5361	18.0337	6.6516	19.1829
0.0000	-0.2286	0.0000	0.0000	0.0000	0.0000	0.0000	0.0000
x	y	V_Z	V_r	V_θ	Yaw	Pitch	RA
0.2286	0.0000	0.0000	0.0000	0.0000	0.0000	0.0000	0.0000
0.2228	0.0000	26.1844	7.3062	-13.0922	-26.5651	14.0130	29.7949
0.2108	0.0000	28.8483	-3.6953	-13.5434	-25.1487	-6.6140	25.9491
0.1979	0.0000	27.9160	-7.7119	-10.4575	-20.5363	-14.5042	24.9597
0.1842	0.0000	27.7400	-10.2491	-6.7109	-13.5998	-19.7538	23.8276
0.1697	0.0000	26.5191	-12.8316	-1.3879	-2.9959	-25.7899	25.9515
0.1532	0.0000	27.7750	-14.3796	1.1631	2.3979	-27.3509	27.4478
0.1354	0.0000	27.9693	-16.2201	6.2917	12.6777	-29.5006	31.8827
0.1143	0.0000	28.8402	-18.2483	8.9121	17.1720	-31.1543	35.1519
0.0886	0.0000	29.8144	-19.7043	10.6845	19.7161	-31.8879	36.9361
0.0513	0.0000	28.9162	-20.7365	11.2984	21.3421	-33.7408	39.2372
-0.0513	0.0000	27.8085	9.6185	0.1941	0.4000	19.0792	19.0832
-0.0886	0.0000	36.8958	3.0454	3.7286	5.7705	4.6947	7.4340
-0.1143	0.0000	45.1490	1.6456	5.1893	6.5567	2.0737	6.8754
-0.1354	0.0000	50.8444	1.6897	6.3725	7.1438	1.8887	7.3880
-0.1532	0.0000	53.9602	1.5168	6.9499	7.3391	1.5970	7.5099
-0.1697	0.0000	54.9732	1.7722	7.0803	7.3391	1.8313	7.5629
-0.1842	0.0000	54.7383	1.3947	7.2395	7.5340	1.4469	7.6709
-0.1979	0.0000	52.9005	1.4574	7.1795	7.7287	1.5637	7.8844
-0.2108	0.0000	50.6377	2.8009	6.6972	7.5340	3.1386	8.1582
-0.2228	0.0000	41.8369	10.0876	4.8086	6.5567	13.4708	14.9552
-0.2286	0.0000	0.0000	0.0000	0.0000	0.0000	0.0000	0.0000

Station A	1.1 L/D	$V_{Z,AVG}$=37.75 m/s					
x	y	V_Z	V_r	V_θ	Yaw	Pitch	RA
-0.1616	0.1616	0.0000	0.0000	0.0000	0.0000	0.0000	0.0000
-0.1575	0.1575	44.8709	7.6236	2.6611	3.3940	9.6259	10.2014
-0.1491	0.1491	51.2849	1.0146	2.6841	2.9959	1.1318	3.2024
-0.1399	0.1399	53.0995	-0.7168	2.5939	2.7967	-0.7724	2.9013
-0.1302	0.1302	53.1868	-0.7690	2.4127	2.5973	-0.8275	2.7259
-0.1200	0.1200	50.4143	-0.5100	1.9353	2.1984	-0.5792	2.2734
-0.1083	0.1083	46.7129	-0.1329	1.3043	1.5994	-0.1629	1.6077
-0.0957	0.0957	41.9305	0.5143	1.0245	1.3996	0.7025	1.5660
-0.0808	0.0808	35.8729	2.5693	0.5009	0.7999	4.0963	4.1736
-0.0627	0.0627	30.2113	6.3855	1.0544	1.9988	11.9274	12.0914
-0.0363	0.0363	25.4539	11.8367	4.4200	9.8511	24.6158	26.3993
0.0363	-0.0363	37.2155	-19.3274	-7.7376	-11.7451	-26.9516	29.2230
0.0627	-0.0627	30.7829	-18.9533	-2.6829	-4.9811	-31.5243	31.8753
0.0808	-0.0808	30.9491	-17.1902	1.1881	2.1984	-29.0314	29.1073
0.0957	-0.0957	32.3669	-14.9571	4.5046	7.9231	-24.5936	25.7626
0.1083	-0.1083	33.7781	-12.7976	7.3685	12.3059	-20.3129	23.6142
0.1200	-0.1200	36.1721	-10.3402	9.9704	15.4102	-15.4074	21.6583
0.1302	-0.1302	37.9434	-8.0524	11.8511	17.3454	-11.4515	20.6872
0.1399	-0.1399	39.6862	-5.4958	13.8335	19.2172	-7.4500	20.5597
0.1491	-0.1491	39.4527	-1.6560	13.1696	18.4594	-2.2800	18.5948
0.1575	-0.1575	36.1347	6.5310	11.1662	17.1721	9.7974	19.6970
0.1616	-0.1616	0.0000	0.0000	0.0000	0.0000	0.0000	0.0000
x	y	V_Z	V_r	V_θ	Yaw	Pitch	RA
0.1616	0.1616	0.0000	0.0000	0.0000	0.0000	0.0000	0.0000
0.1575	0.1575	36.0643	7.1489	-19.6421	-28.5745	9.8752	30.0962
0.1491	0.1491	38.0448	-0.3881	-20.4974	-28.3145	-0.5145	28.3188
0.1399	0.1399	35.1477	-1.5581	-18.8331	-28.1836	-2.2376	28.2650
0.1302	0.1302	29.4535	-0.7842	-15.6080	-27.9200	-1.3477	27.9499
0.1200	0.1200	24.5281	0.4271	-12.2640	-26.5651	0.8924	26.5790
0.1083	0.1083	19.4870	1.7543	-7.3000	-20.5363	4.8189	21.0703
0.0957	0.0957	16.8868	2.8992	0.0000	0.0000	9.7417	9.7417
0.0808	0.0808	19.1219	1.7470	7.1632	20.5363	4.8899	21.0859
0.0627	0.0627	24.6102	-0.1568	13.7619	29.2136	-0.3187	29.2152
0.0363	0.0363	31.1617	-2.8727	19.1851	31.6190	-4.4886	31.9033
-0.0363	-0.0363	28.4883	8.9246	3.1756	6.3604	17.2936	18.3926
-0.0627	-0.0627	35.6622	5.5073	6.1927	9.8511	8.6514	13.0824
-0.0808	-0.0808	43.1086	3.7860	9.2570	12.1194	4.9077	13.0616
-0.0957	-0.0957	49.3047	3.1932	10.0826	11.5575	3.6306	12.1069
-0.1083	-0.1083	52.7791	3.0562	10.6128	11.3694	3.2492	11.8186
-0.1200	-0.1200	54.5849	2.5341	10.7892	11.1809	2.6076	11.4771
-0.1302	-0.1302	55.1949	2.3355	10.7208	10.9920	2.3786	11.2433
-0.1399	-0.1399	54.1596	1.8786	10.5197	10.9920	1.9501	11.1615
-0.1491	-0.1491	52.1488	2.2829	10.1291	10.9920	2.4606	11.2607
-0.1575	-0.1575	48.0764	8.4423	9.9957	11.7452	9.7553	15.2242
-0.1616	-0.1616	0.0000	0.0000	0.0000	0.0000	0.0000	0.0000

Station A	1.1 L/D	$V_{Z,AVG}$=37.75 m/s					
x	y	V_Z	V_r	V_θ	Yaw	Pitch	RA
-0.0875	0.2112	0.0000	0.0000	0.0000	0.0000	0.0000	0.0000
-0.0852	0.2058	47.8016	7.6888	1.6683	1.9988	9.1322	9.3466
-0.0807	0.1948	52.0518	2.0362	1.4534	1.5994	2.2393	2.7516
-0.0757	0.1828	51.8012	1.1536	1.0848	1.1997	1.2754	1.7510
-0.0705	0.1701	48.4494	1.6014	0.8456	0.9999	1.8928	2.1406
-0.0649	0.1568	44.0373	2.0167	0.0000	0.0000	2.6221	2.6221
-0.0586	0.1415	39.0774	3.2414	-1.0229	-1.4995	4.7401	4.9711
-0.0518	0.1251	33.4857	5.3835	-1.2854	-2.1984	9.1267	9.3855
-0.0437	0.1056	28.3611	8.2865	-0.9898	-1.9988	16.2779	16.3969
-0.0339	0.0819	23.6410	12.0855	1.6491	3.9903	27.0201	27.2912
-0.0196	0.0474	23.6011	13.2717	7.2932	17.1720	28.2477	32.6862
0.0196	-0.0474	32.3906	-14.8262	-12.1337	-20.5363	-23.2021	30.6035
0.0339	-0.0819	31.7898	-11.6912	-6.0658	-10.8027	-19.8622	22.5051
0.0437	-0.1056	31.4575	-8.6631	1.6464	2.9959	-15.3770	15.6592
0.0518	-0.1251	33.8343	-6.3923	6.5718	10.9919	-10.5069	15.1610
0.0586	-0.1415	35.4619	-4.9442	10.3681	16.2974	-7.6220	17.9478
0.0649	-0.1568	39.2331	-3.9573	12.2539	17.3454	-5.4995	18.1708
0.0705	-0.1701	42.7259	-3.0807	13.3448	17.3454	-3.9371	17.7732
0.0757	-0.1828	45.4467	-2.1344	14.0438	17.1721	-2.5693	17.3575
0.0807	-0.1948	46.0330	0.7618	14.2250	17.1721	0.9058	17.1952
0.0852	-0.2058	40.0992	7.2372	13.0550	18.0336	9.7380	20.4177
0.0875	-0.2112	0.0000	0.0000	0.0000	0.0000	0.0000	0.0000
x	y	V_Z	V_r	V_θ	Yaw	Pitch	RA
0.2112	0.0875	0.0000	0.0000	0.0000	0.0000	0.0000	0.0000
0.2058	0.0852	35.1655	-0.0556	-22.6040	-32.7324	-0.0762	32.7325
0.1948	0.0807	35.2603	-0.5299	-21.7084	-31.6190	-0.7332	31.6266
0.1828	0.0757	32.5622	-1.7514	-19.8226	-31.3315	-2.6305	31.4305
0.1701	0.0705	27.7038	-1.9161	-16.2839	-30.4464	-3.4124	30.6188
0.1568	0.0649	23.5748	-2.1967	-12.1419	-27.2502	-4.7354	27.6275
0.1415	0.0586	20.3162	-2.6441	-6.6143	-18.0336	-7.0548	19.3216
0.1251	0.0518	19.1983	-5.2175	1.3392	3.9903	-15.1687	15.6729
0.1056	0.0437	22.2222	-7.5943	7.6005	18.8817	-17.9187	25.8034
0.0819	0.0339	25.7178	-9.7438	13.2457	27.2502	-18.6147	32.5941
0.0474	0.0196	30.0852	-12.3592	17.0837	29.5898	-19.6582	35.0252
-0.0474	-0.0196	29.6207	9.4577	-1.3437	-2.5973	17.6909	17.8745
-0.0819	-0.0339	37.5371	3.8613	5.8721	8.8910	5.8031	10.6045
-0.1056	-0.0437	45.4057	2.0864	7.7285	9.6597	2.5937	9.9987
-0.1251	-0.0518	51.2691	1.9237	8.5501	9.4680	2.1196	9.7003
-0.1415	-0.0586	54.2528	1.7747	8.8609	9.2760	1.8491	9.4570
-0.1568	-0.0649	55.5412	1.6074	9.0714	9.2760	1.6361	9.4180
-0.1701	-0.0705	55.6837	1.1691	9.0946	9.2760	1.1871	9.3510
-0.1828	-0.0757	54.1104	1.0750	8.6513	9.0837	1.1239	9.1524
-0.1948	-0.0807	51.3214	2.2567	8.3822	9.2760	2.4849	9.6003
-0.2058	-0.0852	46.2040	8.9377	7.3872	9.0837	10.8141	14.0881
-0.2112	-0.0875	0.0000	0.0000	0.0000	0.0000	0.0000	0.0000

Station A	1.1 L/D	$V_{Z,AVG}$=37.75 m/s					
x	y	V_Z	V_r	V_θ	Yaw	Pitch	RA
0.087481	0.211199	0	0	0	0	0	0
0.085246	0.205802	44.2853	4.346809	-15.0011	-18.7132	5.311285	19.42637
0.080677	0.194772	45.28989	-0.3136	-15.4901	-18.8818	-0.37538	18.88536
0.07572	0.182804	41.29998	-0.74399	-14.5311	-19.384	-0.97354	19.40752
0.070471	0.170132	36.247	0.579292	-13.5784	-20.5363	0.857434	20.55342
0.064931	0.156756	30.50764	2.595683	-11.4284	-20.5363	4.555478	21.01416
0.058613	0.141503	25.43739	5.078147	-8.7001	-18.8817	10.69661	21.60452
0.051808	0.125077	20.91288	7.740449	-4.70437	-12.6777	19.85489	23.41868
0.043741	0.105599	18.41686	10.74006	0.963864	2.995896	30.21513	30.34932
0.033923	0.081898	19.8114	10.56462	7.421484	20.53628	26.53622	33.09177
0.019635	0.047402	26.6306	8.957784	15.27469	29.83758	16.2663	33.62125
-0.01963	-0.0474	31.5042	5.119697	-6.87243	-12.3059	9.021803	15.21746
-0.03392	-0.0819	33.75414	6.297191	6.440598	10.80271	10.38448	14.94163
-0.04374	-0.1056	38.8032	4.845163	12.24821	17.51827	6.790461	18.74975
-0.05181	-0.12508	44.81925	3.397615	14.29555	17.6906	4.130857	18.15146
-0.05861	-0.1415	49.25191	2.552135	15.38314	17.34546	2.83163	17.56806
-0.06493	-0.15676	52.44886	2.03954	16.03344	16.99821	2.129704	17.1272
-0.07047	-0.17013	54.61499	1.522859	16.33219	16.64889	1.53027	16.71708
-0.07572	-0.1828	54.69019	1.302472	16.17241	16.47345	1.308286	16.52388
-0.08068	-0.19477	53.02616	1.189206	15.85705	16.64888	1.230903	16.69303
-0.08525	-0.2058	46.86974	10.73231	13.8598	16.47342	12.38459	20.50582
-0.08748	-0.2112	0	0	0	0	0	0
x	y	V_Z	V_r	V_θ	Yaw	Pitch	RA
0.211199	-0.08748	0	0	0	0	0	0
0.205802	-0.08525	31.65528	3.431941	-4.07706	-7.33905	6.137312	9.556244
0.194772	-0.08068	32.50459	-4.04469	-4.29894	-7.53401	-7.03249	10.29231
0.182804	-0.07572	33.4822	-8.07884	-3.03458	-5.17872	-13.5121	14.45329
0.170132	-0.07047	34.18078	-11.5012	-0.35793	-0.59997	-18.5961	18.60547
0.156756	-0.06493	33.88182	-14.434	1.182459	1.998784	-23.0619	23.14363
0.141503	-0.05861	33.70524	-16.9316	2.937607	4.981073	-26.5855	27.01465
0.125077	-0.05181	33.91638	-19.448	3.54523	5.967374	-29.6962	30.23614
0.105599	-0.04374	33.22874	-21.4248	4.394717	7.534014	-32.5867	33.35257
0.081898	-0.03392	31.41444	-22.7645	4.805968	8.698009	-35.6146	36.5245
0.047402	-0.01963	28.57334	-24.0092	4.371319	8.698008	-39.7131	40.49998
-0.0474	0.019635	27.13439	13.39781	2.647854	5.573445	26.17057	26.71647
-0.0819	0.033923	33.47674	6.367269	3.150442	5.376179	10.72274	11.98091
-0.1056	0.043741	40.60252	3.444929	3.82104	5.376183	4.828424	7.221394
-0.12508	0.051808	47.33515	2.69872	4.454644	5.37619	3.24875	6.279076
-0.1415	0.058613	51.328	2.789113	5.721499	6.360467	3.091229	7.069083
-0.15676	0.064931	54.3951	2.490346	6.252048	6.556674	2.604195	7.052813
-0.17013	0.070471	55.36539	2.418329	6.747379	6.948371	2.482711	7.376548
-0.1828	0.07572	55.09047	1.961791	7.000084	7.241496	2.023207	7.517368
-0.19477	0.080677	53.22795	2.533847	6.671261	7.143846	2.704307	7.63609
-0.2058	0.085246	49.3759	6.908463	6.017429	6.948359	7.907117	10.51166
-0.2112	0.087481	0	0	0	0	0	0

Station B	2.44 L/D	$V_{Z,AVG}$=36.97 m/s					
x	y	V_Z	V_r	V_θ	Yaw	Pitch	RA
0.0875	0.2112	0.0000	0.0000	0.0000	0.0000	0.0000	0.0000
0.0852	0.2058	31.6159	2.9860	-3.8530	-6.9483	5.3559	8.7650
0.0807	0.1948	34.5617	0.8536	-4.0922	-6.7526	1.4050	6.8966
0.0757	0.1828	36.2638	-0.4228	-4.1052	-6.4586	-0.6637	6.4925
0.0705	0.1701	36.0154	-0.5418	-3.7646	-5.9674	-0.8573	6.0284
0.0649	0.1568	34.8466	-0.4414	-3.0371	-4.9811	-0.7229	5.0331
0.0586	0.1415	33.2592	0.0205	-1.5087	-2.5973	0.0353	2.5976
0.0518	0.1251	31.6835	0.8733	0.0000	0.0000	1.5788	1.5788
0.0437	0.1056	30.4592	1.9765	1.8064	3.3940	3.7063	5.0240
0.0339	0.0819	30.2425	3.4724	3.2662	6.1640	6.5125	8.9579
0.0196	0.0474	31.2690	4.7327	5.1609	9.3720	8.4934	12.6225
-0.0196	-0.0474	38.4901	-6.6327	2.6849	3.9903	-9.7541	10.5314
-0.0339	-0.0819	41.7686	-6.7831	5.0903	6.9483	-9.1576	11.4773
-0.0437	-0.1056	43.8438	-4.0239	7.2363	9.3721	-5.1741	10.6943
-0.0518	-0.1251	45.8919	-3.2711	8.4419	10.4231	-4.0100	11.1599
-0.0586	-0.1415	47.9360	-2.5011	8.8179	10.4231	-2.9376	10.8248
-0.0649	-0.1568	48.9042	-1.4508	9.1638	10.6131	-1.6702	10.7423
-0.0705	-0.1701	49.3440	-0.5520	9.0769	10.4231	-0.6303	10.4420
-0.0757	-0.1828	48.3434	0.5021	8.7269	10.2328	0.5856	10.2494
-0.0807	-0.1948	44.6984	3.0204	7.3004	9.2760	3.8154	10.0237
-0.0852	-0.2058	36.5106	6.8295	5.3336	8.3112	10.4863	13.3515
-0.0875	-0.2112	0.0000	0.0000	0.0000	0.0000	0.0000	0.0000
x	y	V_Z	V_r	V_θ	Yaw	Pitch	RA
0.2112	-0.0875	0.0000	0.0000	0.0000	0.0000	0.0000	0.0000
0.2058	-0.0852	22.6260	2.9249	-4.8972	-12.2127	7.2009	14.1497
0.1948	-0.0807	26.0766	0.3963	-4.5282	-9.8511	0.8578	9.8880
0.1828	-0.0757	27.9517	-0.8725	-3.4065	-6.9483	-1.7747	7.1703
0.1701	-0.0705	28.2163	-1.8795	-1.0832	-2.1984	-3.8080	4.3962
0.1568	-0.0649	28.7397	-2.4706	0.5016	0.9998	-4.9125	5.0130
0.1415	-0.0586	28.6206	-3.3510	2.4944	4.9811	-6.6531	8.3044
0.1251	-0.0518	29.5177	-3.4554	3.5973	6.9483	-6.6282	9.5915
0.1056	-0.0437	30.3497	-4.0174	4.7477	8.8910	-7.4509	11.5809
0.0819	-0.0339	31.8456	-4.0529	6.0764	10.8027	-7.1257	12.9178
0.0474	-0.0196	33.5230	-4.7954	7.5410	12.6777	-7.9449	14.9269
-0.0474	0.0196	34.8152	3.2986	1.2150	1.9988	5.4091	5.7655
-0.0819	0.0339	36.8086	1.2288	3.5919	5.5734	1.9030	5.8884
-0.1056	0.0437	39.9736	0.4596	4.5945	6.5567	0.6544	6.5891
-0.1251	0.0518	43.5809	-0.0163	5.1602	6.7526	-0.0213	6.7527
-0.1415	0.0586	46.5783	-0.1825	5.5151	6.7526	-0.2229	6.7563
-0.1568	0.0649	48.9928	0.0228	5.8010	6.7526	0.0265	6.7527
-0.1701	0.0705	50.1027	0.4411	5.9324	6.7526	0.5009	6.7711
-0.1828	0.0757	50.0232	1.0613	6.0963	6.9484	1.2065	7.0518
-0.1948	0.0807	46.3958	3.1532	5.8150	7.1438	3.8580	8.1142
-0.2058	0.0852	38.1440	8.1987	5.9670	8.8910	11.9891	14.8872
-0.2112	0.0875	0.0000	0.0000	0.0000	0.0000	0.0000	0.0000

Station B	2.44 L/D	$V_{Z,AVG}$=36.97 m/s					
x	y	V_Z	V_r	V_θ	Yaw	Pitch	RA
0.0000	0.2286	0.0000	0.0000	0.0000	0.0000	0.0000	0.0000
0.0000	0.2228	31.2379	3.8146	-1.0902	-1.9988	6.9580	7.2381
0.0000	0.2108	35.7547	1.9397	-2.1205	-3.3940	3.0998	4.5953
0.0000	0.1979	38.2397	0.7470	-2.9337	-4.3871	1.1158	4.5265
0.0000	0.1842	38.2381	0.1691	-2.6674	-3.9903	0.2528	3.9983
0.0000	0.1697	36.9252	0.1620	-1.9325	-2.9959	0.2510	3.0064
0.0000	0.1532	35.2599	0.5559	-0.9845	-1.5994	0.9029	1.8366
0.0000	0.1354	33.3200	1.2457	0.1163	0.2000	2.1411	2.1504
0.0000	0.1143	32.1748	2.2353	1.1229	1.9988	3.9717	4.4456
0.0000	0.0886	31.0581	3.7985	2.2746	4.1888	6.9544	8.1132
0.0000	0.0513	31.8472	5.1127	2.7757	4.9811	9.0865	10.3521
0.0000	-0.0513	37.8524	-5.8607	3.6938	5.5734	-8.7603	10.3713
0.0000	-0.0886	40.7660	-4.2975	5.6735	7.9231	-5.9609	9.9036
0.0000	-0.1143	42.8420	-3.1352	7.2921	9.6597	-4.1264	10.4964
0.0000	-0.1354	44.9981	-2.3262	7.8139	9.8511	-2.9157	10.2695
0.0000	-0.1532	45.6271	-1.3735	8.7061	10.8027	-1.6937	10.9331
0.0000	-0.1697	46.7233	-0.3915	8.4345	10.2328	-0.4725	10.2436
0.0000	-0.1842	46.7971	0.5105	8.1262	9.8511	0.6158	9.8701
0.0000	-0.1979	45.2940	1.8445	7.2417	9.0837	2.3027	9.3686
0.0000	-0.2108	41.2200	3.9856	6.4482	8.8910	5.4569	10.4205
0.0000	-0.2228	32.8557	6.3188	3.4344	5.9674	10.8286	12.3468
0.0000	-0.2286	0.0000	0.0000	0.0000	0.0000	0.0000	0.0000
x	y	V_Z	V_r	V_θ	Yaw	Pitch	RA
0.2286	0.0000	0.0000	0.0000	0.0000	0.0000	0.0000	0.0000
0.2228	0.0000	23.9440	3.3781	-8.5808	-19.7161	7.5652	21.0636
0.2108	0.0000	26.9416	1.1771	-7.8770	-16.2974	2.4014	16.4687
0.1979	0.0000	27.7612	0.0779	-6.0559	-12.3059	0.1571	12.3069
0.1842	0.0000	28.3747	-0.7832	-4.4388	-8.8910	-1.5621	9.0261
0.1697	0.0000	28.4357	-1.6644	-1.9836	-3.9903	-3.3417	5.2030
0.1532	0.0000	28.1046	-2.1584	0.4905	0.9998	-4.3910	4.5032
0.1354	0.0000	28.9568	-2.8268	2.0199	3.9903	-5.5622	6.8418
0.1143	0.0000	29.6147	-2.8442	3.6091	6.9483	-5.4458	8.8199
0.0886	0.0000	30.9885	-2.8063	5.3811	9.8511	-5.0986	11.0808
0.0513	0.0000	33.5421	-3.0234	6.6299	11.1808	-5.0533	12.2565
-0.0513	0.0000	35.3862	-2.1173	0.6176	0.9998	-3.4237	3.5665
-0.0886	0.0000	38.2408	-3.1926	3.3329	4.9811	-4.7544	6.8817
-0.1143	0.0000	41.8537	-3.6566	4.3749	5.9674	-4.9661	7.7578
-0.1354	0.0000	45.2686	-3.6254	5.5169	6.9484	-4.5454	8.2969
-0.1532	0.0000	48.2384	-3.4607	5.7116	6.7526	-4.0751	7.8821
-0.1697	0.0000	50.5622	-3.3291	5.8991	6.6547	-3.7418	7.6304
-0.1842	0.0000	51.1305	-2.8459	6.0541	6.7526	-3.1637	7.4539
-0.1979	0.0000	49.7318	-0.7508	6.0608	6.9484	-0.8586	7.0009
-0.2108	0.0000	45.4960	2.7483	5.7022	7.1438	3.4301	7.9208
-0.2228	0.0000	34.4917	6.4073	4.2035	6.9483	10.4480	12.5261
-0.2286	0.0000	0.0000	0.0000	0.0000	0.0000	0.0000	0.0000

Station B	2.44 L/D	$V_{Z,AVG}$=36.97 m/s					
x	y	V_Z	V_r	V_θ	Yaw	Pitch	RA
-0.0875	0.2112	0.0000	0.0000	0.0000	0.0000	0.0000	0.0000
-0.0852	0.2058	35.0875	3.5443	1.9586	3.1950	5.7592	6.5835
-0.0807	0.1948	40.3579	1.1510	1.4085	1.9988	1.6326	2.5806
-0.0757	0.1828	42.6595	-0.3923	1.1167	1.4995	-0.5266	1.5893
-0.0705	0.1701	42.9096	-0.9100	1.1981	1.5994	-1.2145	2.0081
-0.0649	0.1568	41.5155	-1.0210	1.4489	1.9988	-1.4079	2.4447
-0.0586	0.1415	39.3170	-0.7009	1.7150	2.4976	-1.0203	2.6979
-0.0518	0.1251	36.9372	-0.0079	2.1906	3.3940	-0.0123	3.3941
-0.0437	0.1056	34.4738	1.1419	2.2847	3.7917	1.8931	4.2374
-0.0339	0.0819	32.8113	2.8844	2.2888	3.9903	5.0118	6.4031
-0.0196	0.0474	32.3841	5.2277	2.1462	3.7917	9.1504	9.8987
0.0196	-0.0474	36.8009	-7.9820	4.7398	7.3390	-12.1404	14.1578
0.0339	-0.0819	37.9182	-5.5479	5.4082	8.1173	-8.2417	11.5482
0.0437	-0.1056	38.7317	-5.2520	5.9254	8.6980	-7.6344	11.5538
0.0518	-0.1251	39.2420	-4.0828	6.2741	9.0837	-5.8658	10.7996
0.0586	-0.1415	39.2212	-2.8223	6.5409	9.4680	-4.0599	10.2945
0.0649	-0.1568	39.3288	-1.9890	6.2879	9.0837	-2.8589	9.5193
0.0705	-0.1701	38.6279	-1.1261	6.0427	8.8910	-1.6497	9.0415
0.0757	-0.1828	36.9257	-0.0156	5.1391	7.9231	-0.0239	7.9232
0.0807	-0.1948	34.0030	1.4066	3.9082	6.5566	2.3534	6.9645
0.0852	-0.2058	28.8827	5.9408	2.0148	3.9903	11.5954	12.2539
0.0875	-0.2112	0.0000	0.0000	0.0000	0.0000	0.0000	0.0000
x	y	V_Z	V_r	V_θ	Yaw	Pitch	RA
0.2112	0.0875	0.0000	0.0000	0.0000	0.0000	0.0000	0.0000
0.2058	0.0852	25.9725	4.1847	-8.9683	-19.0497	8.6595	20.8588
0.1948	0.0807	29.4925	1.8004	-9.7963	-18.3745	3.3157	18.6611
0.1828	0.0757	30.3591	1.0915	-9.3815	-17.1720	1.9673	17.2810
0.1701	0.0705	29.7880	0.6066	-7.5086	-14.1478	1.1312	14.1920
0.1568	0.0649	29.1831	0.1293	-6.0675	-11.7451	0.2485	11.7477
0.1415	0.0586	28.0792	0.1854	-3.2273	-6.5566	0.3758	6.5674
0.1251	0.0518	27.2790	0.3813	-0.9520	-1.9988	0.8003	2.1530
0.1056	0.0437	27.6302	0.7198	1.7349	3.5929	1.4894	3.8890
0.0819	0.0339	28.9570	1.1089	4.3301	8.5047	2.1690	8.7750
0.0474	0.0196	31.6322	1.2615	6.5767	11.7451	2.2360	11.9532
-0.0474	-0.0196	36.5724	-1.3117	0.7659	1.1997	-2.0536	2.3783
-0.0819	-0.0339	40.4657	-1.5150	3.6675	5.1787	-2.1353	5.6006
-0.1056	-0.0437	43.5067	-1.5007	5.9046	7.7287	-1.9576	7.9713
-0.1251	-0.0518	46.8080	-1.0641	6.5144	7.9232	-1.2899	8.0268
-0.1415	-0.0586	49.6390	-0.9024	7.0800	8.1173	-1.0310	8.1821
-0.1568	-0.0649	51.7638	-0.5363	7.2042	7.9232	-0.5879	7.9448
-0.1701	-0.0705	52.5688	-0.1951	7.3162	7.9232	-0.2106	7.9260
-0.1828	-0.0757	51.3751	0.6890	7.1501	7.9232	0.7611	7.9594
-0.1948	-0.0807	48.0970	3.4779	6.6938	7.9232	4.0966	8.9135
-0.2058	-0.0852	37.2592	7.6793	4.5408	6.9483	11.5626	13.4654
-0.2112	-0.0875	0.0000	0.0000	0.0000	0.0000	0.0000	0.0000

Station B	2.44 L/D	$V_{Z,AVG}$=36.97 m/s					
x	y	V_Z	V_r	V_θ	Yaw	Pitch	RA
-0.1616	0.1616	0.0000	0.0000	0.0000	0.0000	0.0000	0.0000
-0.1575	0.1575	36.0244	5.1611	3.0145	4.7832	8.1250	9.4203
-0.1491	0.1491	42.2156	1.0869	2.5037	3.3940	1.4722	3.6992
-0.1399	0.1399	44.7131	-0.5778	2.3401	2.9959	-0.7393	3.0857
-0.1302	0.1302	45.4057	-1.2718	2.0597	2.5973	-1.6028	3.0518
-0.1200	0.1200	44.0696	-1.5222	2.1528	2.7967	-1.9759	3.4238
-0.1083	0.1083	41.7319	-1.4020	2.3295	3.1950	-1.9211	3.7276
-0.0957	0.0957	39.1436	-0.9237	2.3897	3.4935	-1.3492	3.7447
-0.0808	0.0808	36.3313	0.0058	2.4078	3.7917	0.0092	3.7917
-0.0627	0.0627	34.8967	1.2993	1.5830	2.5973	2.1302	3.3587
-0.0363	0.0363	34.3438	3.3566	0.2398	0.4000	5.5820	5.5963
0.0363	-0.0363	36.0015	-6.3332	5.6319	8.8910	-9.8596	13.2469
0.0627	-0.0627	36.5889	-5.5318	5.7238	8.8910	-8.4955	12.2737
0.0808	-0.0808	36.0741	-4.5353	6.2642	9.8511	-7.0611	12.1000
0.0957	-0.0957	36.0234	-3.6122	6.2554	9.8511	-5.6422	11.3386
0.1083	-0.1083	36.1809	-2.7523	6.2828	9.8511	-4.2862	10.7347
0.1200	-0.1200	35.1273	-1.8760	6.0998	9.8511	-3.0120	10.2969
0.1302	-0.1302	35.3595	-1.1827	5.5314	8.8910	-1.8927	9.0886
0.1399	-0.1399	33.9693	-0.3963	4.4927	7.5340	-0.6626	7.5629
0.1491	-0.1491	31.9555	0.8128	3.0073	5.3762	1.4507	5.5679
0.1575	-0.1575	26.5606	3.8774	1.8528	3.9903	8.2856	9.1903
0.1616	-0.1616	0.0000	0.0000	0.0000	0.0000	0.0000	0.0000
x	y	V_Z	V_r	V_θ	Yaw	Pitch	RA
0.1616	0.1616	0.0000	0.0000	0.0000	0.0000	0.0000	0.0000
0.1575	0.1575	28.7797	3.0091	-8.8934	-17.1720	5.7046	18.0677
0.1491	0.1491	30.8303	1.5571	-8.1872	-14.8720	2.7947	15.1265
0.1399	0.1399	32.1444	0.8634	-8.3196	-14.5108	1.4895	14.5854
0.1302	0.1302	31.5162	0.6361	-7.0896	-12.6777	1.1280	12.7270
0.1200	0.1200	30.5938	0.6819	-5.3126	-9.8511	1.2580	9.9303
0.1083	0.1083	29.5989	0.6529	-3.6072	-6.9483	1.2543	7.0601
0.0957	0.0957	28.7076	1.0053	-1.0019	-1.9988	2.0045	2.8304
0.0808	0.0808	28.8695	1.7525	0.7053	1.3996	3.4727	3.7438
0.0627	0.0627	29.5949	2.1336	3.0935	5.9674	4.1012	7.2366
0.0363	0.0363	31.4593	2.9980	4.9213	8.8910	5.3787	10.3801
-0.0363	-0.0363	37.1271	-5.6991	2.5899	3.9903	-8.7061	9.5706
-0.0627	-0.0627	41.0392	-5.3832	5.4277	7.5340	-7.4091	10.5517
-0.0808	-0.0808	44.1257	-4.8679	7.3588	9.4680	-6.2103	11.3075
-0.0957	-0.0957	47.2360	-4.4344	8.2837	9.9467	-5.2829	11.2501
-0.1083	-0.1083	49.3934	-4.0266	8.6620	9.9467	-4.5907	10.9453
-0.1200	-0.1200	51.1684	-3.6694	8.9733	9.9467	-4.0404	10.7283
-0.1302	-0.1302	51.6555	-3.0654	8.9699	9.8511	-3.3461	10.3986
-0.1399	-0.1399	50.9176	-1.3382	8.8418	9.8511	-1.4833	9.9611
-0.1491	-0.1491	46.9314	1.8635	8.4720	10.2328	2.2377	10.4721
-0.1575	-0.1575	38.4898	5.8082	7.6736	11.2751	8.4180	14.0383
-0.1616	-0.1616	0.0000	0.0000	0.0000	0.0000	0.0000	0.0000

Station C	3.88 L/D	$V_{Z,AVG}$=37.00 m/s					
x	y	V_Z	V_r	V_θ	Yaw	Pitch	RA
0.0000	0.2286	0.0000	0.0000	0.0000	0.0000	0.0000	0.0000
0.0000	0.2228	28.6669	3.2478	0.5003	0.9998	6.4628	6.5394
0.0000	0.2108	32.3343	0.9131	0.2257	0.4000	1.6175	1.6662
0.0000	0.1979	33.7364	0.5447	0.0000	0.0000	0.9250	0.9250
0.0000	0.1842	34.5265	0.6391	0.0000	0.0000	1.0604	1.0604
0.0000	0.1697	34.2342	0.7676	0.5975	0.9998	1.2842	1.6275
0.0000	0.1532	34.6579	0.9297	0.6049	0.9998	1.5364	1.8330
0.0000	0.1354	34.7670	1.2104	0.9101	1.4995	1.9933	2.4941
0.0000	0.1143	34.7592	1.3491	1.2131	1.9988	2.2213	2.9879
0.0000	0.0886	35.0722	2.0116	1.5298	2.4976	3.2796	4.1215
0.0000	0.0513	36.4456	2.5949	1.3991	2.1984	4.0696	4.6245
0.0000	-0.0513	41.2670	-3.3116	3.0223	4.1888	-4.5759	6.2006
0.0000	-0.0886	42.7619	-2.5587	4.4698	5.9674	-3.4058	6.8678
0.0000	-0.1143	43.6131	-2.0914	5.3151	6.9483	-2.7253	7.4612
0.0000	-0.1354	43.7304	-1.5812	5.3294	6.9483	-2.0556	7.2446
0.0000	-0.1532	43.4539	-1.0758	4.9945	6.5567	-1.4089	6.7057
0.0000	-0.1697	43.0028	-0.8089	4.4950	5.9674	-1.0718	6.0625
0.0000	-0.1842	42.0146	-0.4157	3.8079	5.1787	-0.5646	5.2093
0.0000	-0.1979	40.0301	-0.1641	2.7924	3.9903	-0.2344	3.9972
0.0000	-0.2108	37.0385	0.9083	1.9384	2.9959	1.4029	3.3078
0.0000	-0.2228	32.7036	3.2230	-0.2283	-0.4000	5.6283	5.6424
0.0000	-0.2286	0.0000	0.0000	0.0000	0.0000	0.0000	0.0000
x	y	V_Z	V_r	V_θ	Yaw	Pitch	RA
0.2286	0.0000	0.0000	0.0000	0.0000	0.0000	0.0000	0.0000
0.2228	0.0000	26.5218	2.3414	0.2314	0.5000	5.0450	5.0696
0.2108	0.0000	29.7047	0.4544	1.1403	2.1984	0.8758	2.3663
0.1979	0.0000	31.1317	-0.0477	1.6293	2.9959	-0.0877	2.9972
0.1842	0.0000	32.2037	-0.0796	2.1343	3.7917	-0.1414	3.7943
0.1697	0.0000	33.0841	-0.2225	2.3078	3.9903	-0.3844	4.0087
0.1532	0.0000	33.6760	-0.3141	2.9351	4.9811	-0.5323	5.0094
0.1354	0.0000	34.2878	-0.3404	3.2863	5.4748	-0.5662	5.5039
0.1143	0.0000	35.0454	-0.3117	3.5416	5.7705	-0.5069	5.7927
0.0886	0.0000	36.2855	-0.3977	3.4148	5.3762	-0.6252	5.4123
0.0513	0.0000	37.4328	-0.5186	3.9128	5.9674	-0.7895	6.0192
-0.0513	0.0000	39.6170	-1.5317	0.6914	0.9998	-2.2138	2.4290
-0.0886	0.0000	40.6278	-2.0524	2.5510	3.5929	-2.8863	4.6075
-0.1143	0.0000	42.1505	-2.1015	3.2337	4.3871	-2.8459	5.2278
-0.1354	0.0000	43.6627	-2.0715	3.5017	4.5853	-2.7076	5.3235
-0.1532	0.0000	44.5589	-1.9693	3.5736	4.5853	-2.5225	5.2320
-0.1697	0.0000	45.1290	-1.5589	3.6193	4.5853	-1.9720	4.9905
-0.1842	0.0000	45.0420	-1.2215	3.4556	4.3871	-1.5489	4.6520
-0.1979	0.0000	43.2753	-0.7437	3.1694	4.1888	-0.9819	4.3021
-0.2108	0.0000	40.2774	0.7464	3.0900	4.3871	1.0585	4.5127
-0.2228	0.0000	33.5950	3.5346	2.3435	3.9903	5.9917	7.1948
-0.2286	0.0000	0.0000	0.0000	0.0000	0.0000	0.0000	0.0000

Station C	3.88 L/D	$V_{Z,AVG}$=37.00 m/s					
x	y	V_Z	V_r	V_θ	Yaw	Pitch	RA
-0.1616	0.1616	0.0000	0.0000	0.0000	0.0000	0.0000	0.0000
-0.1575	0.1575	32.1456	2.6864	2.6899	4.7832	4.7606	6.7446
-0.1491	0.1491	36.2186	0.0531	1.8955	2.9959	0.0839	2.9971
-0.1399	0.1399	38.2407	-0.6807	2.0014	2.9959	-1.0184	3.1641
-0.1302	0.1302	39.0637	-0.9881	2.0444	2.9959	-1.4470	3.3267
-0.1200	0.1200	39.7468	-1.3292	1.8030	2.5973	-1.9133	3.2256
-0.1083	0.1083	39.8622	-1.2791	1.8083	2.5973	-1.8360	3.1804
-0.0957	0.0957	39.4334	-1.2159	1.7888	2.5973	-1.7642	3.1395
-0.0808	0.0808	38.3702	-1.1174	1.5399	2.2982	-1.6667	2.8386
-0.0627	0.0627	38.4664	-0.6662	1.3425	1.9988	-0.9916	2.2312
-0.0363	0.0363	38.9464	-0.2853	0.4078	0.6000	-0.4197	0.7322
0.0363	-0.0363	38.9373	0.0951	5.4190	7.9231	0.1386	7.9244
0.0627	-0.0627	39.0871	0.7063	5.4399	7.9231	1.0254	7.9888
0.0808	-0.0808	38.4804	1.2187	5.4884	8.1173	1.7958	8.3123
0.0957	-0.0957	37.9288	1.3847	5.4098	8.1173	2.0698	8.3753
0.1083	-0.1083	37.3003	1.6799	5.1912	7.9231	2.5541	8.3221
0.1200	-0.1200	35.9296	1.7550	5.0004	7.9231	2.7698	8.3904
0.1302	-0.1302	34.8541	1.9091	4.2476	6.9483	3.1122	7.6104
0.1399	-0.1399	33.3632	1.9779	3.4874	5.9674	3.3743	6.8523
0.1491	-0.1491	31.1114	2.3642	1.9535	3.5929	4.3372	5.6299
0.1575	-0.1575	27.1004	3.2264	0.0000	0.0000	6.7894	6.7894
0.1616	-0.1616	0.0000	0.0000	0.0000	0.0000	0.0000	0.0000
x	y	V_Z	V_r	V_θ	Yaw	Pitch	RA
0.1616	0.1616	0.0000	0.0000	0.0000	0.0000	0.0000	0.0000
0.1575	0.1575	27.9845	1.6303	-0.9766	-1.9988	3.3322	3.8851
0.1491	0.1491	30.5959	-0.8996	-0.5340	-0.9998	-1.6839	1.9583
0.1399	0.1399	31.6751	-1.1392	0.0000	0.0000	-2.0598	2.0598
0.1302	0.1302	31.9869	-1.1410	0.5582	0.9998	-2.0426	2.2741
0.1200	0.1200	32.6536	-1.1840	0.5699	0.9998	-2.0763	2.3044
0.1083	0.1083	33.0079	-1.1475	1.1520	1.9988	-1.9898	2.8201
0.0957	0.0957	33.5195	-0.8477	1.7543	2.9959	-1.4467	3.3266
0.0808	0.0808	33.9908	-0.8554	2.3711	3.9903	-1.4381	4.2411
0.0627	0.0627	34.7758	-0.7951	3.0309	4.9811	-1.3049	5.1487
0.0363	0.0363	36.4852	-0.4782	3.8138	5.9674	-0.7469	6.0138
-0.0363	-0.0363	40.6957	-4.6424	4.2539	5.9674	-6.4730	8.7953
-0.0627	-0.0627	43.2920	-4.4003	5.5758	7.3391	-5.7565	9.3176
-0.0808	-0.0808	43.9871	-4.0896	6.8811	8.8910	-5.2482	10.3137
-0.0957	-0.0957	45.3349	-3.7750	7.0920	8.8910	-4.7030	10.0494
-0.1083	-0.1083	46.2169	-3.5083	6.9111	8.5047	-4.2934	9.5199
-0.1200	-0.1200	46.7972	-3.1656	6.5129	7.9232	-3.8331	8.7963
-0.1302	-0.1302	46.5790	-2.4657	5.9992	7.3391	-3.0054	7.9275
-0.1399	-0.1399	45.6669	-2.2825	5.5654	6.9484	-2.8403	7.5038
-0.1491	-0.1491	43.2642	-1.6032	4.8226	6.3605	-2.1091	6.6997
-0.1575	-0.1575	39.2627	1.9435	4.7849	6.9483	2.8131	7.4936
-0.1616	-0.1616	0.0000	0.0000	0.0000	0.0000	0.0000	0.0000

Station C	3.88 L/D	$V_{Z,AVG}$=37.00 m/s					
x	y	V_Z	V_r	V_θ	Yaw	Pitch	RA
-0.0875	0.2112	0.0000	0.0000	0.0000	0.0000	0.0000	0.0000
-0.0852	0.2058	29.6433	5.0100	1.5514	2.9959	9.5801	10.0334
-0.0807	0.1948	33.5443	1.9867	1.2877	2.1984	3.3869	4.0371
-0.0757	0.1828	35.7236	1.4277	1.1221	1.7991	2.2875	2.9099
-0.0705	0.1701	36.5488	1.4482	0.8930	1.3996	2.2683	2.6652
-0.0649	0.1568	37.0381	1.5124	0.7757	1.1997	2.3377	2.6275
-0.0586	0.1415	36.6150	1.6919	1.2778	1.9988	2.6440	3.3141
-0.0518	0.1251	36.4344	1.9965	1.3986	2.1984	3.1342	3.8277
-0.0437	0.1056	36.2150	2.5396	1.8953	2.9959	4.0059	5.0008
-0.0339	0.0819	36.2142	3.0337	1.8953	2.9959	4.7820	5.6411
-0.0196	0.0474	37.0229	3.8837	1.2921	1.9988	5.9847	6.3085
0.0196	-0.0474	41.9809	-3.1737	3.6589	4.9811	-4.3069	6.5813
0.0339	-0.0819	42.5132	-2.3480	4.4439	5.9674	-3.1442	6.7424
0.0437	-0.1056	42.2844	-1.5274	5.1532	6.9483	-2.0536	7.2440
0.0518	-0.1251	41.6945	-1.1008	5.3701	7.3391	-1.4999	7.4899
0.0586	-0.1415	41.1995	-0.7146	5.0210	6.9483	-0.9864	7.0177
0.0649	-0.1568	40.6839	-0.2568	4.2526	5.9674	-0.3597	5.9782
0.0705	-0.1701	39.4354	0.0695	3.7112	5.3762	0.1005	5.3771
0.0757	-0.1828	37.6377	0.3012	2.6255	3.9903	0.4574	4.0164
0.0807	-0.1948	34.0870	1.3929	1.7840	2.9959	2.3368	3.7988
0.0852	-0.2058	30.0886	3.1693	0.0000	0.0000	6.0128	6.0128
0.0875	-0.2112	0.0000	0.0000	0.0000	0.0000	0.0000	0.0000
x	y	V_Z	V_r	V_θ	Yaw	Pitch	RA
0.2112	0.0875	0.0000	0.0000	0.0000	0.0000	0.0000	0.0000
0.2058	0.0852	25.5525	3.4226	-1.3373	-2.9959	7.6187	8.1833
0.1948	0.0807	29.0855	1.0294	-1.0151	-1.9988	2.0258	2.8456
0.1828	0.0757	31.3689	0.1166	-0.7664	-1.3996	0.2129	1.4157
0.1701	0.0705	32.1633	-0.2374	0.0000	0.0000	-0.4229	0.4229
0.1568	0.0649	32.4144	-0.1957	0.5657	0.9998	-0.3458	1.0580
0.1415	0.0586	33.4798	-0.2391	1.1684	1.9988	-0.4089	2.0402
0.1251	0.0518	33.8930	-0.4590	1.7738	2.9959	-0.7749	3.0944
0.1056	0.0437	34.5829	-0.2604	2.4124	3.9903	-0.4303	4.0134
0.0819	0.0339	35.5664	-0.1903	3.3471	5.3762	-0.3053	5.3848
0.0474	0.0196	37.6834	-0.1570	4.2005	6.3604	-0.2372	6.3649
-0.0474	-0.0196	40.3650	-1.5122	2.3939	3.3940	-2.1417	4.0126
-0.0819	-0.0339	41.9750	-1.3555	4.0961	5.5735	-1.8408	5.8687
-0.1056	-0.0437	43.6267	-1.3133	4.9387	6.4586	-1.7133	6.6810
-0.1251	-0.0518	44.6264	-1.0973	5.5932	7.1438	-1.3976	7.2786
-0.1415	-0.0586	45.4081	-0.8307	5.0616	6.3605	-1.0416	6.4448
-0.1568	-0.0649	45.9023	-0.6527	4.9574	6.1640	-0.8099	6.2168
-0.1701	-0.0705	45.3004	-0.1820	4.7352	5.9674	-0.2290	5.9718
-0.1828	-0.0757	43.5594	0.5110	4.2507	5.5735	0.6690	5.6133
-0.1948	-0.0807	39.8214	2.6881	3.7475	5.3762	3.8449	6.6063
-0.2058	-0.0852	31.5541	5.9960	2.7501	4.9811	10.7195	11.8079
-0.2112	-0.0875	0.0000	0.0000	0.0000	0.0000	0.0000	0.0000

Station C	3.88 L/D	$V_{Z,AVG}$=37.00 m/s					
x	y	V_Z	V_r	V_θ	Yaw	Pitch	RA
0.0875	0.2112	0.0000	0.0000	0.0000	0.0000	0.0000	0.0000
0.0852	0.2058	28.7311	3.0829	-1.5037	-2.9959	6.1162	6.8081
0.0807	0.1948	31.4287	0.5867	-1.0968	-1.9988	1.0689	2.2665
0.0757	0.1828	33.0308	0.0651	-0.9223	-1.5994	0.1128	1.6033
0.0705	0.1701	33.7127	0.1370	-0.5884	-0.9998	0.2329	1.0266
0.0649	0.1568	34.1297	0.1689	-0.4765	-0.7999	0.2836	0.8487
0.0586	0.1415	34.1683	0.1462	0.0000	0.0000	0.2452	0.2452
0.0518	0.1251	34.5298	0.4668	0.6026	0.9998	0.7744	1.2646
0.0437	0.1056	34.5937	0.7025	1.2073	1.9988	1.1627	2.3122
0.0339	0.0819	35.5735	1.1576	1.7378	2.7967	1.8615	3.3591
0.0196	0.0474	37.1363	1.6667	2.2671	3.4935	2.5651	4.3331
-0.0196	-0.0474	41.7822	-0.9891	0.3646	0.5000	-1.3560	1.4452
-0.0339	-0.0819	43.4610	-1.3698	2.2746	2.9959	-1.8028	3.4961
-0.0437	-0.1056	44.9858	-1.2728	2.7463	3.4935	-1.6176	3.8494
-0.0518	-0.1251	45.3008	-1.5571	3.1600	3.9903	-1.9639	4.4467
-0.0586	-0.1415	45.8553	-0.9520	3.0390	3.7917	-1.1867	3.9728
-0.0649	-0.1568	45.3384	-0.5485	2.6889	3.3940	-0.6919	3.4638
-0.0705	-0.1701	44.7810	-0.1214	1.8752	2.3979	-0.1552	2.4029
-0.0757	-0.1828	42.8469	0.3149	1.4953	1.9988	0.4208	2.0426
-0.0807	-0.1948	39.3620	1.5573	0.6870	0.9998	2.2653	2.4760
-0.0852	-0.2058	33.2700	7.1992	0.5806	0.9998	12.2081	12.2483
-0.0875	-0.2112	0.0000	0.0000	0.0000	0.0000	0.0000	0.0000
x	y	V_Z	V_r	V_θ	Yaw	Pitch	RA
0.2112	-0.0875	0.0000	0.0000	0.0000	0.0000	0.0000	0.0000
0.2058	-0.0852	24.7201	3.3322	1.2938	2.9959	7.6666	8.2279
0.1948	-0.0807	29.1719	1.7396	1.6284	3.1950	3.4074	4.6697
0.1828	-0.0757	32.2763	0.7659	1.9142	3.3940	1.3569	3.6549
0.1701	-0.0705	33.9006	0.4731	2.4828	4.1888	0.7974	4.2639
0.1568	-0.0649	34.5489	0.2690	3.6113	5.9674	0.4437	5.9838
0.1415	-0.0586	35.8486	0.1720	3.9960	6.3604	0.2732	6.3663
0.1251	-0.0518	36.4231	0.1316	4.4389	6.9483	0.2055	6.9514
0.1056	-0.0437	37.6928	-0.1506	4.7242	7.1438	-0.2272	7.1474
0.0819	-0.0339	38.2532	-0.3832	4.9268	7.3390	-0.5693	7.3610
0.0474	-0.0196	39.2653	-0.9575	4.9212	7.1438	-1.3861	7.2764
-0.0474	0.0196	39.4789	1.3627	0.0000	0.0000	1.9768	1.9768
-0.0819	0.0339	39.2234	0.8930	2.0528	2.9959	1.3024	3.2665
-0.1056	0.0437	39.7424	0.5139	3.1182	4.4862	0.7385	4.5464
-0.1251	0.0518	40.7877	0.2775	3.2002	4.4862	0.3885	4.5030
-0.1415	0.0586	41.4810	0.4239	3.2546	4.4862	0.5837	4.5239
-0.1568	0.0649	41.6701	0.5023	3.1969	4.3871	0.6887	4.4407
-0.1701	0.0705	41.2402	0.7585	3.2357	4.4862	1.0505	4.6073
-0.1828	0.0757	40.5113	0.9531	2.8259	3.9903	1.3444	4.2103
-0.1948	0.0807	37.5389	2.4472	3.2717	4.9811	3.7159	6.2116
-0.2058	0.0852	30.9726	6.8322	3.7746	6.9483	12.3510	14.1448
-0.2112	0.0875	0.0000	0.0000	0.0000	0.0000	0.0000	0.0000

Vita

Francisco Dovali-Solis was born in Mexico City, Mexico on November 12, 1971 to Antonio Dovali-Ramos and Maria Eugenia Solis-Cortez. He attended the Preparatory School of the *Instituto Tecnologico y de Estudios Superiores de Monterrey* graduating in December 1991. He continued in *I.T.E.S.M.-Mexico City Campus* where he earned a Bachelor's degree in Mechanical-Electrical Engineering in December 1996.

Before receiving his bachelor's degree, he decided to pursue graduate studies in the United States, and actively sought admission into Lehigh University, starting in January 1997. Taking a research assistantship at Lehigh University Energy Research Center permitted him to conduct studies in flow measurement accuracy in power plant stacks. He will receive the degree of Master of Science in Mechanical Engineering in January 1999. His future plans are to start a career in the Power Generation Industry and be involved in infrastructure projects around the globe.

END
OF
TITLE